Dissertation von Peter Fauland
Universität Bielefeld

"The COMPASS Experiment and the RICH-1 Detector"

Dissertation zur Erlangung
des Doktorgrades (Dr. rer. nat.)
Fakultät für Physik
Universität Bielefeld

vorgelegt von
Peter Fauland
aus Mannheim

März 2004

1.Gutachter : Prof. Dr. G. Baum
2.Gutachter : Prof. Dr. H. Steidl

Gedruckt auf alterungsbeständigem Papier °° ISO 9706

Contents

Abstract

The **Co**mmon **M**uon and **P**roton **A**pparatus for **S**tructure and **S**pectroscopy (COMPASS) is a new fixed target experiment at the CERN (Conseil Européen pour la Recherche Nucléaire) Super Proton Synchrotron (SPS) with the aim to study hadron structure with polarized muon beams and hadron spectroscopy with hadron beams.

The main physics objective of the muon beam physics program is the measurement of $\Delta G/G$, the gluon polarization in a longitudinally polarized nucleon. The hadronic program comprises a search for glue balls in the high mass region in exclusive diffractive pion proton scattering, a study of leptonic and semi leptonic decays of charmed hadrons with high statistics and precision and Primakoff scattering with various probes. A detailed investigation of charmed and doubly charmed baryons is performed in a second stage of the experiment.

The setup consists of two spectrometers, one for small angle and one for large angle particles, giving a wide angular acceptance for all measurements. Each spectrometer performs full particle identification using one Ring Imaging Cherenkov Counter (RICH), electromagnetic and hadronic calorimetry and muon detection. A high momentum resolution is obtained by using highly precise tracking with silicon detectors, gaseous strip detectors and drift tubes. The measurements are performed with high intensity beams allowing to collect the needed statistics.

The key-detector for particle identification is the RICH-1, which is a technological challenge in terms of photon detection and radiator gas supply. The COMPASS setup is presented with special focus on the radiator gas preparation and operational aspects of the gas system. Some first results on D^0 and D^* analysis are presented.

1 Introduction

The COMPASS experiment is a continuation of the European Muon Collaboration (EMC) [1], the New Muon Collaboration (NMC) [2], the and the Spin Muon Collaboration (SMC) [3] experiments at CERN. Semi-inclusive data by SMC resulted in a first measurement of $\Delta u_v, \Delta d_v$ and $\Delta\overline{u} + \Delta\overline{d}$ with similar measurements done by the HERMES (HERa MEasurement of Spin) experiment at DESY (Deutsches Elektronen Synchrotron). Beginning of 1995, two collaborations designed experiments, that seemed to be very similar in the foreseen setup. The *Hadron Muon Collaboration* (HMC) [4] proposed to investigate the spin structure of the nucleon by scattering of muons off a polarized target. The *Charm Experiment with Omni-Purpose Setup* (CHEOPS) [5] was interested in semi leptonic decays of charmed baryons. Looking at the COMPASS muon and hadron program the original formulation of physics questions of those programs are maintained.

Measurements of the deep inelastic scattering (DIS) of polarized muons or electrons from polarized nucleons by the EMC [1], SMC [6] and *Stanford Linear Accelerator Center* (SLAC) [7] collaborations have shown deviations between experimental data and the Ellis-Jaffe sum rule [8]. As a consequence, the spin of the nucleon cannot be described as the sum of the spin of quarks in the nucleon. This discovery led to what was called the *spin crisis* [9]. Possible explanations are thought to be due to the contributions to the nucleon spin from the polarization of the gluons, the spin of the sea quarks and orbital angular momentum of the quarks and gluons in the nucleon.

In the COMPASS muon program the measurement of the gluon polarization ΔG/G aims at investigating the gluon contribution to the spin. Comparison with lattice QCD calculations [10, 11] together with other model predictions will help to further improve our understanding of hadrons. Another feature of the experiment will be the detection of high statistics samples of events with charmed particles. Determining the cross-section asymmetry for open charm production in deep inelastic scattering will produce precise values of ΔG/G, the gluon polarization, to be compared with upcoming predictions from lattice QCD (quantum chromo dynamics) or other QCD-inspired models [12–14].

The use of hadron beams will allow detailed studies of semi-leptonic decays of charmed and doubly-charmed baryons to test Heavy Quark Effective Theory (HQET) [15] calculations. In addition the search for exotic states and the investigation of transverse spin distribution functions and structure functions will complete the total program.

A state-of-the-art spectrometer with particle identification and calorimetry, being capable of standing beam intensities up to $2{\cdot}10^8$ particles/spill, together with dedicated trigger setups for the different programs and fast read-out complement the performance of the system. After technical runs in 1999 and 2000, data taking started in 2001.

This thesis is organized in the following way: the subsequent chapters will describe the formation of the COMPASS experiment and will give a short overlook over competing experiments and the COMPASS experiment with its different physics programs. Special emphasis will be put on the RICH-1 detector. First results will be pointed out in chapter 10. Especially the preparation of the radiator gas, the quality control and the determination of the radiator gas transparency will be discussed in detail.

2 COMPASS - The historical consolidation of past experiments and projects

This chapter will give a brief overview of former experiments and projects whose physics goals are continued and consolidated by the COMPASS experiment. As direct predecessor the SMC experiment will be discussed in more in detail.

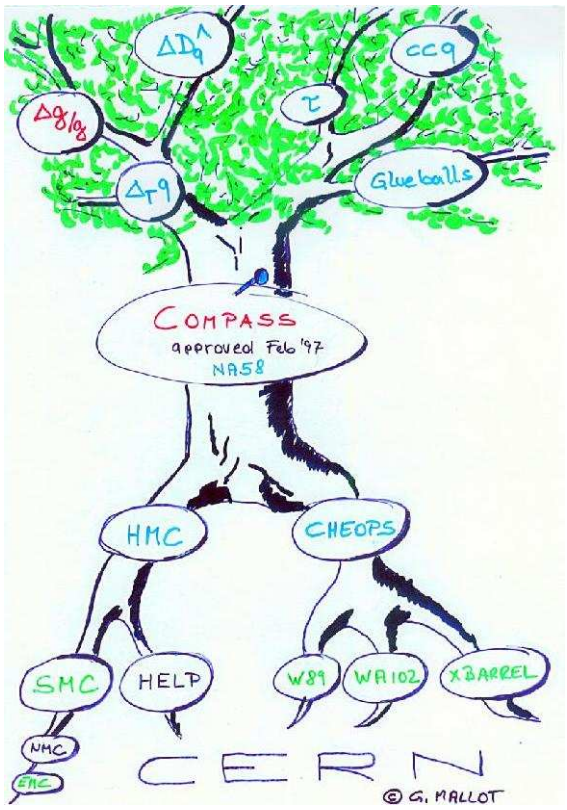

Figure 2.1: The roots of COMPASS.

2.1 The SMC Experiment

The aim of the Spin Muon Collaboration (SMC) was the measurement of cross section asymmetries of longitudinally polarized muons scattered off longitudinally polarized protons respectively deuterons. Many components were reused from the former EMC experiment and the production of the muon beam was similar to that at the Fermi National Laboratory (FNAL): the muons (190 GeV) originating from parity violating decays of $\pi-$ and K-mesons show a natural positive or negative longitudinal polarization P_m. With an angle of zero degree between muon and meson flight direction, the absolute value of polarization is expected to be 1. Besides Monte-Carlo simulation a direct measurement of this quantity based on parity violation of weak interaction is preferable. Taking the energy spectrum of positrons from muon decay, $\mu^+ \rightarrow e^+\nu_e\overline{\nu_\mu}$, the muon beam polarization can be given as a function of the variable y = E_e / E_μ - with E_e and E_μ as the positron- and muon energies. The published result is P_m = -0.8 $\pm$0.03 with an uncertainty for y below 1 % [16].

The polarization of the protons P_p is determined via nuclear magnetic resonance (NMR) using electromagnetic waves ($\sim$100 MHz). In case of exact match of the precession frequency of the spin and orientation of the magnetic field spin flip takes place in resonant absorption. A set of coils around the target (parallel to $[\vec{B}]$) are used to get an induced signal of the same frequency, where the area under the signal is proportional to the polarization. With an accuracy of 3% the value for P_p is about 90 %. With the cross section asymmetry for the deuteron and proton [17]

$$A = \frac{\sigma^{\uparrow\downarrow} - \sigma^{\uparrow\uparrow}}{\sigma^{\uparrow\downarrow} + \sigma^{\uparrow\uparrow}} \tag{2.1}$$

one can determine the spin dependent structure function $g_1^p(x)$. $\sigma^{\uparrow\downarrow}$ and $\sigma^{\uparrow\uparrow}$ are the cross sections for inclusive deep inelastic scattering of longitudinally polarized muons off longitudinally polarized deuterons, both for anti parallel and parallel orientation of beam and target polarizations. Taking the naive quark parton model, g_1 is related to the portion of the quarks with respect to the proton spin.

$$g_1 = \frac{1}{2}\sum_f \left(Q_f^2 \times \left[q_{f\uparrow} - q_{f\downarrow} + \overline{q}_{f\uparrow} - \overline{q}_{f\downarrow}\right]\right) \tag{2.2}$$

to be compared with the unpolarized structure function F_1 :

$$F_1 = \frac{1}{2}\sum_f \left(Q_f^2 \times \left[q_{f\uparrow} + q_{f\downarrow} + \overline{q}_{f\uparrow} + \overline{q}_{f\downarrow}\right]\right). \tag{2.3}$$

Using the integral over $g_1(x)$, one can deduce the total spin Σ, consisting of the

relative contributions of the three quark flavors u, d and s. The measured world average value [18] is

$$\Delta\Sigma = 0.23 \pm 0.07.$$

This is much smaller than the relativistic quark model prediction of 0.58 [8]. The basic picture of the nucleon spin as a sum of the three quark spins adding up to 1/2 was not in agreement with experimental data and the question "What carries the spin ?" evolved into the "spin crisis" [19] . In particular, the roles of angular momentum, the gluon spin and polarization of the sea quarks are not clear in this context.

2.2 The CHEOPS Project

End of 1995 a group of physicists [5] started to investigate the possibilities to continue the study of light and charmed hadrons at CERN after the end of the Omega experiment: a new fixed target experiment at the SPS named CHEOPS was proposed. The foreseen physical program contained the study of charmed hadrons, the exploration of glue balls in central production with the help of exclusive pp-interactions, the search for hybrid systems, a more detailed analysis of Primakoff scattering in order to be able to measure the polarizability of different hadrons and to pursue the questions about color transparency and color fluctuation. Selected topics in charm physics were determination of lifetimes, form factors and decay constants of charmed and doubly charmed hadrons. The study of semi leptonic decays is very important, since it provides an easy access to the corresponding form factors where precise predictions come from (HQET) [15] . For spectroscopy purposes this field is also of special interest as many baryon states have not experimentally been detected till this day. For theoretical aspects the production of charmed baryons is as well of great interest. Doubly charmed baryons represent an optimal basis for investigation of these production mechanisms. The ground state can be treated as a heavy meson or hydrogen-like system with two heavy c-quarks forming a color anti-triplet which is surrounded by a light quark. Another main research is charmed exotics - quark configurations that can not be interpreted as the usual $q\overline{q}$- or qqq-states such as a pentaquark, which is a qqq-c$\overline{s}$-state. CP-violation in charm systems should be accessible via D-meson decay. Those purposes lead to the following requirements concerning the detector:

- the study of charmed events needs a large spectrometer acceptance, implying a two stage spectrometer
- extremely short lifetimes (femtoseconds) require excellent vertex-reconstruction
- the proof of semi leptonic decays demands a muon-detector with large acceptance
- good particle identification for clean charm production channels.

The planned detector layout comprised two spectrometer stations each equipped with tracking, particle identification, electromagnetic calorimetry and muon filter. Figure 2.2 provides a schematic view.

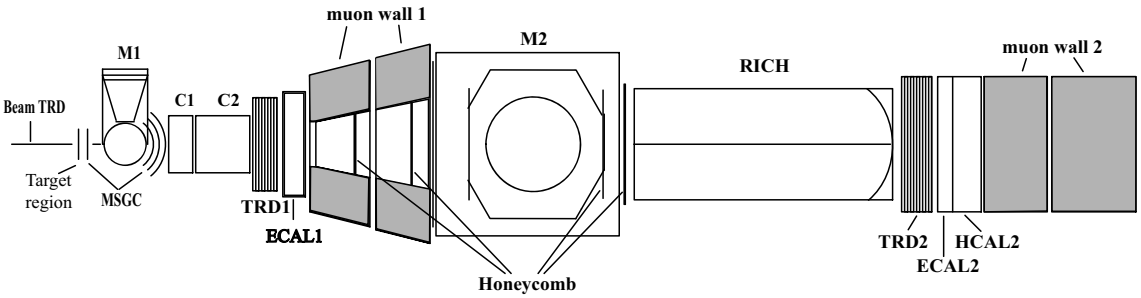

Figure 2.2: Schematic view of the CHEOPS-Experiment.

At that time, the planned location for the experiment was the CERN muon hall, which was occupied by SMC. Therefore, it was considered to consolidate both experiments.

2.3 The HMC Project

The physics goals of the HMC collaboration [4] were the study of hadrons from deep inelastic scattering of polarized muons with longitudinally polarized solid state targets to determine the gluon polarization $\Delta G/G$ by measuring the asymmetries in open charm production. The measurement of the longitudinal polarization of $\Lambda-$ and $\overline{\Lambda}$-hyperons both in target as well as in current fragmentation should be used to verify models explaining the spin contents of the nucleon and for the first time allow direct measurements of the spin transfer in fragmentation. Further verifications by experiments at CERN and SLAC had confirmed the original EMC results, stating that the spin content of the nucleon cannot be traced back to the spins of the quarks alone. The gluon interpretation [20, 21] holds the polarized

glue ΔG responsible for the reduced contribution of the quarks to the nucleon spin, while other models [22] claim negatively charged strange quarks. The experimental approach comprises of proton-proton-collisions and semi-inclusive lepton scattering. The collaboration proposed photon-gluon fusion, leading to open charm production, to measure ΔG. A different approach is the determination of asymmetries in single or correlated production mechanisms using deep inelastic scattering with the observation of high p_t-particles[1]. This method was successfully used by the SMC collaboration obtaining the first data concerning Δu_v, Δd_v and $\Delta\overline{u} + \Delta\overline{d}$. Measuring the polarization of Λ out of target fragmentation can answer this question. Assuming those spin dependent fragmentation functions are known, also for transverse spin positions, they can be used in deep inelastic scattering processes with transverse polarized targets to calculate the probability to find a specific quark with parallel or anti parallel spin with respect to a polarized nucleon. In this case a different approach to attack the h_1 structure function was presented by J. Collins [23]. He suggested measuring (transverse) spin dependent azimuthal asymmetries of several hadrons in the direction of the virtual photon. The planned experimental setup is outlined in Figure 2.3.

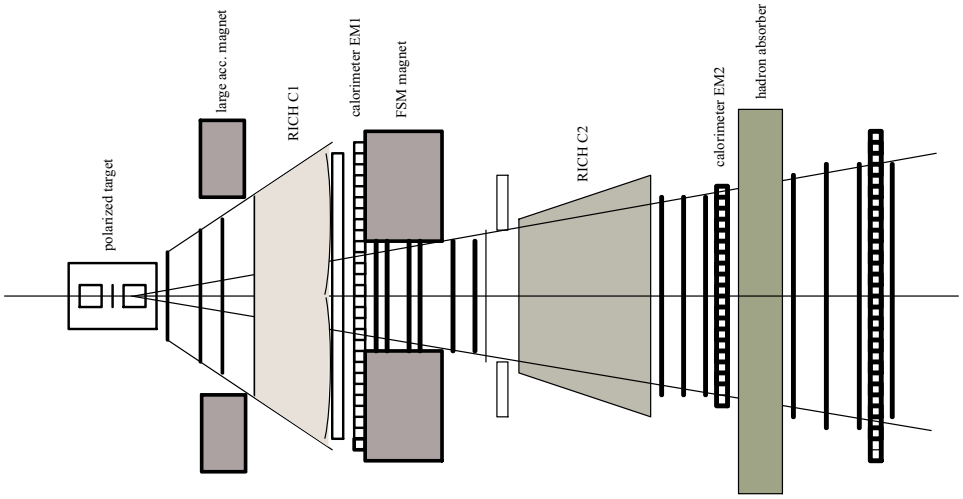

Figure 2.3: Schematic view of the HMC-Experiment.

[1]particles with a high transverse momentum p_t

3 Competing Experiments

HERMES

Besides COMPASS, which is data taking since 2000, HERMES [24] is another polarized deep inelastic scattering experiment for lepton-nucleon scattering. In addition to earlier HERMES studies, measuring inclusive events, the experiment has also been used to measure *semi-inclusive* cross section asymmetries where outgoing hadrons are identified along with the scattered lepton. Beginning in 1998, a number of upgrades have been installed which significantly expanded the capabilities of the original HERMES spectrometer [25]. These modifications are known as the 'charm upgrade' and aimed at improving the ability to perform a flavor decomposition of the spin contributions to the nucleon and to permit measurement of $\Delta G/G$ with reasonable precision. The replacement of the threshold Cherenkov Detector with a dual-radiator RICH was the most important for the program to study the polarization of the strange sea quarks. The HERMES instrument uses two radiators, C4F10, a heavy fluorocarbon gas, and a wall of silica aerogel tiles. In this way the refractive index can be tuned in an optimum way. Since commissioning in 1999, the RICH has performed well and the first physics analysis using its particle identification capabilities have been carried out ([26] and references therein). This detector is also essential in order to study the gluon polarization through charmed meson production, where Kπ decays of D mesons must be cleanly identified. Spin asymmetries from inelastic J/ψ production are also useful to determine the gluon polarization. An iron wall instrumented with scintillation hodoscopes behind was installed at the rear of the spectrometer in 1998. The iron acts as a muon filer thereby allowing identification of muon pairs from J/ψ decays. In 1999 additional scintillation counters were installed on the faces of the spectrometer magnet to act as a muon filter and permit crude momentum analysis of those detected muons. The third component of the charm upgrade is the installation of tracking chambers in the pole gaps of the first two HERA quadrupoles downstream of the spectrometer. A fraction of the low energy electrons scattered in the target are momentum-analyzed by these instrumented quadrupoles. The information is used to determine the kinematics of the virtual photon J/Ψ production as well as other reactions in which the scattered lepton is emitted at forward angles.

Another major upgrade to the spectrometer underway since 2000 is the installation of two wheel-shaped planes of silicon micro-strip detectors with a diameter of about 50 cm (called the 'Lambda Wheels') inside the vacuum chamber, immediately downstream of the internal target. These form a critical part of the extended acceptance of the muon tracking system. Their primary purpose is to increase the acceptance for Λ^0 hyperon detection. This detector enhancement is useful in the forward current fragmentation region where Λ^0 typically contains an up quark which is expected to yield new information about helicity of strange quarks in the nucleon. Finally a prototype of a silicon recoil detector, which was designed to detect very low momentum particles outside the present HERMES acceptance below the target cell was already successfully tested during the 1998 running year. Combining open and hidden charm channels with the presently accumulated luminosity on the polarized hydrogen and deuterium targets results in a measurement of ΔG(x)/G(x) = 0.41 $\pm$0.18 (stat) $\pm$0.03 (syst) for $< x_G >$=0.17 with $< \overline{p}_T^2 > = 2.1$ (GeV/c)^2 [27]. These are difficult measurements at HERMES due to the low cross sections involved.

In summary, the new instrumentation at HERMES allows the detection of D mesons, and enhances the acceptance for J/ψ mesons. It will be possible to measure values of ΔG(x) using polarization asymmetries for three independent channels - production of hadron pairs, D^0 and J/ψ. The statistics in each channel will be limited, but backgrounds and theoretical uncertainties enter differently in each of the measurements. An important point is that the range of x_G covered by charm production at HERMES ($< x_G = 0.30 >$) is higher than in any other experiment, while that for hadron pair production is $< x_G = 0.17 >$. Hence measurements of the gluon polarization at HERMES are complementary to those at other laboratories and are useful for the determination of the complete integral of ΔG(x).

RHIC:

The Spin Collaboration [28] at Brookhaven's new Relativistic Heavy Ion Collider (RHIC) will probe the proton spin structure in polarized proton-proton-collisions at center-of-mass energies from 50 to 500 GeV. RHIC is primary a collider for heavy ion physics. The RHIC spin program is complementary to the heavy-ion collision experiments. Both aim at studying the appropriate degrees of freedom for the description of hadronic systems, and especially the relationship of confined constituent quarks to the current quarks and gluons. The spin physics program involves the acceleration and storage of polarized proton beams and allows experiments with the two major detectors, STAR and PHENIX. This program will run during the

calibration proton runs for the heavy ion program (roughly 20% of the running time per year). In contrast to lepton deep inelastic scattering experiments, at RHIC the nucleons are effectively bombarded by quark and gluon probes. Scattering results are directly sensitive to gluon polarization through direct photon, jet, and heavy flavor production. Parity violating $W^{\pm}$ production will give the possibility to decompose the u-, d-quark and sea quark flavor contributions to the proton spin. Finally, measurements of single and double spin asymmetries with transversely polarized protons at RHIC will provide access to the transversity structure function $h_1(x)$. In the year 2001 the upgrades in STAR and PHENIX for spin physics were completed and first physics runs with polarized proton beams (with aimed longitudinal polarization of up to 70 % at collision point) at $\sqrt{s} = 200$ GeV took place. Several measurements to access the polarized gluon and sea quark distributions are proposed. The measured asymmetries (e.g. the double longitudinal spin asymmetry $A_{LL} = \frac{\Delta G}{G} \times A_1^P \times \overline{a}_{LL}$ and the single asymmetry A_N^{PP}) are a convolution of the polarized parton distribution functions from both colliding protons and the elementary scattering asymmetry summed over the different sub processes that contribute to the observed events.

E161, SLAC:

The E161 collaboration [29] proposed to measure the gluon spin distribution using polarized open charm photo production by tagging decays of D mesons into high transverse momentum muons. The muon momentum is measured via fine grain hodoscopes, the kaon and pion is absorbed before the decay. Table 3.1 shows the fraction of μ^+ and μ^- used for charm tagging.

	D^+	D^0	D_S^+	Λ_c^+
produced (%)	19	63	8	8
branching ration (%)	17	7	8	4
fraction of μ^+ (%)	37	47	8	4
	D^-	D^0	D_S^-	Λ_c^-
produced (%)	21	71	6	2
fraction of μ^- (%)	40	53	5	1

Table 3.1: Charm tagging via single decay muons in the E161 experiment at SLAC.

The asymmetry for single muons is measured in the range $0.1 < x < 0.5$. The quasi monochromatic and circularly polarized photon beam used will be produced by polarized electrons hitting an diamond crystal. Coherent bremsstrahlung is used to generate the beam. By rotating the crystal axis, three energies between 45 and 51

GeV at a current of 2 $\times 10^{10}$ electrons per 500 ns long beam pulse will be available. The target is longitudinally polarized LiD at a temperature of 300 mK, centered in a 6.5 T magnetic field to obtain a polarization higher than 60%. Dynamic Nuclear Polarization (DNP) is used to polarize the material in the 3 cm long and 1 cm diameter cylinder. The setup is similar to that used in SLAC experiments E143 and E155. The spectrometer consists of a 3 m aluminum absorber surrounded by a dipole magnet and three planes of scintillator hodoscopes. The experiment is approved but will have to wait for allocated beam time for five years.

4 The Muon Program

After confirmation of the original EMC results by recent experiments at CERN and SLAC (Stanford Linear Accelerator Center) it has now been established that the spin content of the nucleon is not entirely carried by its quarks. There are different interpretations for this result. The gluon interpretation holds the polarized glue ΔG responsible to lower the quark's contribution to the nucleon spin, whereas alternative theories make negatively polarized strange quarks responsible. There are several approaches to resolve these ambiguities in the interpretation. As inclusive measurements of the gluon polarization do not allow to distinguish the role of each individual parton distribution function, it is needed to either study polarized proton proton collisions or to perform polarized semi-inclusive lepton scattering. The gluon polarization $\Delta G/G$ is measured using photon-gluon fusion processes leading to open charm production as a clean channel to access ΔG among other possibilities (see Figure 4.1).

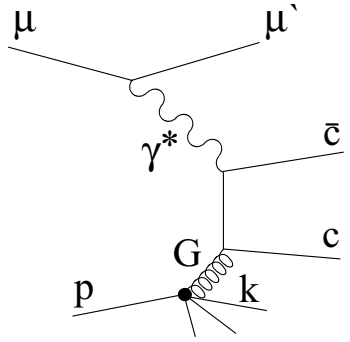

Figure 4.1: Feynman diagram showing charm prod. via photon-gluon fusion.

Another approach is the determination of asymmetries in single or correlated high p_T particle production in deep-inelastic scattering. The following sections 4.1 to 4.3 explain the main physics objectives of the COMPASS muon program in more detail.

4.1 Charm Production via Photon-Gluon Fusion

The study of the longitudinal spin asymmetry of open charm lepto production in muon proton collisions is favorable to measure $\Delta G/G$. The proposed measurements are based on the reconstruction of D^0 mesons from their hadronic decay products. Special attention is paid to the determination of the combinatorial background from other inelastic interactions of quasi-real photons, where tagging of D^{*+} decays is an efficient way of background suppression (see chapter 10.4). The measured quantity is the number of events $N_{c\bar{c}}$, where charm quarks are produced. Taking the ratio of the difference of the number of events with parallel and anti parallel beam and target polarization and the sum of these quantities one gets the spin dependent asymmetry A_{exp}:

$$\begin{aligned} A_{exp} &= \frac{\left(N_{c\bar{c}}^{\uparrow\downarrow} - N_{c\bar{c}}^{\uparrow\uparrow}\right)}{\left(N_{c\bar{c}}^{\uparrow\downarrow} + N_{c\bar{c}}^{\uparrow\uparrow}\right)} \\ &= P_B \times P_T \times f \times A_{\mu N}^{c\bar{c}}, \end{aligned} \tag{4.1}$$

with P_B and P_T being beam and target polarization, respectively and f the dilution factor of the target, giving the fraction of nucleons in the target material that can be polarized. The correlation between asymmetry $A_{\mu N}^{c\bar{c}}$ and virtual photon asymmetry $A_{\gamma N}^{c\bar{c}}$ is

$$A_{\mu N}^{c\bar{c}}(y) = D(y)\, A_{\gamma N}^{c\bar{c}}, \tag{4.2}$$

with the depolarization factor D of the virtual photon with respect to the incident polarized muon (neglecting the muon mass). The depolarization factor represents the transfer polarization from the incoming muon to the virtual photon :

$$D(y) = \frac{\left[1 - \left(1-y\right)^2\right]}{\left[1 + \left(1-y\right)^2(1+R)\right]}, \tag{4.3}$$

with y = (E - E') / E representing the relative energy transfer from the muon to the virtual photon. The energy of the virtual photon is ν with ν = E - E'. R is the ratio of the longitudinal to the transverse photo-absorption cross section. The asymmetry $A_{\gamma N}^{c\bar{c}}$ is given by the ratio of the helicity dependent and helicity averaged cross sections for charm production $\Delta\sigma^{\gamma N \to c\bar{c}X}$ and $\sigma^{\gamma N \to c\bar{c}X}$ [30–32]. They can be described using the elementary photon-gluon cross sections (polarized and unpolarized):

$$\Delta\sigma(s) = \frac{4}{9}\,\frac{2\pi\alpha_e\alpha_s(\widehat{s})}{\widehat{s}}\left[3\beta - ln\frac{1+\beta}{1-\beta}\right], \tag{4.4}$$

and

$$\sigma(s) = \frac{4}{9}\,\frac{2\pi\alpha_e\alpha_s(\widehat{s})}{\widehat{s}}\left[-\beta(2-\beta^2)+\frac{1}{2}(3-\beta^4)ln\frac{1+\beta}{1-\beta}\right], \tag{4.5}$$

with α_e as electromagnetic coupling constant and α_s as strong interaction coupling constant. Finally, using the gluon distributions ΔG and G, $A_{\gamma N}^{c\bar{c}}$ can be written as:

$$A_{\gamma N}^{c\bar{c}} = \frac{\int_{4m_c^2}^{2M_N E_y} d\widehat{s}\Delta\sigma(\widehat{s})\Delta G(\eta,\widehat{s}))}{\int_{4m_c^2}^{2M_N E_y} d\widehat{s}\sigma(\widehat{s})G(\eta,\widehat{s})}, \tag{4.6}$$

where $\beta = \sqrt{1-4m_c^2/\widehat{s}}$ is the center of mass velocity of the charm quark, $\widehat{s} = (q+k)^2$ is the invariant mass of the photon-gluon system, q and k are the photon and gluon 4-momenta, and $\eta = \widehat{s}/2M_N E_y$ is the gluon momentum fraction. This asymmetry is assumed to be independent of Q^2. With an incident muon energy of 100 GeV the depolarization factor D is large in the range of $0.08 < \nu < 0.35$, exactly the region where a maximum of ΔG(η) is expected. With this muon energy, the photon energy is between 35 GeV and 85 GeV with an integrated cross section of 1.9 nbarn. The averaged depolarization factor in this energy regime is D = 0.66.

About 60% of charm quarks fragment into a D^0 and 20% to a D^{*+} resulting in $N^{D^0}/N^{c\bar{c}} = 1.23$ D^0 mesons per charm event. The detection strategy is based on the combinatorial search for the hadronic decay products. The simplest decay of the D^0 meson is the two-body decay $D^0 \rightarrow K^- + \pi^+$ with a branching ratio of $(3.80 \pm 0.09$ %) [33], where the number of accidental combinations is lower than in three or four-body decays. The momentum of the outgoing particles in the center of mass frame is large with p*=861 MeV. The background in this analysis can be significantly reduced by tagging D^{*+} decays. The decay chain is

$$D^{*+} \rightarrow D^0\pi_S^+ \rightarrow (K^-\pi^+)\pi_S^+, \tag{4.7}$$

where an *additional* soft pion π_S^+ is required. The mass difference Δ M = m($K^-\pi^+\pi_S^+$) - m($K^-\pi^+$) = 145 MeV can be measured much more precisely than the D^{*+} mass itself. The D^{*+} tagging method is also studied for the more complex three and four-body decays [34]:

$$\begin{aligned} D^0 &\rightarrow K^-\pi^+\pi^0 && (13.1 \pm 0.9)\ \%, \\ D^0 &\rightarrow K^-\pi^+\pi^+\pi^- && (\ 7.5 \pm 0.3)\ \%, \\ D^+ &\rightarrow K^-\pi^+\pi^+ && (\ 9.1 \pm 0.6)\ \%. \end{aligned}$$

Figure 4.2 explains the tagging mechanism with a D^0-meson as an example.

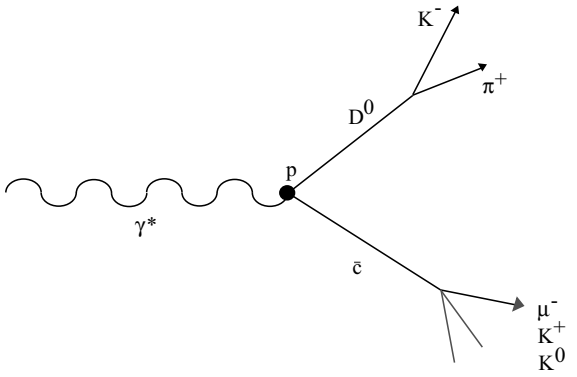

Figure 4.2: Tagging on the antiparticle. Looking for K π combinations from D^0 decays and the corresponding particles coming from the opposite charm decay one can use μ^-, $K^\pm$ or K^0 for tagging.

An additional approach is the measurement of Λ- and $\overline{\Lambda}$-polarization: this method allows one to get more information about strange quark and anti strange quark polarization in addition to the information coming from photon-gluon fusion. These measurements represent a possibility to explain why the spin content of the protons is rather low. On one side the reason could be found in polarized gluons, on the other side negatively polarized strange quarks could be responsible. The low polarization of the strange quark makes this rather unlikely. In addition, the spin transfer function from the hit quark to a Λ-hyperon can be determined by measuring $\Lambda/\overline{\Lambda}$-polarization.

4.2 Semi-Inclusive Deep Inelastic Scattering

The spin of the nucleon can be decomposed into contributions from the individual quarks and anti quarks, gluons and the orbital angular momenta of the quarks and gluons:

$$s = \frac{1}{2} = \frac{1}{2}\Delta\Sigma + \Delta g + L_q + L_g, \tag{4.8}$$

with Δg representing the gluon contribution, L_q and L_g the quark and gluon orbital angular momentum contributions. Neglecting heavy quark flavors the constituent quark/anti quark contributions are described as

$$\Sigma = \Delta u + \Delta\overline{u} + \Delta d + \Delta\overline{d} + \Delta s + \Delta\overline{s}. \tag{4.9}$$

Accurate data on the spin structure functions $g_1(x,Q^2)$ for both proton and neutron have been provided by polarized deep inelastic lepton-nucleon scattering

experiments. Information from inclusive scattering is limited by the domination of scattering from up quarks, since the cross section scales with the square of the electric charge. Quarks and anti quarks of the same flavor enter in a similar way. To distinguish between the contributions from the quark flavors and to separate the sea and valance quark components it is necessary to use additional types of experimental information. Semi-inclusive scattering refers to measurements where one or more hadrons are detected in the final state. In most cases the scattered lepton is also detected since it defines the Bjorken variables in the scattering. The essential principle behind the use of semi-inclusive scattering is the high likelihood that the leading hadron 'contains' the quark originally struck by the virtual photon. Scattering asymmetries with various leading hadrons in the final state can be analyzed to measure the fractional contributions of the various quark flavors to the nucleon spin.

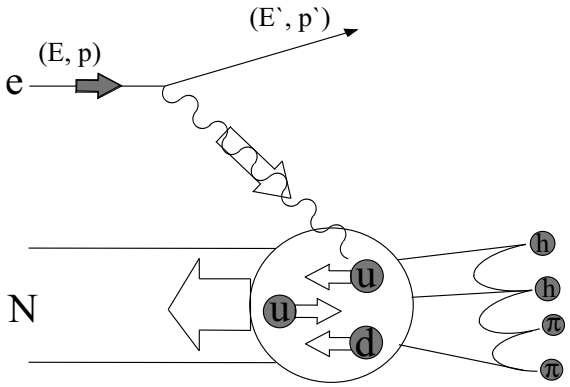

Figure 4.3: In semi-occlusive deep inelastic scattering, a hadron h is also detected.

The nucleon breaks up into fragments escaping parallel to its initial momentum (target region) and other hadrons more collinear with the direction of the photon (current region). Semi-inclusive measurements provide the possibility of identifying the flavor of the struck quark thereby allowing extraction of the polarized quark distributions for each quark and anti quark flavor (see Figure 4.3 and 4.4). For example, a high momentum π^+ observed in the final state is a strong indication that a u quark was struck in the collision, whereas a high momentum π^- indicates that a d quark was struck by the parton. Observed K-mesons arise from interactions with strange quarks and anti quarks in the sea. The contributions of each quark flavor $\Delta q_f(x,Q^2)$ can be investigated as a function of the kinematic parameters x and Q^2. Furthermore, the flavor-tagging method does not rely on the assumption of flavor symmetry to extract the polarized quark distributions. The importance of the semi-inclusive reactions is attributed to the fact that they allow isolation of the valence and sea quark contributions to the nucleon spin.

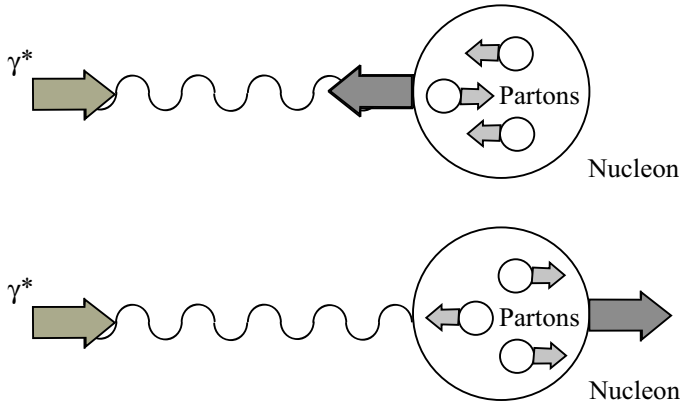

Figure 4.4: In deep inelastic scattering with polarized lepton beams and polarized nucleon targets, one probes the polarization of the quarks in the nucleon (seen in the lab frame).

$$\sigma_{1/2} \sim q^+(x) \quad F_1 = \frac{1}{2}\sum_i e_i^2 q_i$$
$$g_1 = \frac{1}{2}\sum_i e_i^2 \Delta q_i$$
$$\sigma_{3/2} \sim q^-(x) \quad \Delta q_i = q_i^+ - q_i^-$$

4.3 Transverse Spin Distribution Functions

As shown by Jaffe and Ji [35, 36], the quark state inside the nucleon is entirely specified by the momentum distribution q(x), the helicity distribution Δ q(x) and the transverse spin distribution $\Delta_T\ q(x)$. The functions $\Delta_T\ q(x)$ have never been measured before. However, in all existing estimates this quantity is nonzero at least for u quarks and is different from its longitudinal analogy Δ q(x). In analogy to g_1(x), one can construct a new structure function $h_1(x)$ from $\Delta_T\ q(x)$

$$h_1(x) = \frac{1}{2}\sum_q e_q^2[\Delta_T q(x) + \Delta_T \overline{q}(x)]. \tag{4.10}$$

Other than g_1(x) which can be obtained directly from the lepton-nucleon cross-section asymmetry, h_1(x) cannot be measured in a single inclusive process, due to its odd chirality nature. But the transverse spin distribution functions can be measured via semi-inclusive deep inelastic scattering using transverse polarized proton- and deuteron targets. By measuring the hadrons involved, the struck quark flavor can be identified. The spin distribution function can be specified for each quark flavor:

$$\Delta_T\ q(x) = q\uparrow(x) - q\downarrow(x). \tag{4.11}$$

Arrows indicate parallel or anti-parallel quark spin orientation with respect to the transverse orientation of the nucleon spin. One method to measure the quark transverse polarization relies on the measurement of the transverse polarization of Λ hyperons.

5 The Hadron Program

Three main topics will be investigated using hadron beams: study of charmed hadrons, spectroscopic analysis of light quark and glue ball systems and investigations in the field of hadronic structures via Primakoff reactions.

For this program several detector-systems upstream of SM1 have to be changed. The first spectrometer e.g. will be made out of several tracking chambers. To be able to stand high particle fluxes and offer the spatial resolution needed, micro strip gas chambers are foreseen. For the detection of charmed hadrons a special target-detector will be installed to allow exact track reconstruction of charmed hadrons. This setup will consist of a dense arrangement of target material, trigger counters and 10μm pitch silicon detectors, installed with a distance of only 1 mm, followed by additional double-sided large area silicon detector hodoscopes. These silicon detectors will be also used upstream the target for beam-definition purposes. For the light-quark spectroscopy this detector-system will be replaced by a 40 cm liquid hydrogen target, together with a silicon detector. A time-of-flight detector will be arranged around the target cell, to detect recoil-protons. This system will consist of many scintillation-counters, mounted in a cylindrical shape with 40 cm diameter. In case of Primakoff measurements and diffractive meson-production merely a heavy target, followed by silicon-detectors will be used. The COMPASS hadron program is foreseen to start after the SPS-shutdown in 2005.

5.1 Hadrons with Charm

The knowledge of semi leptonic decay widths is one of the most important issues in charm physics as they provide the best test for our understanding of charmed baryons. Since precise theoretical predictions exist about rates and form factors, special effort was put in the q^2 -dependence of form factors in the framework of HQET calculations [15]. Up to the present day all $1/2^+$ states of charmed baryons were observed, but only very little is known about doubly-charmed baryons. Presumably they consist of a heavy cc-diquark surrounded by a light quark. Such states are expected in the mass region of 3.6 GeV (ccu, ccd) to 3.8 GeV (ccs). Unfortunately the study of ccq-baryons is complicated by the fact that production cross sections are very low which makes high rate experiments necessary to collect the needed amount of statistics.

5.2 Light Quark Systems

One fundamental statement of quantum chromo dynamics (QCD) is the existence of states consisting of valence gluons: Glue balls and Hybrids. As QCD can not give any predictions about non- $q\overline{q}$ state spectra, there is the need to fall back on different models, predicting a huge variety of those states. According to lattice QCD calculations masses for the lightest glue balls should be in the mass region of 1500 MeV to 1800 MeV for the 0^{++}-state. Since many years there has been an attempt to establish the existence of glue balls and hybrids, with the best candidate coming from LEAR (Low Energy Storage Ring, CERN): a Scalar glue ball $f_0(1500)$. To obtain a data sample enriched with $q\overline{q}$-states COMPASS will go for two production mechanisms: central production and diffractive scattering of mesons by nuclei. One can observe many decay modes including photons as well as neutral and charged pions and kaons, with special emphasis on the glue ball preferred final states containing $\eta\eta$ and $\eta\eta'$-mesons.

5.3 Primakoff Reactions

The study of the nucleon structure gained general interest since non-perturbative QCD descriptions are available. In particular, chiral perturbation theory allows making precise predictions for a number of quantities such as polarizabilities and cross sections in $\pi - \gamma$-reactions [37]. At this time such studies are performed at low energy electron accelerators. High energy pion, kaon, and hyperon beams allow complementary measurements using Primakoff reactions , which is Compton scattering with virtual photons in inverse kinematics (see Figure 5.1). Under certain kinematical conditions photo-production of neutral mesons and their decay into two photons can be described using the same interaction. Taking this into account lifetimes of mesons are more easily determined, namely via photo-production instead of via decay modes.

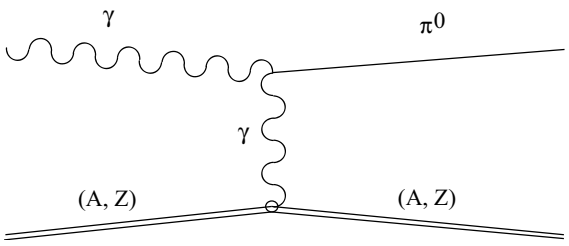

Figure 5.1: Schematic representation of the Coulomb photo production of neutral pions (Primakoff effect).

6 The COMPASS Muon Beam

The beam for the muon program is the polarized muon beam M2 of CERN-SPS, that is modified to satisfy COMPASS specifications. To reach the design beam intensity of $2 \cdot 10^8$ muons per spill with an energy of up to 190 GeV, a proton intensity of 10^{13} protons per spill (5.1 s with a total cycle time of 16.8 s) with energies up to 450 GeV is needed. The acceleration cycle of the SPS is 16.8 seconds since the year 2000. In order to produce the muon beam, the proton beam is focused on a beryllium target of 0.5 m length, whereas the accelerating structures are switched off just before the extraction. The existing bunches during acceleration are distributed equally around the ring, to be directed toward the primary beryllium target during a specified period of time. Pions being created here, are momentum selected and continue their travel through a 600 m decay path. Roughly 10% of the pions decay into muons. Using a beryllium absorber they are separated from the remaining hadrons and momentum selected. The muon beam is directed toward the experimental area. Assuming suitable kinematics, the muon beam is naturally polarized because of the weak decay of pions, pseudo scalar mesons, which have a total angular momentum equal zero. Looking closer at the process $\pi^+ \rightarrow \mu^+ \nu_\mu$ both outgoing fermions must have opposite spin, due to the conservation of angular momentum. Massless neutrions are left handed with negative helicity, where spin and momentum are anti parallel aligned. This results in a defined spin orientation of the muon. The distribution of the muon in the rest system of the pion is isotropic. Using the relation $\gamma \sim p_\pi / m_\pi$ one gets for the longitudinal momentum of the muon in the lab system:

$$p_{\mu_\parallel} = \frac{p_\pi}{2}\Big[(1-b)cos\theta + (1+b)\Big], \tag{6.1}$$

with b = $(\frac{m_\mu}{m_\pi})^2 \sim 0.573$. Thus, the momentum of the muon in the lab system is explicitly defined by the angle θ defining the emitted angle. The beam polarization is likewise associated with that angle, implicating that with a corresponding choice of pion and muon energy the polarization is fixed. With p_π = 177 GeV and p_μ = 160 GeV one expects a polarization of

$$P_\mu^+ = -0.75 \pm 0.04. \tag{6.2}$$

The experience of the SMC collaboration showed good agreement between measured polarization and Monte-Carlo-simulations, resulting in the abandonment of a direct

measurement at COMPASS. Phase space properties of the beam play an important role for the design of the spectrometer, since the phase space volume of the muon beam is large with respect to the primary particle beam. The reasons for that are the production mechanism on the one hand and the large diffusion power of the muons, enforcing the effect of beam focusing, on the other hand. As a direct consequence one has to cope with a strong beam halo, consisting of particles which are crossing beam focusing elements. The 1σ - width of the muon beam is vertically 7.6 mm, horizontally 8.9 mm, with a corresponding beam divergence of 0.9 mrad and 0.7 mrad, respectively. The measurement of the beam momentum is done by the Beam Momentum Station (BMS, Table 6.1) along the beam line M2. Each station consists of two planes of segmented scintillator hodoscopes placed up- and downstream of the bending magnet B6. Figure 6.1 schematically illustrates the setup.

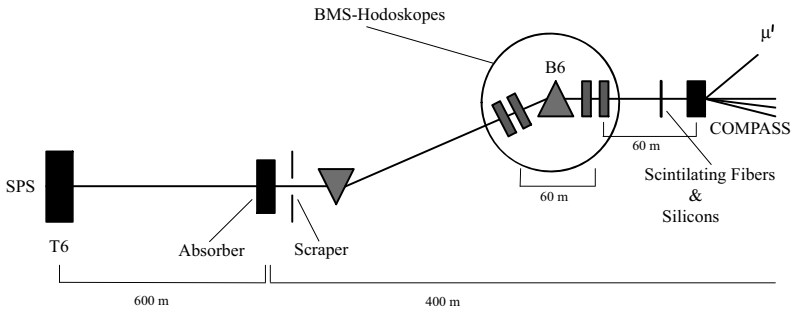

Figure 6.1: BMS setup along the M2 muon beam line.

BMS	
Single Plane Time Resolution	262 ± 10 ps
Multiplicity, hits per plane per event	5
Efficiency	$82 \ldots 93$ %
Scintillator element dimensions	5×20 mm
Stations , outer dimensions	180×60 mm
	90×120 mm
	100×120 mm
	230×60 mm

Table 6.1: Properties of the BMS.

7 The COMPASS Spectrometer

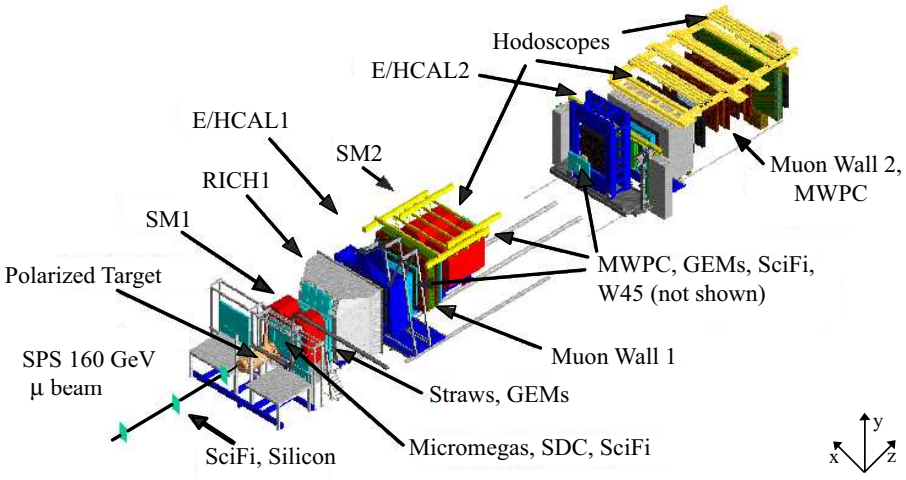

Figure 7.1: Design of the COMPASS experimental setup.

As described in the two previous chapters the experiment includes measurements of different nature, making it necessary to have optimized setups. Still the general layout in Figure 7.1 shows many similarities, namely a modern forward-spectrometer capable of high rates consisting of two independent parts equipped with tracking, particle identification, calorimetry and muon walls. A large part of the setup will be used for both physics programs, which is particularly true for the region downstream of the first spectrometer magnet SM1. As the target setups are completely different the region upstream of RICH-1 has to be individually designed, including different large angle spectrometers. The requirements for different detectors are defined by the different measurements with the most strict ones being based on the high intensity of the muon beam leading to detector rates of 100 MHz and the enormous interaction rate in the hadron beam (1 MHz). These high rates demand special choices of detector materials to avoid radiation damages. The need for fast and efficient triggering for charmed events implies also high demands in terms of speed of the detector readout making special front-end electronics, multi-buffering and fast mass storage systems necessary. The following sections describe the particular components of the large- and small angle spectrometer. The design of the two parts is similar and consists of a bending-magnet

SM1/2, Ring Imaging Cherenkov Counters RICH 1/2, electromagnetic calorimetry ECAL 1/2, hadron calorimetry HCAL 1/2 and muon filters 1/2.

7.1 The COMPASS Target

Technical problems prevented the completion of the COMPASS target solenoid in time, which made it necessary to reactivate the SMC target magnet [38] . Figure 7.2 illustrates the difference of the two spectrometer setups: being forced to operate with a smaller acceptance angle (± 70 mrad instead of ± 160 mrad) the positioning of all the detectors downstream the target had to be adjusted and optimized. The basic features of the SMC target system [39] remain unchanged: polarizing the nucleons via dynamic nuclear polarization (DNP), that is described in more detail later, in an homogeneous magnetic field of 2.5 T at temperatures below 0.5 K.

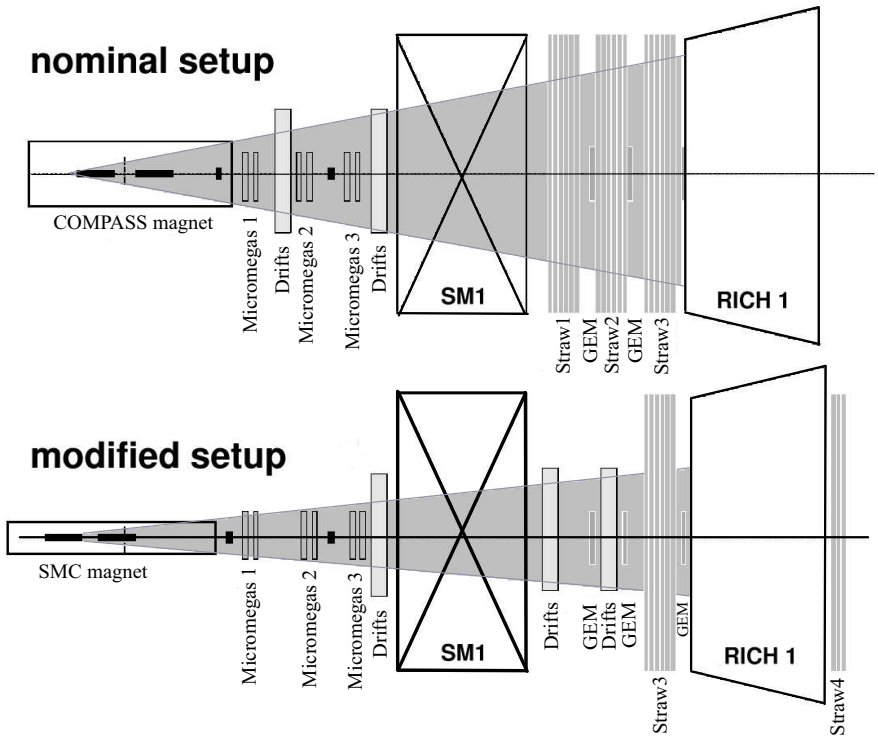

Figure 7.2: Comparison of the original and the modified COMPASS muon setup.

The target itself consists of two cylindrical oppositely polarized target cells (see Table 7.1). This is essential to minimize systematic errors as it is not possible to quickly reverse the polarization of a target cell and to measure under exactly equivalent experimental conditions. With the two target cells, equivalent to infinitely fast field reversals, instrumental asymmetries can be minimized or even totally eliminated.

Material	NH_3	^6LiD
Length of cell [cm]	60	60
Distance between cells [cm]	10	10
Diameter of cell [cm]	3	3
Areal density [g/cm]	61	59
Dilution factor	0.176	0.5
Polarization	0.85	0.5

Table 7.1: Properties of the target setups.

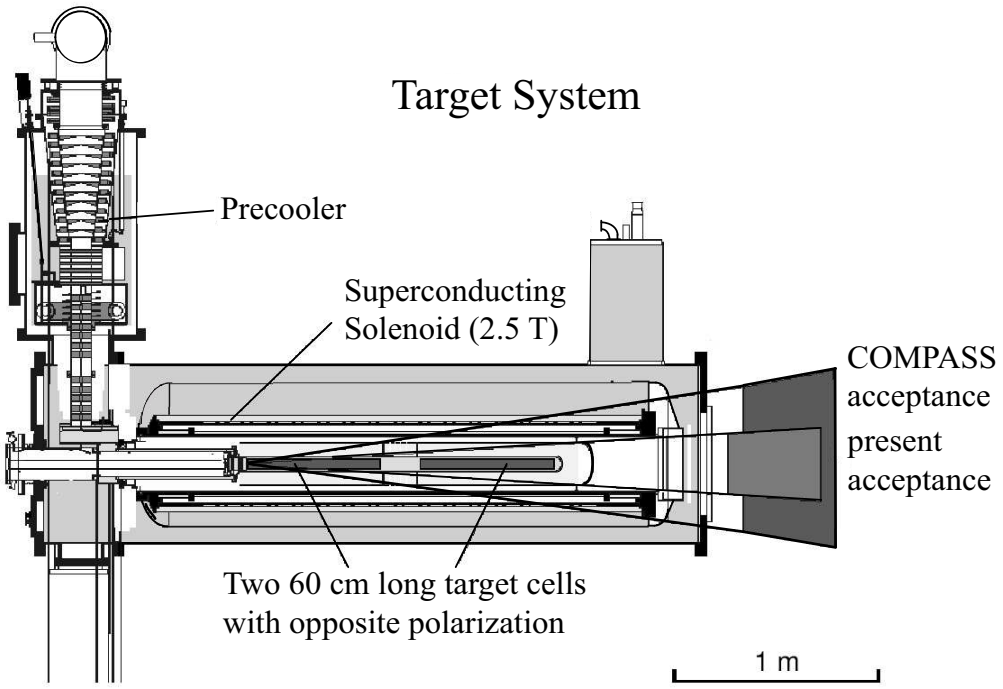

Figure 7.3: Schematic drawing of the SMC target as it is used in the COMPASS environment. The ^{3}He-^{4}He dilution refrigerator is operated at 50 mK. The magnetic field of the dipole is 0.5 T.

The experimental ambition to obtain $\Delta G/G$ is the measurement of the double spin asymmetry in Eq. 7.1 at highest precision. Since the beam polarization is fixed, the target polarization has to be inverted.

$$A^{exp} = \frac{N_{c\bar{c}}^{\Rightarrow\leftarrow} - N_{c\bar{c}}^{\Leftarrow\leftarrow}}{N_{c\bar{c}}^{\Rightarrow\leftarrow} + N_{c\bar{c}}^{\Leftarrow\leftarrow}} \tag{7.1}$$

Both target cells are longitudinally polarized with respect to the direction of the beam as shown in Figures 7.4 a)-d).

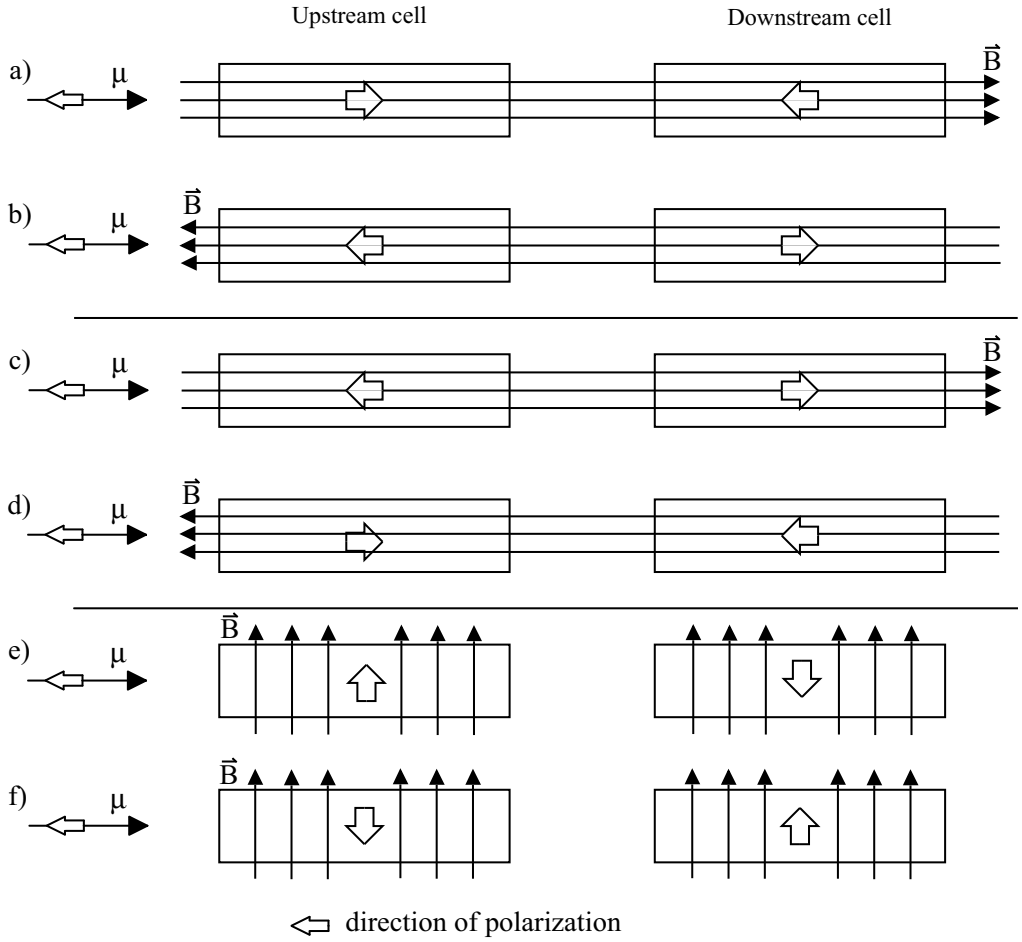

Figure 7.4: All possible spin configurations in the COMPASS experiment. The negatively polarized muon plus beam is incident from the left side. A transition from configuration a) or b) to c) or d) can be achieved by microwave field reversal.

The spins in the target can be reversed with respect to the beam by performing a so-called field rotation. As the nuclear spin follows the direction of the external magnetic field, the field can be changed from configuration a (c) to b (d) in Figure 7.4. In order to reduce the systematic error due to variations in the spectrometer efficiency and acceptance together with the slightly different amount of target material in the two cells this field rotation is performed every 8 hours. The measurement of the transverse spin-dependent structure function with a transversely polarized target is also part of the muon program. Such a spin configuration can be achieved by stopping the process of field rotation ad midst. The nuclear polarization is kept in the frozen spin mode at temperatures around 60 mK with a transverse magnetic field of 0.42 T. Starting with a field configuration like a) or b) in Figure 7.4, configuration e) can be obtained in about 15 minutes, as the dipole magnet can only be used in one field configuration. Correspondingly configuration f) can be obtained starting from c) or d).

The distance between both target cells is large enough to be able to allocate the correct cell during event reconstruction. The choice of target material for a polarized deep inelastic scattering experiment presents a challenging task. Taking the expression from Eq. 7.1, the measured asymmetries can be summarized by the simple expression

$$A^{exp} = P_T P_B \, f \, A^{\mu n \to c\bar{c}X}(x, Q^2), \tag{7.2}$$

with P_T as the target polarization, P_B the beam polarization, $A^{\mu n \to c\bar{c}X}(x, Q^2)$ the physics asymmetry of interest. The dilution factor f is defined as the fraction of events originating from polarizeable nucleons in the target and is a function of x and Q^2. At COMPASS ^{6}LiD is used as deuteron target and was polarized up to 55% at a magnetic field of 2.5 T during the 2003 run [40].

In the following part the process of polarizing the target material via DNP will be described in more in detail . Because of the Zeeman effect spin orientations of protons and electrons in the magnetic field belong to different energy levels, to result in a natural polarization. According to the Curie theorem one finds for spin $\frac{1}{2}$ particles that

$$P = tanh\left(\frac{\hbar\omega_0}{2k_B T}\right) \tag{7.3}$$

and

$$P = \frac{4\, tanh\left(\frac{\hbar\omega_0}{2k_B T}\right)}{3 + tanh^2\left(\frac{\hbar\omega_0}{2k_B T}\right)}, \tag{7.4}$$

for spin 1 particles with a given external magnetic field H, gyromagnetic ratio g, magnetic moment μ_B and spin temperature T_S, using $\frac{\hbar\omega_0}{k_B T_S} = \frac{g\mu_B H}{2k_B T_s}$. At 2.5 T magnetic field and a temperature of 500 mK electrons are polarized to 99.75%, deuterons to 0.05%. In the state of thermal equilibrium at temperatures below 1 K all electrons are in the spin states of lowest energies. Irradiation with microwaves of specific frequencies transfer the electron polarization to the protons. Using the possible spin states $|e \downarrow p \uparrow>$, $|e \downarrow p \downarrow>$, $e \uparrow p \uparrow>$ and $e \uparrow p \downarrow>$ a transition $|e \downarrow p \uparrow> \rightarrow |e \uparrow p \downarrow>$ can be induced using microwaves of the frequency $(\omega_e + \omega_p)$ as illustrated in Figure 7.5.

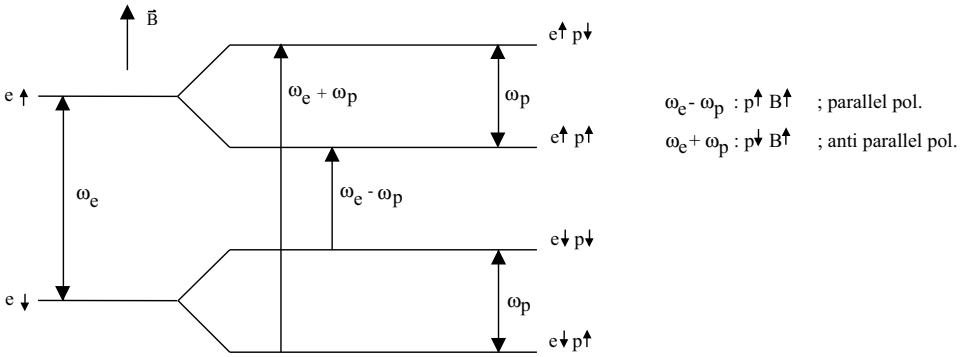

Figure 7.5: Energy levels, showing possible spin states. The electron and proton spin directions with respect to the magnetic field are indicated as e.g. e↑ and p↓ for parallel electron and anti parallel proton spin orientations, respectively.

Because of the large energy splitting of the electron energy levels the relaxation time is much shorter compared to that of the proton. During the same time period the proton spin remains unchanged while the electron spin flips back to its original state and is therefore again available as a polarization source. Finally polarization directions of protons and electrons are equal. Accordingly, a transition $|e \downarrow p \downarrow> \rightarrow |e \uparrow p \uparrow>$ can be obtained by irradiation with a frequency $(\omega_e - \omega_p)$. In the case of a $(\omega_e + \omega_p)$ transition the final proton spin polarization is anti parallel with respect to the magnetic field, while in case of a $(\omega_e - \omega_p)$ transition the final proton spin polarization is parallel with respect to the magnetic field.
This technique is used to go from configuration a) or b) in Figure 7.4 to configuration c) or d). Switching off the microwaves and simultaneously cooling down the target to about 50 mK leads to a freezing of the spin state. To reach temperatures in that region a ^{3}He - ^{4}He - dilution refrigerator is used at COMPASS [41,42].

The phase transition in a cold ^{3}He/^{4}He-mixture provides the cooling power needed, as two coexisting phases built up at temperatures below one Kelvin: 99.997% ^{3}He as concentrated phase with the diluted phase, where a small fraction ^{3}He is solved in super fluid ^{4}He. In the mixing chamber of the target both phases

exist. Pumping ^{3}He out of the diluted phase induces the dilution of helium atoms out of the concentrated phase. As this phase transition is endothermic, the temperature decreases. A good overview about the first results obtained with the ^{6}LiD polarized target at COMPASS is given in reference [43].

7.2 Small Area Tracking

The COMPASS tracking detectors can be classified into two subgroups: detectors for the small area tracking (SAT) : Micromegas (micro mesh gas detectors) and GEMs (gas electron multiplier) and very small area tracking (VSAT) where Scintillating Fiber Stations and Silicon Micro strip detectors are used.

7.2.1 Micromegas

Micro mesh gas detectors [44] use a similar operating principle as the GEMs. Instead of perforated foils copper meshes are used. The detector has an active surface of 38 $\times$ 38 cm^2 with a deactivated region of 2.5 cm diameter in the center. The distance between readout-strips in the central region is 360 μm, 420 μm in the outer regions. One station is made of two back-to-back mounted Micromegas, inclined by 45° respectively 90° in the y-plane. The spatial resolution is around 70 μm, time resolution is better than 10 ns and their efficiency for particle detection is better than 98%. The detector, as shown in Figure 7.6 consists of three electrodes: a drift electrode, the micro-mesh and the micro strips. An electric field of the order of 1 KV/cm decouples ions and electrons that generate an avalanche when they travel through the intense electric field of the amplification gap (30 - 50 KV/cm) between micro-mesh and micro strips (see Figure 7.7). The induced signal is read out via the readout strips. Between the polarized target and the first spectrometer magnet (SM1) three Micromega stations are operated with a gas mixture of Ne (80%), C_2H_6 (10%) and CF_4 (10%).

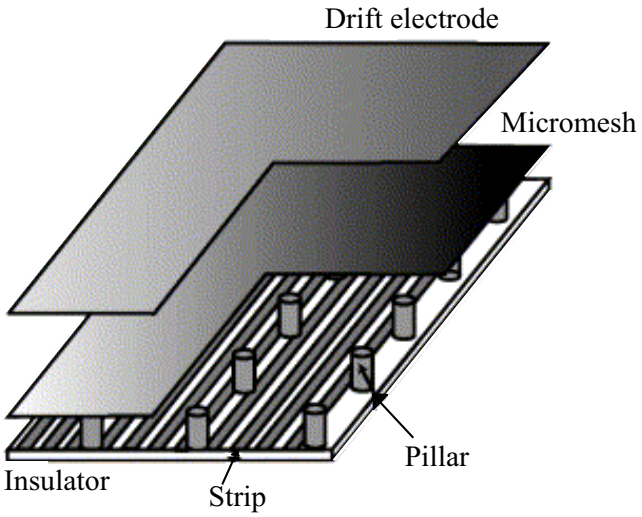

Figure 7.6: Schematical view of a Micromega detector.

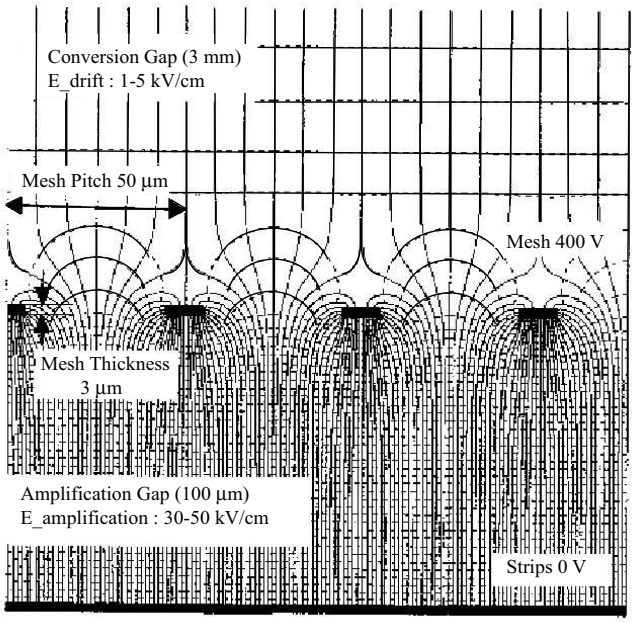

Figure 7.7: Electric field lines in a Micromega detector.

7.2.2 Gas Electron Multiplier Detectors

A GEM unit is made out of three kapton foils used for amplification with a regular hole-structure of 70 μm diameter ($\sim 10^4$ holes/cm^2). Figure 7.8 shows a photograph of such a foil.

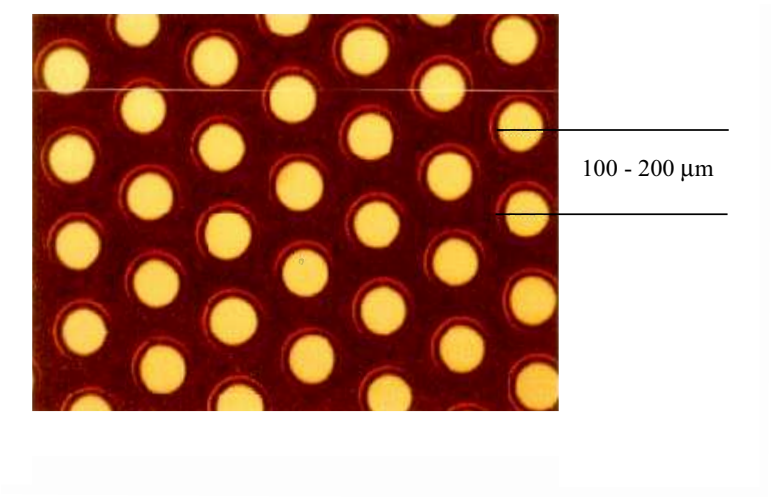

Figure 7.8: A photograph of a GEM-foil.

Each foil is coated on both sides with electrically conductive layer , having a potential difference between them. The amplification of the charged particles drifting through the field (50 KV/cm) occurs in these channels. The high density of field lines inside the amplification gap is shown in Figure 7.9.
The generated shower is read out by a two dimensional front-end card. The active area is 30×30 cm^2, where the central region of the GEM detector (5 cm diameter) is deactivated in order to protect the detector from high beam intensities. One station consists out of two layers, inclined by 45°, having four projections per station.

A spatial resolution of 46 μm, a time resolution of 15 ns and a particle identification efficiency higher than 97% is reached. GEM detectors are found at several places in the experiment: three stations are installed between the first spectrometer magnet SM1 and RICH-1, three between RICH-1 and the second spectrometer magnet SM2 and four between SM2 and Muon Wall 2.

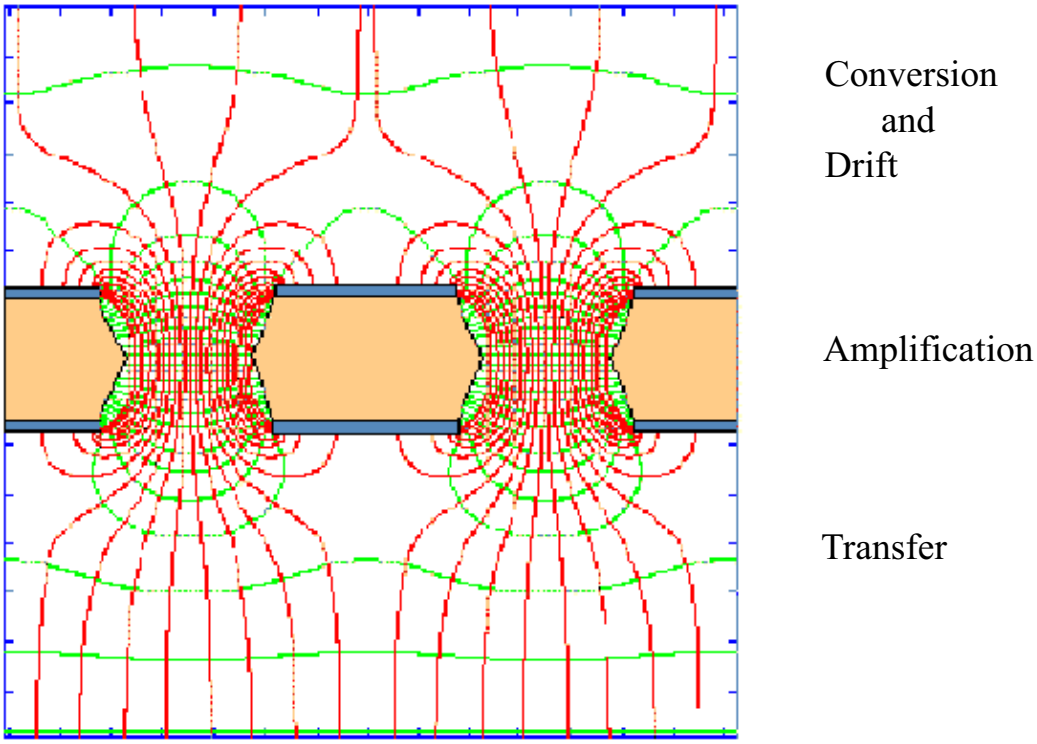

Figure 7.9: Electric field line configuration inside a GEM foil. The plot was created using the software package *Garfield*^{TM}.

7.2.3 Scintillating Fiber Stations

This type of detector is used for track reconstruction in the range of smallest angles and highest intensities in the beam, implying special demands on radiation hardness, spatial- and time resolution as well as dead time. With active areas of a few square centimeters they are located in the target region and downstream of RICH-1 and SM2. Figure 7.10 illustrates the arrangement of fibers into many stacks.

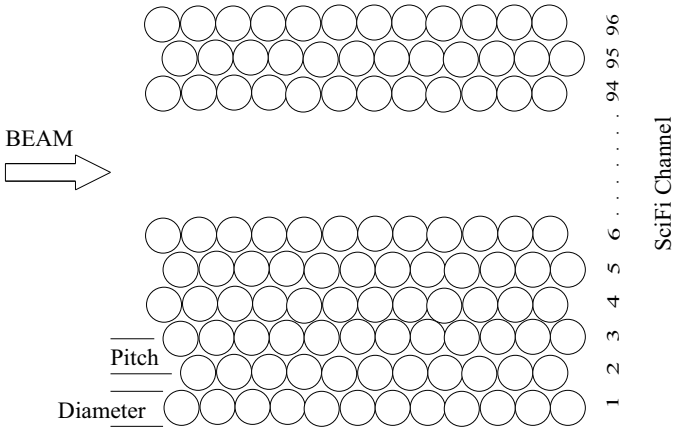

Figure 7.10: Schematic view of a SciFi plane with seven fibers per stack and 96 channels.

The active areas are 52.5 × 52.5 mm^2 with 384 channels for the Japanese detectors (Time resolutions are 400 to 500 ps, spatial resolutions 120 μm) and 123 × 123 mm^2 with 768 channels for the German detectors (Time resolutions are 370 ps, spatial resolutions 410 μm).

7.2.4 Silicon Micro strip Detectors

The silicon detectors , installed in the target region, are used for beam definition and small angle tracking. They provide high spatial resolution (up to 7 μm can be achieved) and precise time information (between 2 and 3 ns). The silicon wafer (70 $\times$ 50 mm^2 active area) has a readout pitch of 50 μm. The wafer has a thickness of 300 μm and can be read out both from the p- and n-side with orthogonal projections. Each detector consists of two stations, inclined by 5° and equipped with a two-dimensional readout (APV25 chips: 0.25 μm CMOS, 128 analogue inputs) resulting in four projections per detector. The readout chips are mounted on two L-shaped Printed Circuit Boards (PCBs), providing the electrical connections between readout chip and silicon wafer together with the cooling facilities needed for cryogenic operation. As the material budget should be as limited as possible, the cryostat with external dimensions of 240 $\times$ 240 $\times$ 82 mm^3 was machined out of stainless steel with two thin windows of 80 mm diameter made of 30 μm aluminized mylar. These are enforced with kevlar wires to guarantee mechanical stability when pressurized.

The Silicon detectors must cope with severe radiation exposure. Studies have shown that a detector which is already unusable at room temperature because of a dramatically decreased efficiency recovers its charge collection efficiency up to 80% when cooled down to liquid nitrogen temperatures. This phenomenon is known as the Lazarus effect. To utilize this effect, detectors are operated at low temperatures (130 K). During the 2003 run first tests of cryogenic operation were successfully performed. A more detailed summary and additional references can be found in [45].

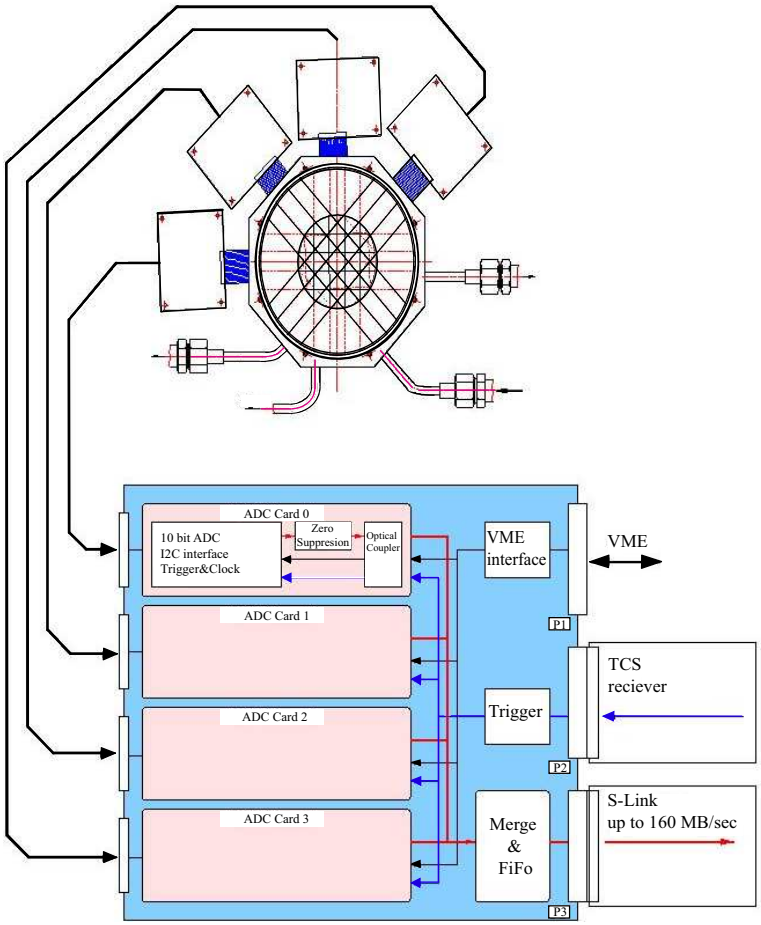

Figure 7.11: Schematic view of a silicon detector station including readout electronics.

7.3 Large Area Tracking

For the large area tracking drift chambers (DC), multi wire proportional chambers (MWPC) and straw detectors are used.

7.3.1 Drift Chambers

The drift chambers have an active area of 1.40 × 1.25 m^2. The central region (diameter of 30 cm) of this detector can be deactivated. These detectors are operated with a gas mixture of Ne (45%), C_2H_6 (45%) and CF_4 (10%) resulting in a maximum drift time of 70 ns. The particle identification efficiency is above 95%. One chamber consists of eight projections: two for each for the following orientations: ±20°, 90° and 0°. The distance between layers having the same orientation is 3.5 mm, whereas the pitch of a single layer is 7 mm. The distance

between cathodes of different projections is 10 mm, the spatial resolution is around 240 μm.

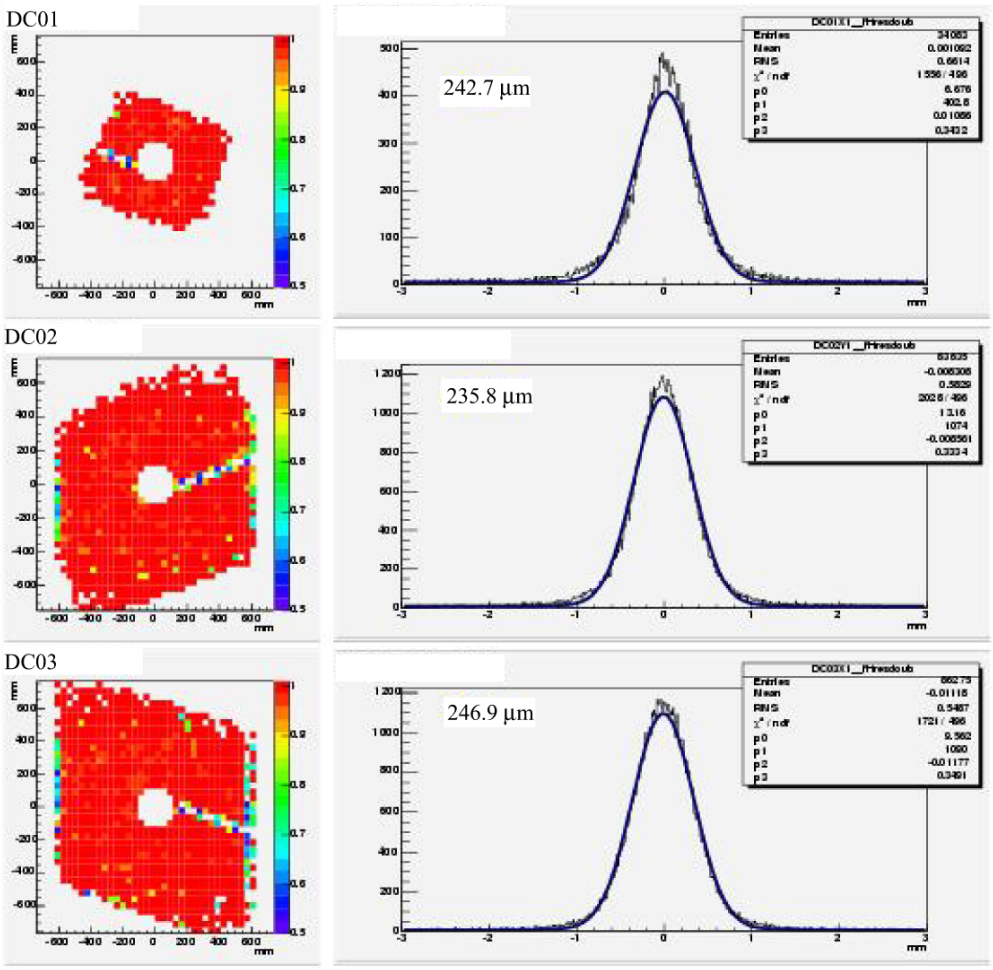

Figure 7.12: Left side: The efficiency for the three drift chambers is plotted. The dead region in the center is clearly visible. Right side: the spatial resolution is shown.

Additionally, Very Large Area Trackers (VLAT) with an active area of 2.40 × 5.00 m^2 (deactivated area with a diameter of 50 cm) and a drift space of 2 cm are used in the second spectrometer between SM2 and Muon Wall 2 under the name W4/5. The chambers are operated using the gas system of the MWPCs, providing a mixture of Ar (70%), CF_4 (20%) and CO_2 (10%).

7.3.2 Multi Wire Proportional Chambers

The MWPCs utilized at COMPASS have a wire spacing of 2 mm and a distance to the cathode of 4 mm. Depending on their location in the experiment they are equipped with three or four planes with the following orientations: 0°, ±10° and 90°. The active area is 1.5 × 1.2 m^2, again with a deactivated area in the central region of 16 cm to 22 cm, depending on the position along the beam line. They reach a spatial resolution of 500 μm. The time resolution is about 35 ns. They are operated with a gas mixture of Ar (70%), CF_4 (20%) and CO_2 (10%). At the nominal voltage of 4.25 kV their charged particle detection efficiency is higher than 99%.

7.3.3 Straws

A straw detector is built of drift tubes with a diameter of 6 mm and 10 mm depending on the location within the detector plane, respectively. Three double layers (see Figure 7.13) form one submodule, two submodules build one straw detector. The active area is 3.25 × 2.77 m^2, with a deactivated area of 23 × 16 cm^2 in the central region. The spatial resolution of each layer is around 250 μm. The timing resolution for the 6 mm straws is 33 ns and 55 ns for the 10 mm straws.

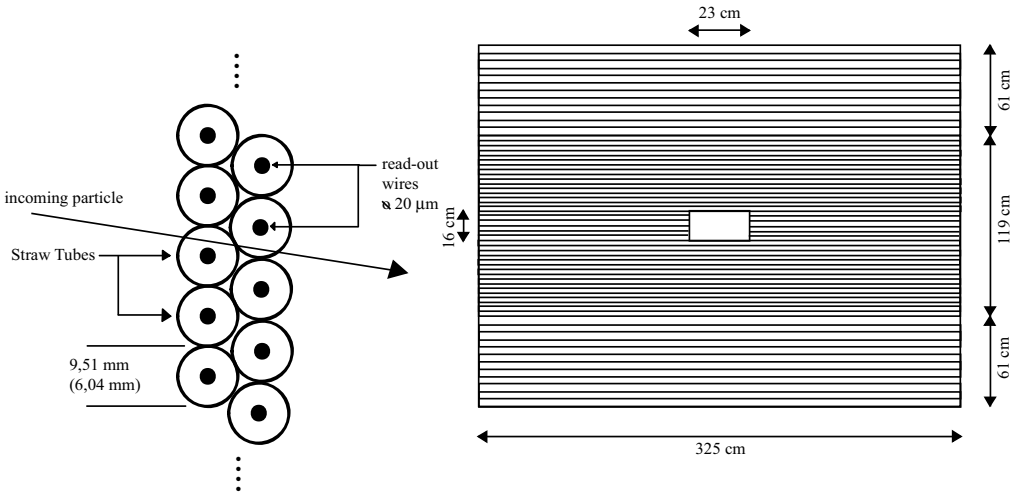

Figure 7.13: Left side: schematic view of a straw tube double layer, seen along the wires. Right side: straw detector seen along the beam line with 9.5 mm straws in the outer regions and 6.0 mm straws in the inner region of the detector.

During the 2002 run there were two Drift chambers (DC02 and DC03), followed by two submodules built up of three double layers each (ST03X1, ST03Y1, ST03U1

and ST03V1, ST03Y2, ST03X2) placed between the first spectrometer magnet SM1 and the RICH detector to compensate missing straw units. Another submodule was located downstream the RICH (ST04V1, ST04Y1, ST04X1). For the 2003 run two additional submodules were installed. The total setup now consists of two drift chambers (DC02, DC03) followed by two submodules (ST03X1, ST03Y1, ST03U1 and ST03V1, ST03Y2, ST03X2) between SM1 and RICH. One module is downstream the RICH (ST04V1, ST04Y1, ST04X1). The two new submodules are located behind the second spectrometer magnet SM2 (ST05X1, ST05Y1, ST05U1 and ST06V1, ST06Y1, ST06X1) To avoid interactions with the proton beam all large area trackers are equipped with a 4×4 cm beam window. Those 'vacant areas' are equipped with micro strip gas chambers and silicon detectors in the hadron-program, while scintillation fibers or hodoscopes are used in the muon setup. These measures improve the spatial resolution of the spectrometer.

7.4 Spectrometer Magnets

There are two bending magnets in the spectrometer. The key parameters are shown in Table 7.2.

	SM1	SM2
labeling	MEP 21/1	MEP 45
magnetic field [T]	0.49	1.60
current [A]	2500	5000
voltage [V]	600	600
turns	2×165	2×312
resistance [Ohm] (at 20°)	0.2	0.12
cooling water flow	540 l/min	150 l/min
weight [t]	120	400

Table 7.2: Specifications of the SM1 and SM2 magnet. The magnetic field of 0.49 T for SM1 is obtained with a gap size of 1320 mm. With a gap size of 920 mm the magnetic field is 0.70 T.

For the first spectrometer SM1 , the CERN magnet MEP 21/1, is used for both the muon (SM1m) and the hadron (SM1h) program. Two additional pole-pieces (1.525 m large, 1.100 m long with thickness from 0.250 m to 0.450 m) and two additional yoke pieces ($0.95 \times 1.72 \times 1.76$ m^3 (SM1m) and $0.95 \times 1.20 \times 1.76$ m^3 (SM1h)) are used to get the central gaps of 1.52 m and 1.00 m, respectively to form the magnetic field. Table 7.3 shows possible gaps for the SM1 magnet. The return iron yokes consist of four pieces of 100, 82, 50 and 40 cm height. Figure 7.14 shows the design of the SM1 magnet. SM2 is a classical air-core dipole with an aperture of $2 \times 1 \times 4.3$ m^3. Two water-cooled coils allow a maximum operating current of 5000 A.

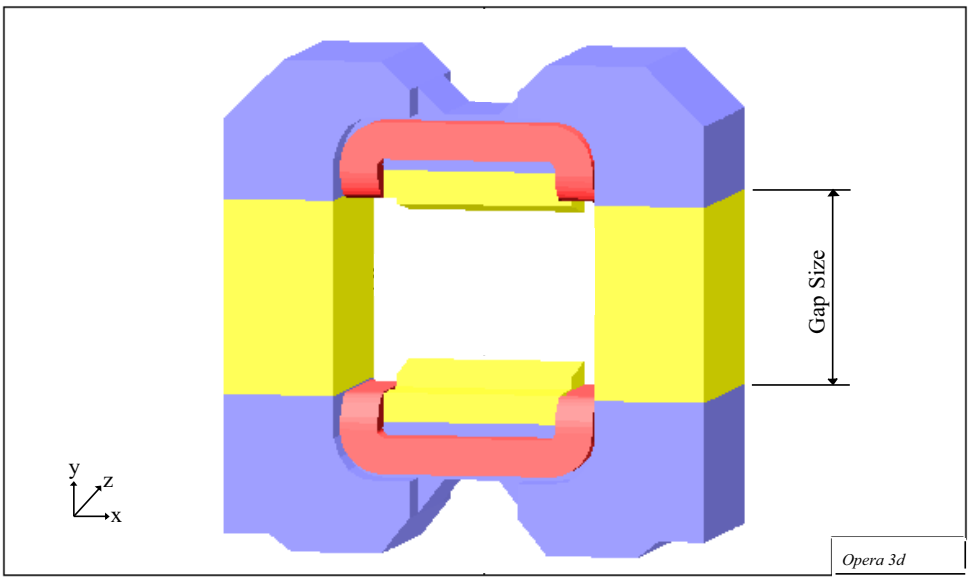

Figure 7.14: The SM1 magnet in the COMPASS setup.

	yoke dimensions [mm]				gap sizes [mm]			field integral [Tm]
	1000	820	500	400	exit	center	entrance	
1)	X	X	X	X	1720	1520	1320	1.00
2)	X	X	X		1320	1120	920	1.38
3)	X	X		X	1220	1020	820	
4)	X		X	X	900	700	500	
5)	X	X			820	620	420	
6)		X	X	X	720	520	320	1.76
7)	X		X		500	300	100	

Table 7.3: Different gap sizes for the SM1 magnet. Option 1) is the default configuration for the muon program.

7.5 Muon Filters

The muon filters (MF1 and MF2) are used for identification of scattered muons in the muon program and muons coming from semi leptonic decays in the hadron program. The muon track has to be correlated with additional tracking information upstream of the absorber. Because of multiple scattering inside the absorber, only limited spatial resolution is needed.

The general setup is similar for both muon filters. They consist of an absorber, made of 0.6 m of iron in case of MF1 and 2.4 m of concrete in case of MF2. These absorbers filter out hadrons and the tracking systems detect particles passing the absorber. The main purpose of MF1 is the detection of low energy muons (energies $\leq 25\ GeV$) from semi leptonic decays of charmed baryons. The fraction of muons from deep inelastic scattering processes with $y > 0.5$ hitting this filter is below 10%. Figure 7.15 shows the design of the two detector planes.

The first two muon detectors of MF1 are located downstream of the first hadron calorimeter (HCAL 1), followed by 0.6 m of iron absorber and two additional muon detectors. The tracking is done with plastic Iarocci tubes (PIT) [46], using a gas mixture of Ar (70%) and CO_2 (30%). Each station consists of four double layers with 10 mm pitch. The spatial resolution requirements are comparably low as multiple scattering of low energetic muons inside the absorber plays an important role (roughly 12 mrad for 10 GeV-muons): the spatial resolution is around 5 mm. Scattering in the calorimeters must be taken into account in order to correlate downstream and upstream tracks. Assuming that multiple scattering is of the order of 12 mrad for 10 GeV muons the spatial resolution needed is 0.5 - 1.0 cm.

The second muon filter (MF2) is used for the detection of high energetic muons coming from deep inelastic scattering and high momentum decay muons originating from charmed hadrons. The setup is located downstream of HCAL 2 behind 2 m of iron, where multiple scattering for 200 GeV muons is about 0.7 mrad. Using two detectors with a spatial resolution of 300 μm fulfills the demands. The setup consists of several components: 2 m of iron form the absorber. Aluminum drift tubes of 3 cm diameter are used as tracking detectors (gas mixture here: Ar (75%) and CO_2 (25%)). Six double layers form one module, with an active area of 4.0×2.0 m^2. The second absorber is made of 50 cm concrete to shield the trigger hodoscopes. The muon halo is the reason for a noise level of 50 - 180 Hz/cm^2.

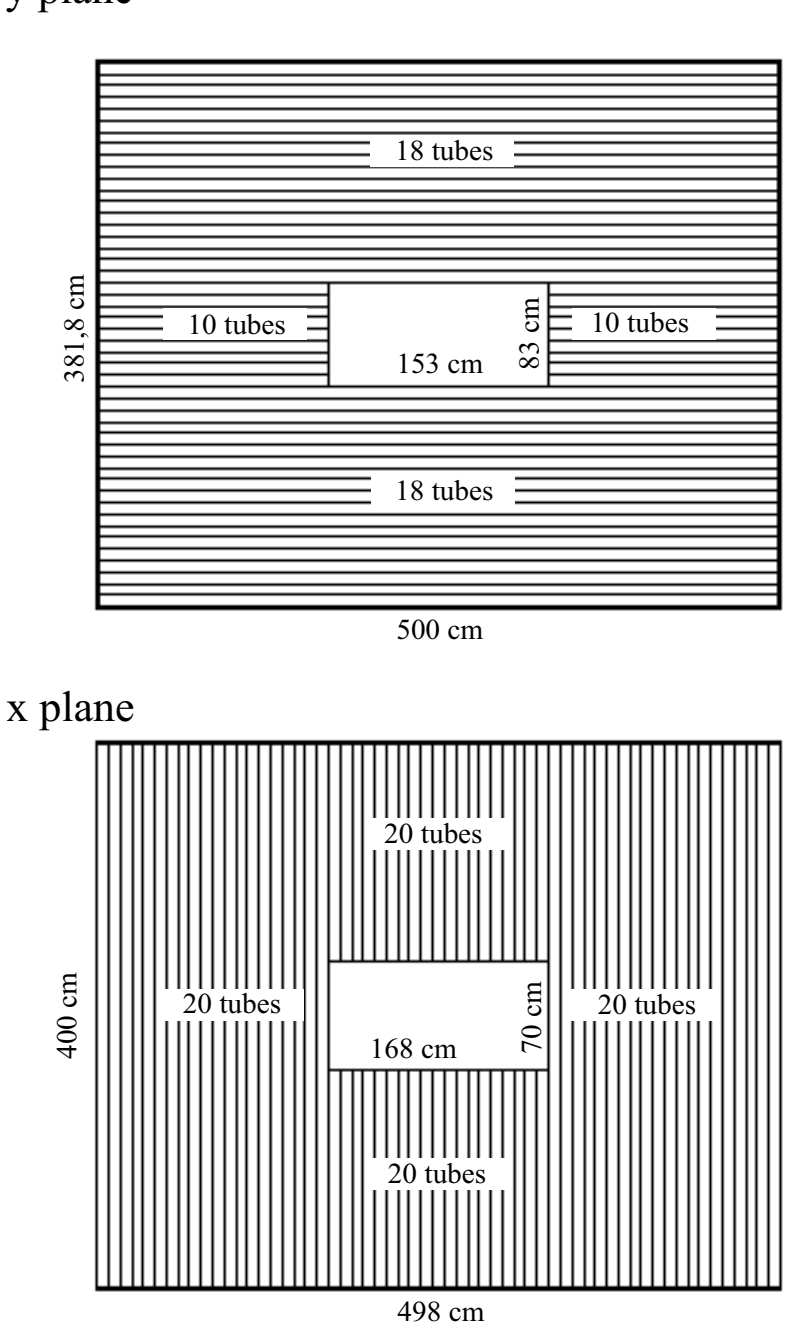

Figure 7.15: Schematic view of the X- and Y-planes of Muon Filter 1.The z-direction goes into the drawing surface.

7.6 Calorimetry

In the final setup a combination of two electromagnetic and two hadronic calorimeters is planned. The electromagnetic calorimeters are in the phase of being installed and tested. The design foresees lead glass, the central region of the downstream calorimeter consists of novel radiation hard $PbWO_4$-crystals. The first hadron calorimeter (HCAL 1) is mainly used for triggering purposes where moderate energy resolution is sufficient. Components from the WA102 [47] experiment are reused. The module size is $15 \times 15 \times 100$ cm^3 resulting in an active area of 4.2×3.0 m^2. The small angle calorimeter (HCAL 2) requires high resolution and is therefore designed as lead glass scintillator sandwich with modules of $20 \times 20 \times 120$ cm^3 forming an active area of 4.4×2.0 m^2. The readout electronics is identical for both detectors.

7.7 Trigger

The trigger system for COMPASS consists of various scintillators combined with the hadron calorimeter HCAL1. The trigger system is built of four groups of hodoscopes, labelled "inner", "ladder", "middle" and "outer" trigger covering a large $y - Q^2$-acceptance, see Table 7.4. Apart from the bending in the two spectrometer magnets, muons interacting in the polarized target can easily be mistaken for a particle passing the target without interaction in case of extremely small scattering angles in a ΔG/G-measurement. In order to avoid this the scattered muon is measured at two different positions along the beamline to determine the direction of the scattered muon μ' and to filter out halo muons going through the spectrometer in parallel to the nominal beam line. In respect to the second aspect a minimum amount of energy in the calorimeter is required coming from hadrons being produced in this reaction.

Trigger	$Q^2(GeV^2)$	y	type of event
inner	0-0.5	0.2-0.5	quasi-real photon emission
ladder	0-0.5	0.5-0.9	quasi-real photon emission
middle	0.5-1	0-0.9	inclusive DIS
outer	5-50	0-0.8	inclusive DIS

Table 7.4: The trigger system in the 2002 run.

In the COMPASS muon program there are two event classes which need a dedicated trigger mechanism: the so called 'ΔG' trigger which selects photon gluon fusion events and therefor triggers on quasi-real photon events with small four momentum transfer ($Q^2 \leq 1GeV^2$) and photon energies above a selected cut

value of typical $\nu_{min} = 0.3 \times E_{beam}$. This event class requires a hadron calorimeter signal to reject radiative and muon-electron scattering events in the trigger as well as low energy halo tracks. Secondly the 'DIS-trigger' for deep inelastic scattering events, where a minimal momentum transfer of $Q^2 > 1\ GeV^2$ is asked for. The acceptance is typically limited by the window size of the spectrometer magnet SM2 of 1×2 m^2 at about 20 m distance from the target. At a beam energy of 190 GeV this limits the four momentum transfer to about $Q^2 \simeq 80 GeV^2$ at x=1 and $Q^2 \simeq 28 GeV^2$ at x=0.1.
Looking at the photon gluon fusion trigger one finds two possible signals: the scattered muon and hadrons. Both are needed in order to select PGF events. In case of open charm production at least two mesons from a D^0 decay have to be reconstructed. In addition one has to distinguish between scattered muons and beam- or halo muons. Considering the fact that most of the beam- or halo muons have the full energy of 160 GeV scattered muons are characterized by at least 20% lower energy.
The photon energy has to provide sufficient invariant energy in the photon-gluon system to allow a perturbative treatment. s $\simeq$ 10 GeV^2 is considered as sufficiently high. The energy of the photon gluon subsystem is given by $s = x_G \times 2M \times \nu$. At low $\nu \approx 30(60)$ GeV this allows to sample gluons at $x_G > 0.16(0.08)$. A minimum relative energy loss of $y = \frac{\nu}{E_{beam}} > 0.3$ is needed to provide a sufficient photon polarization. An event with a sufficient invariant energy of the subsystem will produce either heavy quarks (charm) or a pair of high transverse momentum hadrons with $p_\perp > 1.5$ GeV.
This energy loss trigger is realized by three pairs of scintillator hodoscopes. Limiting factors are the existence of beam particles with lower energy, energy losses due to elastic muon-electron scattering and bremsstrahlung. The described trigger system selects all candidates with energies varying from the beam energy of 160 GeV. On the other hand, both event classes have one common feature: Apart from a muon that could be misleadingly interpreted as a scattered muon there are no hadrons produced. Using information from the hadron calorimeters HCAL 1 and HCAL 2 enables event selection with a hadron above a certain threshold energy in addition to a muon track candidate with a minimum energy loss coming from the target. Figure 7.16 explains the formation of the quasi real trigger, combining information from hodoscopes H4 and H5 together with HCAL. In the final setup of the COMPASS spectrometer both hadron calorimeters will have electromagnetic calorimeters (ECAL 1 and ECAL 2) upstream of them in order to protect them from electromagnetic showers initiated by electrons or photons. In the case of HCAL 2 there is a 10 cm thick lead wall used to shield from electromagnetic showers in the absence of ECAL 2. More detailed information can be found in [48].

Table 7.5 shows the development of the various detector components during the

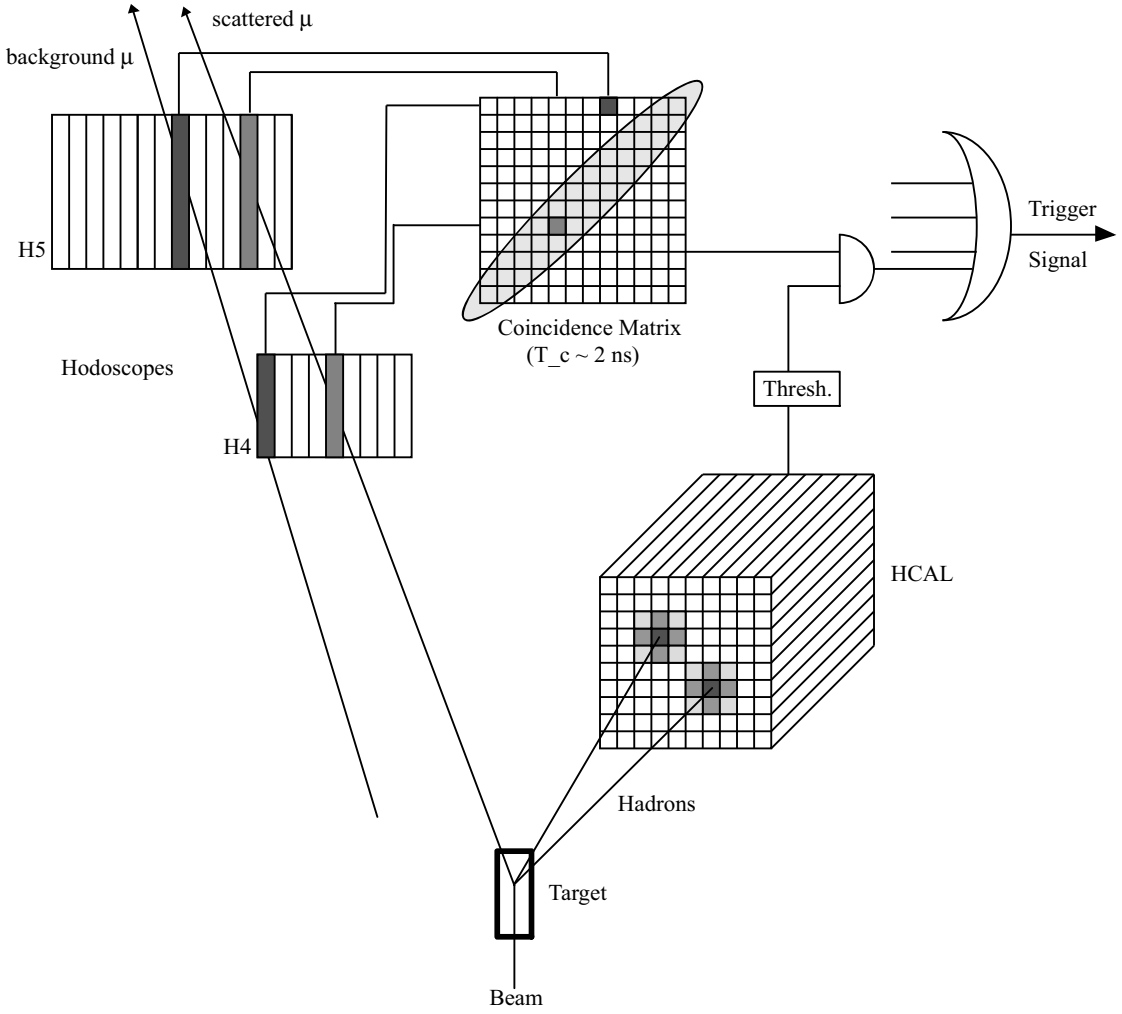

Figure 7.16: Setup for the trigger for quasi real photon events. It consists of two hodoscopes H4 and H5 for muon pointing and the hadron calorimeters HCAL 1 and HCAL 2 for hadron detection. The matrix for track selection and the quasi real trigger logic are also shown.

last three beam times.

Detector components	2001-Run	2002-Run	2003-Run
Drift chambers	not installed	3 stations	electronics upgraded, better resolution
GEM	7 stations	10 stations	
Silicon	3 projections	8 projections	8 projections (some of them operated at $130K$)
Micromegas	2 stations	3 stations	
Straws	1 submodule	3 submodules	5 submodules
MWPCs	not installed	14 stations	
W4/5	not installed	2 stations	4 stations
Muon filter 1	not read out	2 stations	active
Muon filter 2	1 double layer, only partially read out		active
HCAL 1, 2	active	active	active
ECAL 1, 2	not installed	not installed	50% of the readout ok e^--beam calibration done

Table 7.5: Comparison of the detector component status during the 2001, 2002 and 2003 run.

7.8 The Detector Control System

The main purpose of the Detector Control System (DCS) , often referred to as 'slow control', is to provide the control of all the relevant spectrometer parameters during long-term periods of data taking, as well as for beam tests during construction periods for all of the following detector components: RICH, Straws, MWPC, BMS, MW1, MW2, W45, target, SM1, SM2, trigger hodoscopes, japanese Scintillating Fibers, german Scintillating Fibers, Silicons and GEM. In total several thousand parameters are monitored (see Table 7.6). The temperature distribution analysis of the RICH vessel was performed using this system, see section 9.4.

It includes the monitoring and control of the High Voltage (HV) and the Low Voltage (LV) systems, gas supplies, racks and crates (with CAEN[1] bus) with electronics, slowly varying parameters (e.g. pressure, temperature), as well as experiment-wide infrastructure items, like cooling water supplies.

	Number of monitored parameters
crates with CAEN bus	27
other crates	22
HV standard	9104
HV special (ramp up, down, trip time)	4552
others	38
PLC	75
ELMB	380
Total	14200

Table 7.6: Total number of monitored parameters.

Figure 7.17 gives a schematic view of the COMPASS DCS.

[1]Costruzioni Apparecchiature Elettroniche Nucleari

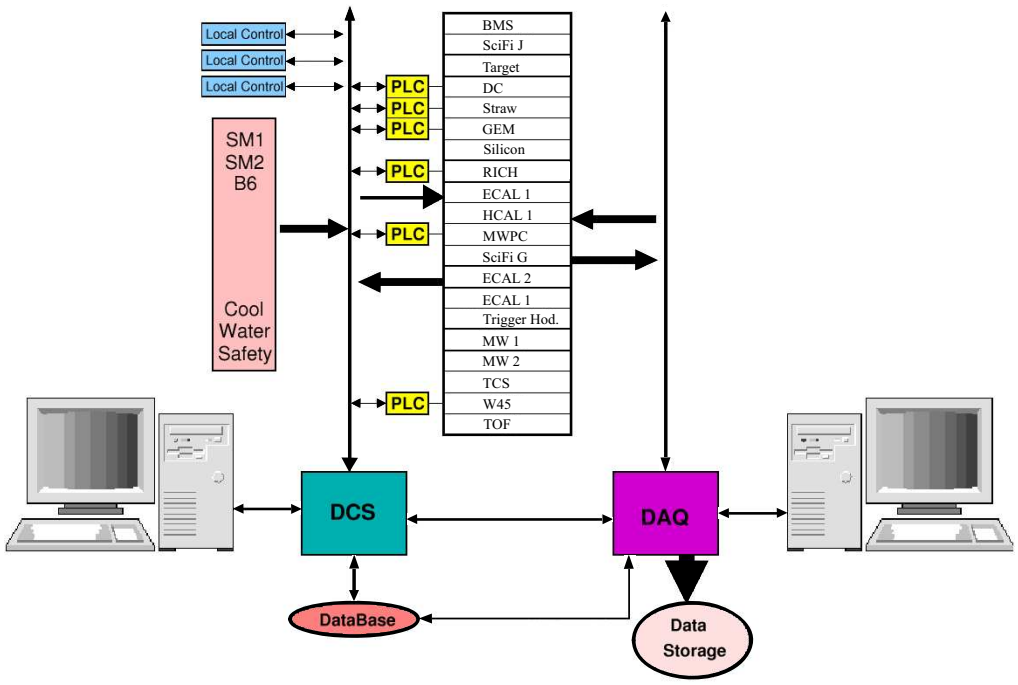

Figure 7.17: Schematic view of the COMPASS DCS system.

There are three main software components:

- Framework - the Framework is an integrated set of guidelines and software tools which is used by Developers to develop their part of the Control System application. When all parts of the application have been developed and integrated these form the complete Control System
- PVSS - a process visualization and control system
- DIM - (Distributed Information Management System) is a communication system for distributed/mixed environments. It provides a network transparent inter-process communication layer.

8 The COMPASS RICH-1 detector

The main RICH-1 requirements are the capability of separating pions, kaons and protons with momenta up to 55 GeV/c at high rates and minimizing the amount of material used to allow best performance of the more downstream electromagnetic and hadronic calorimeter together with the small angle spectrometer. The threshold momentum for Cherenkov photon emission is 2.5 GeV/c for pions, 8.9 GeV/c for kaons and 17.0 GeV/c for protons.

The key part of the RICH is the photon detection system which is made of multi wire proportional chambers equipped with segmented CsI photo cathodes. In order to cope with high multiplicities of hadronic interactions and with the photon halo of the muon beam, a segmentation into 80.000 channels is needed. To be able to have the photon-detectors mounted in the shadow of the first spectrometer magnet, a mirror wall is used to reflect the Cherenkov photons to the top and bottom half of the detector. In the future, a second RICH is planned to separate pions, kaons and protons with momenta up to 120 GeV/c.

8.1 Physics Fundamentals

In 1910, Mme. Curie observed blue light being emitted from radium solutions, without gaining deeper understanding of this effect [49]. Between 1926 and 1929 L. Mallet made the first quantitative observations, both photographic and visual, that asserted a continuous light spectrum. This was to be compared to the discrete spectrum of fluorescent radiation, which was studied during the same period. At that time neither the angular dependence nor the polarization of this radiation were observed. In 1934 P.A. Cherenkov and S.I. Vavilov discovered Cherenkov radiation as a bluish glow when radiating liquids with gamma-rays [50]. Vavilov explained that phenomenon by making Compton-electrons responsible and not photons. In 1937 I. Tamm and I. Frank presented a first quantitative theory [51]. The quantum formulation for this theory was elaborated by V.L. Ginzburg three years later [52]. In 1958 Tamm and Frank together with Cherenkov were awarded the Nobel Prize. They compared the phenomenon with the classical Huygens principle. A good summary of the evolution of the RICH technique can be found in [53–57].

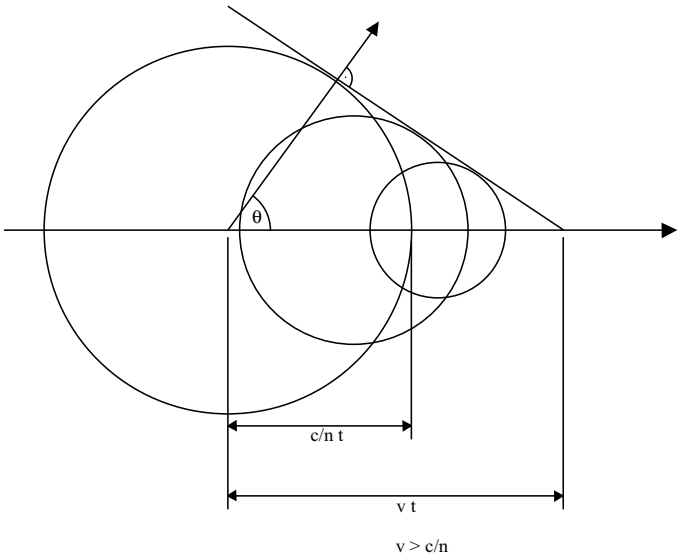

Figure 8.1: A schematic description of the Huygens Principle and the elementary wave dispersion.

When a high energetic particle crosses a dielectric, a part of the emitted light forms a wave front at a certain angle to the particle trajectory. This radiation is produced as soon as the velocity v = $\beta\cdot$ c of the particle is higher than the speed of light c/n in the dielectric, where n is the refractive index. Taking the Huygens construction (Figure 8.1) one observes that in three dimensional space the wave front forms a surface of a cone with the particle trajectory as the middle axis, with

$$\begin{aligned} \cos\theta &= (c \cdot \frac{t}{n})/(\beta c \cdot t) \\ &= \frac{1}{\beta n}, \quad \beta > 1/n. \end{aligned} \tag{8.1}$$

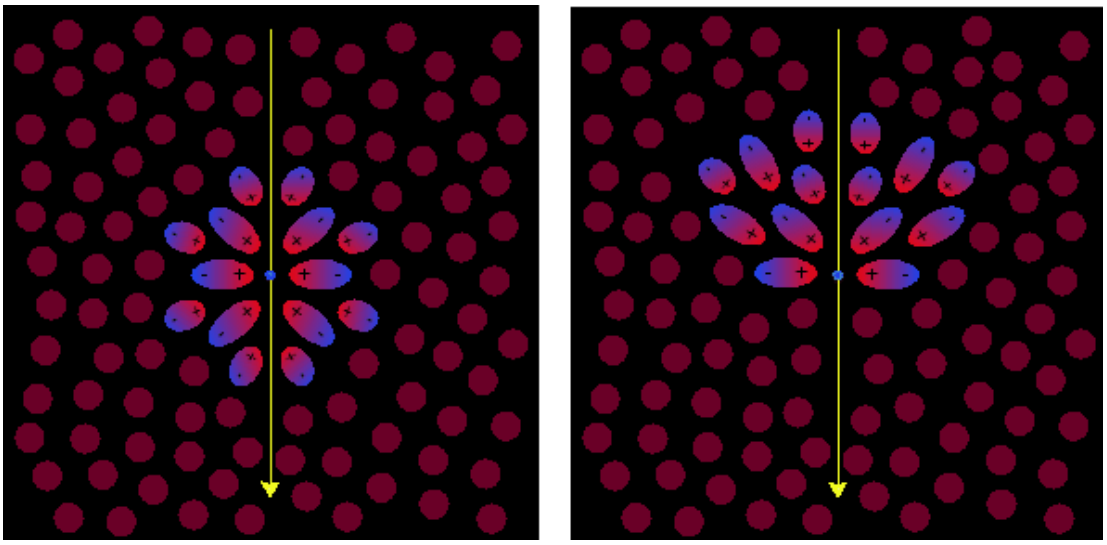

Figure 8.2: Left side: the speed of the particle is less than the speed of light within the medium. Thus the medium is symmetrically polarized with no resulting dipole field. Right side: for the particle velocity being larger than the speed of light within the medium, asymmetric polarization causes a dipole field which becomes manifest in electromagnetic radiation during the buildup of the field.

Observing a slow flying charged particle in a dielectric medium, the Cherenkov-radiator, induced polarization cancels out, resulting in no remaining field (left side of Figure 8.2 [58]). At velocities of the particle higher than the speed of light in the medium processes are different. As the influence of the charge propagates only with the speed v = c/n in a medium with refractive index n, one encounters a distorted charge distribution at higher particle speeds which results in a dipole momentum, ranging through the medium. Corresponding to classical electrodynamics, emitted waves cancel out via interference. Only on a cone with opening angle θ, the Cherenkov angle, there is constructive interference resulting in photon-emission (right side of Figure 8.2). It has to be taken into account that this model only applies under the following assumptions:

- The particle velocity must be larger than the speed of light within the medium, $v > \frac{c}{n}$,

- The total length of the medium passed must be substantially larger than the wavelength of the emitted wave, since otherwise diffraction occurs, $l_{radiator} \gg \lambda$,

- The Cherenkov radiation must be totally linear polarized, as the Poynting vector is perpendicular to the cone, $\vec{S} = \frac{c}{4\pi} \cdot (\vec{E} \times \vec{B}) \perp$ cone.

To specify the threshold speed the Lorentz-variable γ is used:

$$\gamma_{thres} = \frac{n}{\sqrt{n^2 - 1}}. \tag{8.2}$$

Using this equation one gets E_{thres} as minimum or threshold energy for Cherenkov emission for a particle of mass m crossing a dielectric with threshold γ_{thres}:

$$E_{thres} = m \cdot c^2 \cdot \gamma_{thres}. \tag{8.3}$$

The intensity and spectral distribution is given by the Frank-Tamm relation [59]:

$$\frac{dN_{Ph}}{dE} = \frac{\alpha}{\hbar c} \cdot Z^2 L \sin^2 \theta, \tag{8.4}$$

with d N_{Ph} being the number of photons in the energy interval [E, E + dE], α the electromagnetic fine structure constant, L the path length of the particle in the medium and Z the charge of the particle. With $\cos\theta = 1/\beta n$ one gets:

$$\frac{dN_{Ph}}{dE} = \frac{\alpha}{\hbar c} \cdot Z^2 L \left[1 - \left(\frac{1}{(\beta n)}\right)^2\right]. \tag{8.5}$$

The dispersion of an optical medium can be described with a function n = n(E). This has to be taken into account when integrating Eq. 8.5 in order to get the number of Cherenkov photons produced. Assuming a constant Cherenkov angle the integral over dE gives :

$$N = N_0 \cdot Z^2 L \sin^2 \theta, \tag{8.6}$$

with the number of detected photons N and the detector response parameter N_0 (Figure of Merit):

$$
\begin{aligned}
N_0 &= \frac{\alpha}{\hbar c} \cdot \epsilon \Delta E \\
&= (370\, eV^{-1} cm^{-1}) \epsilon \cdot \Delta E, \\
\epsilon \cdot \Delta E &= \int (QTR)\, dE,
\end{aligned}
\tag{8.7}
$$

with ϵ as energy average value of the detector efficiency (Q= quantum-efficiency, T= transmission, R= mirror reflectivity) with in the interval $[E_b, E_b + \Delta E]$. Cherenkov radiation has a continuous frequency spectrum. With a dispersive medium, n and θ are functions of the frequency ν. The energy loss per unit of path length can be derived from the Bethe-Bloch equation [60]:

$$
-\frac{dE}{dx} = K z^2 \frac{Z}{A} \frac{1}{\beta^2} \left[\frac{1}{2}\, ln\, \frac{2 m_e c^2 \beta^2 \gamma^2 E_{max}}{I^2} - \beta^2 - \frac{\delta}{2} \right], \tag{8.8}
$$

with K = 4 $\pi N_A r_e^2 m_e c^2$, E_{max} is the maximum energy that can be transferred in a single collision, I is the mean excitation energy and δ is a density effect correction to the ionization energy loss. The number of photons with a specific frequency or wavelength is proportional to d_ν or d_λ/λ^2 resulting in the observation of mainly blue light. Looking at a small frequency interval, the frequency dependent behavior of n can be neglected and taking Eq. 8.8, one sees that the energy dE, being emitted as Cherenkov light in the wavelength region ν_1 to ν_2 by a particle with charge Z $\cdot$ e per path length dx can be parameterized as:

$$
\frac{dE}{dx} = \frac{z^2}{2} \left(\frac{e^2}{\hbar} \cdot c \right) \left(\frac{mc^2}{e^2} \right) \Big((h\nu_1)^2 - (h\nu_2)^2/(mc^2) \Big) \Big(1 - \Big(\frac{1}{\beta^2 n^2} \Big) \Big). \tag{8.9}
$$

For a particle with z = 1 and $\beta = 1$, taking water as radiator (n = 1.33) this expression results in dE / dx = 400 eV cm^{-1} for the visible part of the spectrum (λ = 400 - 700 nm) and therefore one gets 200 photons per cm. This is only a small fraction of the total loss of energy of roughly 2 MeV cm^{-1}. The helpfulness of the Cherenkov-effect is due to the fact that measuring the angle θ in Eq. 8.1 directly gives the speed $\beta \cdot$ n. Table 8.1 lists several materials suitable as radiator for Cherenkov detectors. The data show that most regions for γ = 1.2 ... 100 are covered by solid, liquid, gaseous and aerogel radiator materials.
The velocity resolution σ_β/β is given as:

$$
\sigma_N/N = \frac{1}{\sqrt{N}} = 2\ cot\theta \cdot \sigma_\theta. \tag{8.10}
$$

Taking each cluster as the photon impact point on the detector reference plane with the emission polar angles θ_{clu} and ϕ_{clu}, θ_{ring} is the average of the θ_{clu} values in the peak of the ϕ_{clu} vs. θ_{clu} plot. σ_θ is the standard deviation of the $\phi_{clu} - \theta_{ring}$

Cherenkov Radiator Materials		
	$n-1$	γ (threshold)
Helium (NTP)	$3.3 \cdot 10^{-5}$	123.0
CO_2 (NTP)	$4.3 \cdot 10^{-4}$	34.0
Pentan (NTP)	$1.7 \cdot 10^{-3}$	17.2
Aerogel	$0.075 \ldots 0.025$	$2.7 \ldots 4.5$
H_2O	0.33	1.52
Glas	$0.75 \ldots 0.46$	$1.22 \ldots 1.37$
C_4F_{10}	$1530 \cdot 10^{-6}$	18.3
C_5F_{12}	$1720 \cdot 10^{-6}$	16.9
C_6F_{14}	0.28	1.61

Table 8.1: Properties of different radiator materials.

distribution and is taken as the single photon resolution. With $\sigma_\theta = cot\,\theta(\sigma_\beta/\beta)$ one gets:

$$\begin{aligned} \frac{\sigma_\beta}{\beta} &= \frac{tan^2\theta}{2\sqrt{N}} \\ &= \frac{n\beta\sigma_\theta}{\sqrt{N_0 L}} \\ &\equiv k_r, \end{aligned} \tag{8.11}$$

where k_r is known as the RICH detector constant . The resolution of a RICH detector for N photo-electrons is given as [59]:

$$\frac{\sigma_\beta}{\beta} = tan\theta(\sigma_\theta/\sqrt{N}), \tag{8.12}$$

with σ_θ as the total angular error per detected photon. The capability for particle identification of a RICH-detector can be illustrated using the variables u = $\sin^2\theta$ and u = 1 - $(\frac{1}{n})^2 - (\frac{m}{pn})^2$:

$$\begin{aligned} n_\sigma &= \frac{u_2 - u_1}{\sigma_u/\sqrt{N}} \\ &= \frac{m_2^2 - m_1^2}{p^2 n^2} \cdot \frac{\sqrt{N}}{\sigma_u}, \end{aligned} \tag{8.13}$$

with n_σ as the number of standard deviations for distinction of mass m_1 and m_2. Following [61] the momentum for particle identification with n_σ standard deviations

can be written as:

$$p = \sqrt{\left(\frac{(m_2^2 - m_1^2)}{2k_r n_\sigma}\right)}. \tag{8.14}$$

There are different types of detectors using the above described principle. The group of proximity focusing RICH detectors uses non-focusing optics to transmit Cherenkov photons to the photon detector (see Figure 8.3). This means the detector volume, known also as 'proximity gap', which is needed to enlarge the Cherenkov cone to a more convenient size for imaging, is placed between the radiator and the photon detector. This type of imaging was first proposed by Seguinot et al. [62] during the early design stages of the DELPHI experiment at CERN.

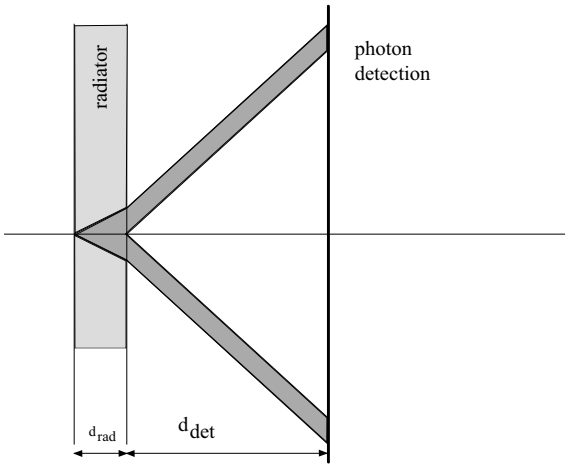

Figure 8.3: A schematic view of a proximity focusing RICH detector. The detector volume of thickness d_{det}, placed between the radiator (d_{rad}) and the photon detector, known as the 'proximity gap', is necessary to enlarge the Cherenkov cone to a more convenient size for the imaging.

A different approach uses a setup where photons travel through a liquid radiator and are then sent through an easy-ionizing gas. These photo-ionization electrons drift toward a multi wire proportional chamber, where a ring image can be extracted from the anode- and cathode signals. The radius of the ring is determined by the speed of the particle.

Photon detection	Experiment	Notes	Status
PM-based photon detectors	AMS	multi anode PMs	designed
	DIRC	PMs	started
	HERA-B	multi anode PMs	started
	HERMES	PMs	started
	LHCb	HPD/multi anode PMs	planned
	PHENIX	PMs	started
	SELEX	PMs	finished
photosensitive gases detectors	CAPRICE	TMAE	running
	CERES	TMAE	ending
	CLEO III	TEA	started
	CRID	TMAE	finished
	DELPHI	TMAE	finished
	OMEGA	TMAE	finished
MWPCs with CsI Photo cathodes	ALICE	HMPID	planned
	COMPASS		running
	HADES		running

Table 8.2: A variety of RICH projects arranged according to their photo detection technique.

Presently three different techniques are used in the main RICH projects:

- photomultiplier based detectors,
- photosensitive vapors inside the detector volume,
- multi wire proportional chambers with CsI photo cathodes.

Table 8.2 gives an overview of the application of these different approaches. In the first section standard photomultiplier tubes (PM), multi anode photomultiplier tubes or HPDs (Hybrid Photo Diode) are used. They provide a wide sensitive range, good rate capabilities and limited chromatic aberrations. Operating in the visible and near UV range, they provide a good Cherenkov angle detection. The second section comprises mainly detectors of the first generation that use TMAE (tetrakis-dimethylamino-ethylene) or TEA (triethylamine) as photosensitive vapor which makes the systems sensitive in the UV domain. In the third section multi wire proportional chambers with one cathode plane designed as a large segmented printed circuit board which is coated with a thin (hundreds of nm) layer of CsI [63] are used. These chambers need entrance windows with good transparency in the correspondent wavelength region, such as quartz windows in the case of ALICE or COMPASS.

8.2 The RICH-1 Setup

COMPASS is using a Ring Imaging Cherenkov Counter in which Cherenkov photons are focused on two photon-detectors via a spherical mirror surface resulting in very precise determination of the ring-radius (Figure 8.4). In the following chapters the different components are described: the vessel, forming the detector volume of about 83 m^3, the mirror wall, with the support structure for the 116 mirrors, the photon detection system and the radiator gas system. The minimization of the total amount of material used for the detector is of major concern. Tab. 8.3, 8.4, 8.5 and 8.6 summarize RICH 1-material , acceptance values and radiation lengths. In these tables the beam region is considered as the volume around the physical beam (which measures 7.6 $\times$ 8.9 mm in vertical and horizontal direction), taking a radius of 100 mm for lateral dimensions of this volume.

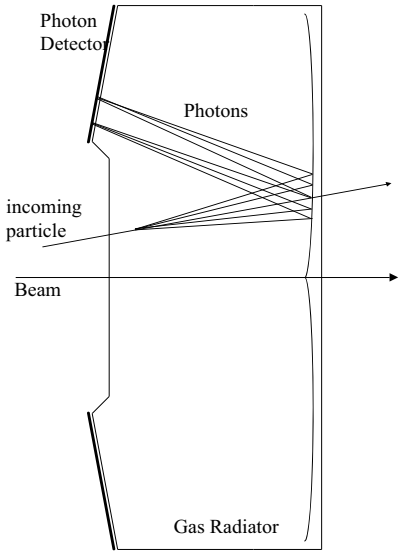

Figure 8.4: Scheme of the COMPASS RICH-1 geometrical arrangement. The incoming particles are reflected by two spherical mirror halves and reflected to the upper and lower photon detectors.

	l [cm]	X0 [cm]	X0 [%]
Upstream window	0.05 Al	8.9	0.6
Radiator Gas	340 C_4F_{10}	3241.0	10.5
Downstream window	0.05 Al	8.9	0.6
Total			11.7

Table 8.3: Overview: material used and radiation length inside of beam region (radius $<$ 100 mm) in the 2001 run.

	l [cm]	X0 [cm]	X0 [%]
Upstream window	0.18 Al equivalent	8.9	2.0
Radiator Gas	340 C_4F_{10}	3241.0	10.5
Mirrors	0.70 Pyrex	12.7	5.5
Mirror mechanics	0.20 Al equivalent	8.9	2.3
Downstream window	0.20 Al equivalent	8.9	2.2
Total			22.5

Table 8.4: Overview: material used and radiation length outside of beam region (radius > 100 mm) in the 2001 run.

	l [cm]	X0 [cm]	X0 [%]
Upstream window	0.05 Al	8.9	0.6
Radiator Gas	0.34 C_4F_{10}	3.24	0.01
He	3140	5281.0	0.06
Upstream light gas pipe window	0.01 Al	8.9	0.1
Downstream light gas pipe window	0.01 Al	8.9	0.1
Downstream window	0.05 Al	8.9	0.6
Total			1.6

Table 8.5: Overview: material used and radiation length inside the beam region (Radius < 100mm) in the 2002 run.

Vertical acceptance of the spectrometer	400 $mrad$
Horizontal acceptance of the spectrometer	500 $mrad$
Active area 'upstream' RICH	$3,2 \times 2,4\ m^2$
Active area 'downstream' RICH	$5,6 \times 4,0\ m^2$

Table 8.6: RICH-1 acceptance characteristics.

Several technological highlights have to be mentioned here: the internal window skins (both for the upstream and downstream windows are only 0.5 mm thick up to a radius of 250 mm. The upstream and downstream windows are a composite structure made out of 1 mm Al foil + 40 mm (upstream window) respectively 50 mm (downstream window) of Klegecell foam[1] + 1 mm Al foil.

Looking at Table 8.4 the most dominant contribution to the overall radia-

[1]Density: 0.055 g/cm^3; composition (weight): Cl : H : C $\sim$ 57 : 5 : 38.

tion length within the beam region (radius $< 100\ mm$) is the radiator gas itself. A light gas pipe filled with He at atmospheric pressure was installed before the 2002 run. It screens the inner beam region (Tab. 8.5), which resulted in a decrease of radiation length of 92.9% (Table 8.4 and 8.5 to be compared). This pipe was manufactured using cutting-edge technology: e.g. welding of ultra-thin Al foils to introduce as little as possible material into the vessel. Table 8.7 outlines the specifications.

Piece	Material	Dimension [mm]
Pipe	Al	100 (diameter) 0.15 (thickness) 3140 (length)
End caps	Al	0.10 (thickness)

Table 8.7: Specification of the light gas pipe.

	Proposal	2002 Run	2003 Run
Number of photons/ring	36	19, 75	21,1
Mirror surface	100%	95%	95%
Mirror reflectance	89%	85%	85%
Active surface	95%	78%	78%
Single photon detection eff.	85%	$75 - 80\%$	$75 - 80\%$
$(n-1) \times 10^6$	1530	1220	1260
Quartz transmission	85%	83%	83%
Gas contamination	5 ppm O_2 5 ppm H_2O	4 ppm O_2 5 ppm H_2O	1 ppm O_2 3 ppm H_2O

Table 8.8: A comparison of the RICH-1 design values according to the proposal and properties during the 2002 and 2003 runs.

Table 8.8 compares design values for the number of photons per ring, optical properties of the mirrors, efficiencies and gas contamination. A slightly lower amount of impurities during the 2003 run resulted in a higher number of photons per ring.

Figure 8.5 shows a superimposed graph of quartz and radiator gas transparencies, mirror reflectivity, CsI quantum and single photon efficiencies. Taking all these curves into account the optimum wavelength interval for the operation of the system is in the interval [165, 185 nm]. The strong drop of the quartz transparency for photon wavelengths below 180 nm together with the maximum for the single photon efficiency around 175 nm sets these limits.

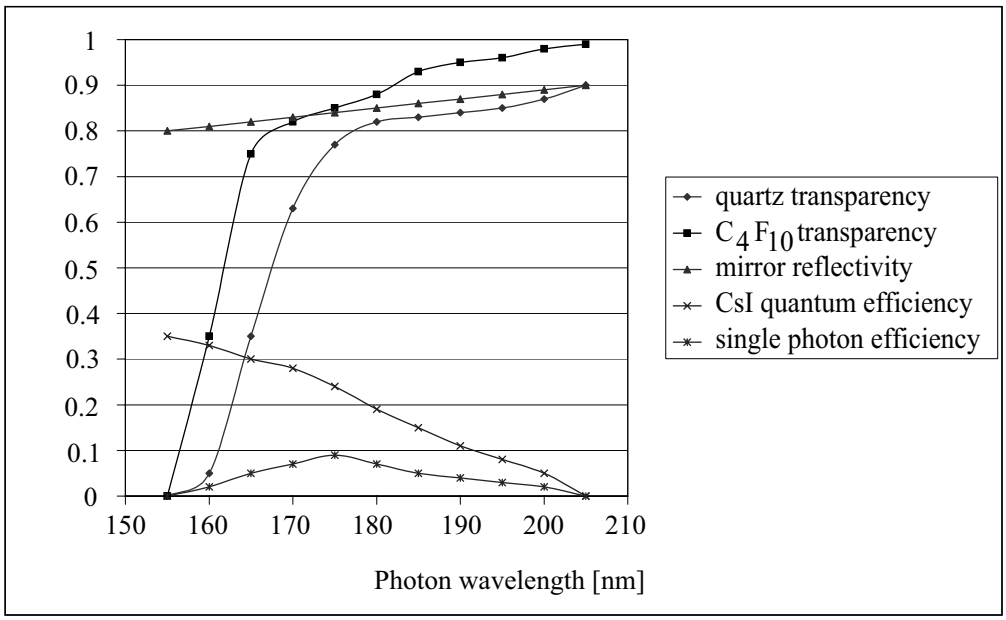

Figure 8.5: Graphics of quartz and C_4F_{10} transparency, mirror reflectivity, CsI quantum efficiency and single photon efficiency.

8.2.1 The Vessel

With outer dimensions of $6.6 \times 5.3 \times 3.3$ m^3 the RICH-vessel is one of the largest component of the COMPASS-experiment. Below the individual components of the vessel are listed: the inner frame, which is made of stainless-steel pillars and beams, forms the framework and provides the stability and stiffness needed. Mechanical precision is not needed. Several frames form the connection between the above mentioned framework and the elements closing the vessel which have to be mechanically precise. Each of these frames consist of two components - one piece is fixed at the framework-structure with the possibility to be aligned precisely with the vessel-skin before welding. The other piece is bolted together with the first mentioned piece. In total five constructions of this design are used:

- a front-frame for the entry-window,
- a backward-frame for the exit-window,
- two detector-frames, which keep the upper and lower photo-detectors,
- one door-frame.

Inside the vessel a special frame keeps the mirrors, ensuring exact positioning and durable fixation of each single mirror. Hooks are mounted on top of the vessel to allow movement of the whole vessel with a crane. Underneath the vessel adjustable feet are situated allowing alignment and fixation of the structure on the rail system in the experimental area.

The external mantle of the vessel is made of a thin stainless steel foil, that is welded on the supporting structure below. Figure 8.6 shows the total setup without the closing windows and without the mirror wall inside. The front and rear windows are sandwich-constructions, consisting of two thin aluminum foils with one layer of solid foam in between. The radiation length per window is about 2%. The surface of the largest composite panel is $> 20\ m^2$. During the 2003 run the leak rate of the vessel was determined for the first time taking pressure and temperature changes together with the changing level of liquid in the storage tank into account. Because of the temperature and external pressure dependent 'breathing' of the system, values are fluctuating. Determination of a trend line over a period of 90 days shows a leak rate of roughly 90 l of gas per day (see Figure 8.7) .

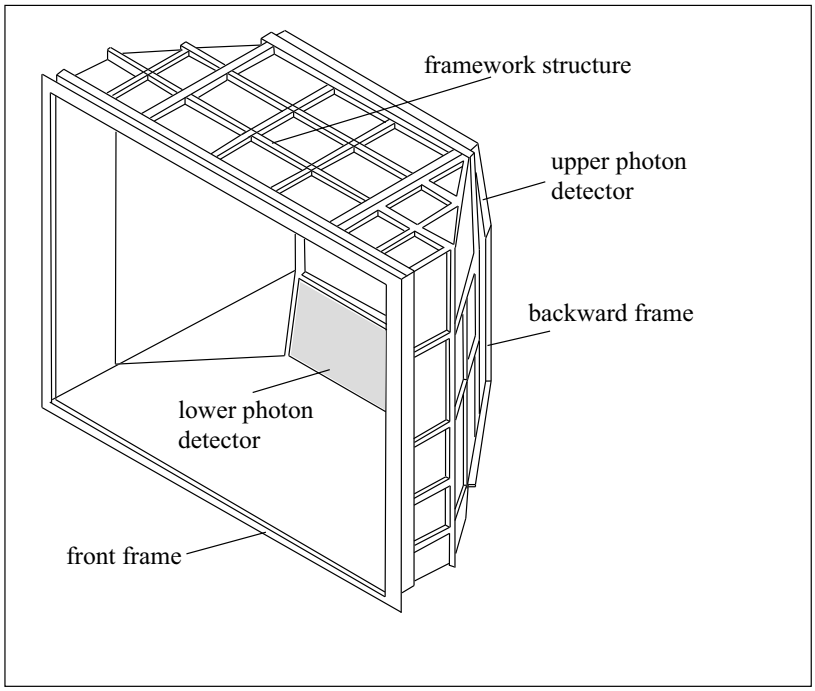

Figure 8.6: RICH-1 vessel structure.

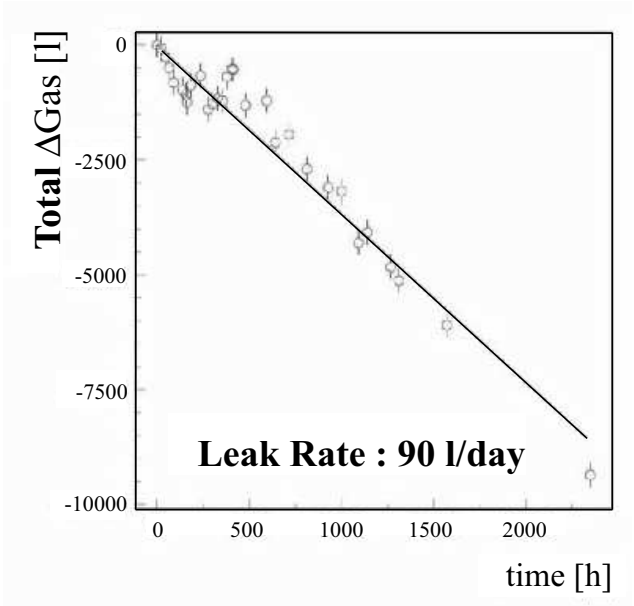

Figure 8.7: Measured leak rate of the RICH-1 vessel during the 2003 run.

8.2.2 The Mirror Wall

The mirror system [64] consists of spherical mirrors with a radius of curvature of 6.6 m, divided in 116 hexagonal and pentagonal elements with centers vertically displaced by 1600 mm up and down with respect to the beam axis, because the image should be focalised outside the spectrometer acceptance. The clearance left between adjacent mirrors results in a total loss of 4% of reflecting surface. With a total area of more than 21 m^2 they form two spherical surfaces to focus the Cherenkov-photons on two photon-detectors located above and below the acceptance region. Local deviation from perfect spherical shape is only tolerable up to $\sigma_\theta = 0.2$ mrad, deviation of radius of single mirrors up to $\sigma_{R/R} = 0.5\%$. The mirror substrates are borosilicate glass of 7 mm thickness. There were 126 (including 10 spare) units produced by IMMA[2] with individually characterized values for the radius of curvature R, the spot diameter D and the roughness of the polished surface. These values are summarized in Table 8.9.

number of mirrors	116
radius of curvature	$6606 \pm 20\,[mm]$
spot diameter	$1.65 \pm 0.45\,[mm]$
surface roughness	$1.26 \pm 0.11\,[nm]$
reflectance	$83 - 87\,\%$
substrate thickness	$\leq 6\,\%$ radiation length

Table 8.9: Overview: mirror characteristics.

To obtain the required reflectance in the VUV region the reflecting layer of $\sim$ 80 nm Al and the protective layer of $\sim$ 30 nm MgF_2 have to be deposited using an optimized and controlled procedure. This delicate part of the production was performed at the CERN reflectometer facility [65]. The long term stability has been considered important from the beginning. The evolution of reflectance after two years of operation is shown in Figure 8.8.
The mechanism to position and fix (angular resolution ~ 0.2 mrad) a single mirror must be lightweight and markedly stiff at the same time. A composite material of Al_{95} : Fe_4 : $Brass_1$ with an almost negligible contribution of stesalite is used. The stability of the structure in conjunction with the RICH-vessel was calculated using a finite element method (FEM), the design was modified and optimized later in substantial simulations. A net-like configuration with the nodal points, where the mirrors are suspended to, laying on a highly precise sphere was chosen. The aluminum structure is made of the following components:

[2]IMMA, Ltd., Kinskeho 703, Turnov, Czech Republic

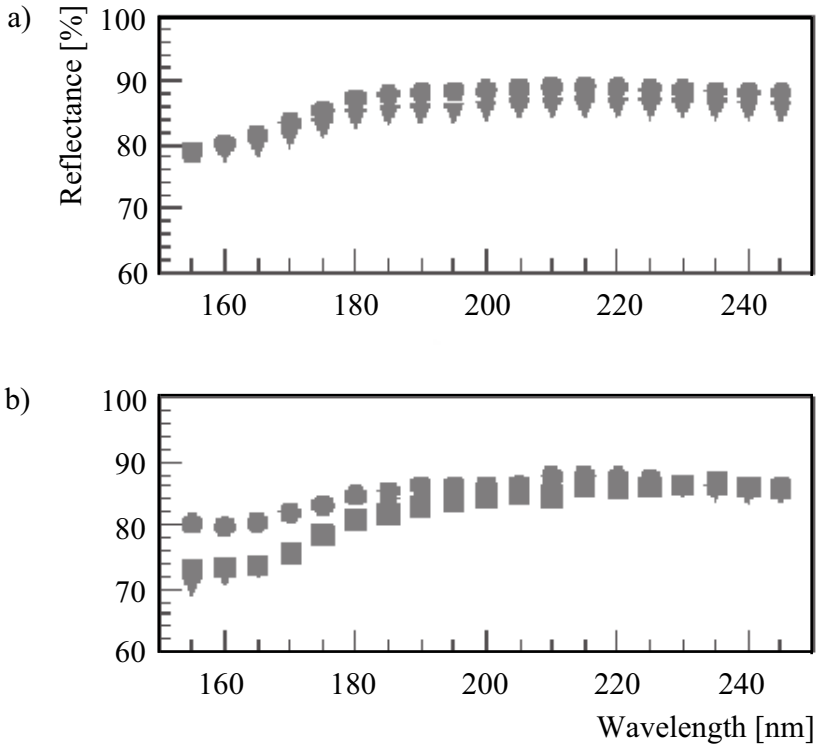

Figure 8.8: (a) shows the mean value of the measured reflectance for all 126 mirrors at the mirror center (dots) and at the mirror edge (triangles) right after production. (b) shows the reflectance of one single mirror directly after production (dots), and after one and two years (squares and triangles) of operation inside the vessel.

- a rectangular outer frame which is outside the acceptance of the spectrometer. Dimensions are 6.05 × 4.85 m^2. This frame is screwed to the rear flange of the vessel,
- a double-spherical structure of high mechanical precision, with connection points where the mirrors are attached,
- the joints, being a complex mechanism connecting the mirrors to the above mentioned structure and allowing the alignment of the mirrors. Each individual element can be rotated around two orthogonal axes with the help of micro metric screws with a precision of 2.5 mrad / turn. The weight of one joint unit is 112 g.

The dimensional precision of the final structure, not including the mirrors themselves, is measured to be ± 1 mm with a total radiation length of 2.5%. A more detailed description of the mirror mounting and alignment is provided in [64]. Figure 8.9 shows the mirrorwall and the light gas pipe, seen from the downstream side with the photon detectors removed from the vessel.

Figure 8.9: Photography of the mirrorwall seen from the downstreamside with the photon detector being removed from the vessel. In the lower half the light gas pipe is visible.

8.2.3 Photon Detection

Taking into account that the surface to be equipped with photon detectors is 5.3 m^2 large, multi wire proportional chambers with segmented CsI photo-cathodes were chosen. This type of UV-photon-detector was developed in collaboration with the RD-26 group [63] at CERN and will be also used at ALICE and other future projects. RICH-1 is equipped with eight identical chambers, with a surface of 576 $\times$ 1152 mm^2 each. Photo cathodes are made of two 576 $\times$ 576 mm^2 double sided Printed Circuit Boards (PCB). The silica-quartz windows consist of two identical quartz-plates (600 $\times$ 600 $\times$ 5 mm^3). Special care is needed handling the PCBs with CsI-deposit, because exposure to an atmosphere with more than 100 ppm of oxygen has to be strictly avoided. Segmentation of the photo cathodes (pixel size: 8 $\times$ 8 mm^2) results in 82.944 channels, provided with analog readout-electronics. Expected occupancy level is $\sim$ 5% at a maximum trigger rate of 10^5 s^{-1}, resulting in a maximum data flow of 2.5 GB/s. COMPASS-Gassiplex chips are used as front-end-chips [66]. These are modified versions of the chips developed for RD26, now equipped with preamplifier, shaper and an analog-multiplexer. The intrinsic dead time is 400 nsec per event, with a peaking time of 1 μsec. The value for noise is as low as 1100 electrons equivalent at a gas amplification of $\sim$ 6.5 mV / (fC). Figure 8.10 shows the setup of the photon-detector in layers.

The core piece of the readout system is the total amount of 192 front-end-cards, the 60 cm long BORA boards [67], hosting the front-end chips and a first trigger level. There are 24 BORA-boards per photon chamber handling 432 analog channels. Each single BORA-board is equipped with front-end-chips, ADCs (analog digital converter), FIFOs (first in first out buffer), FPGAs (field programmable gate array) of the type VIRTEX XCV100 [68] for logic sequencers, threshold-subtraction and zero-suppression, 32-bit DSPs [69] for event packaging, on-board controls and optical links. The event processing time is $10\mu sec$. The control system for those BORA-boards is a parallel network of DSPs (digital signal processing), operated via a dedicated PC-PCI-interface: the DOLINA-boards with 8 on-board DSPs each. To avoid grounding interference between the PC and the detector all BORA-boards are optoisolated from DOLINA with the help of specific optoisolating boards. Figure 8.11 sketches the architecture of the readout system.

The photon detectors reach an absolute gain of 10^4 at nominal voltage of 2000 V with photon detection efficiencies of about 75% as presented in Figure 8.12.

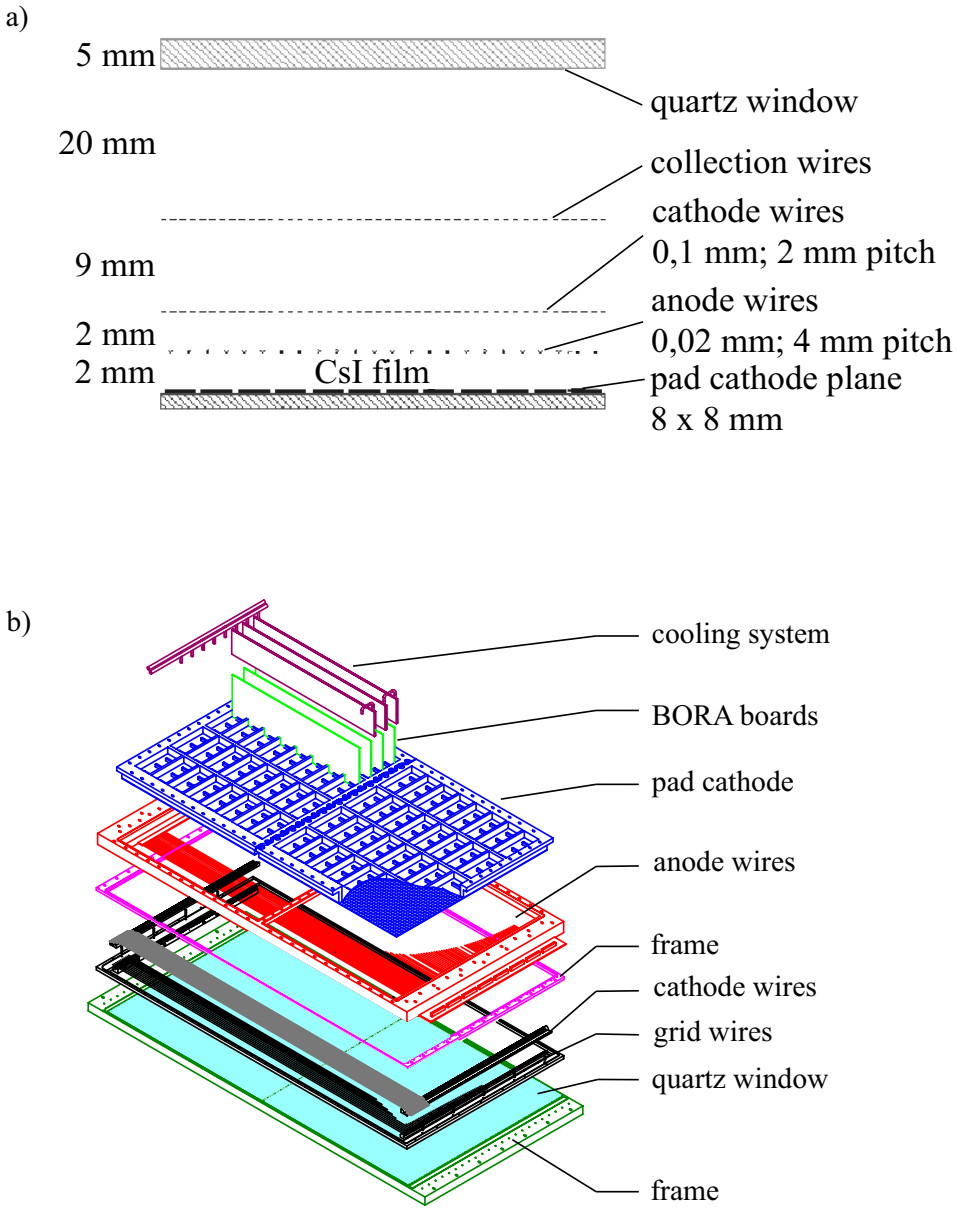

Figure 8.10: Schematic design of a RICH-1 photon detector. a) Side view of a photon detector. b) 3-D sketch of a photon detector, including (from bottom to top) a detector frame, the quartz window, the cathode- and anode wires, the pad cathode, the front end boards and the cooling system.

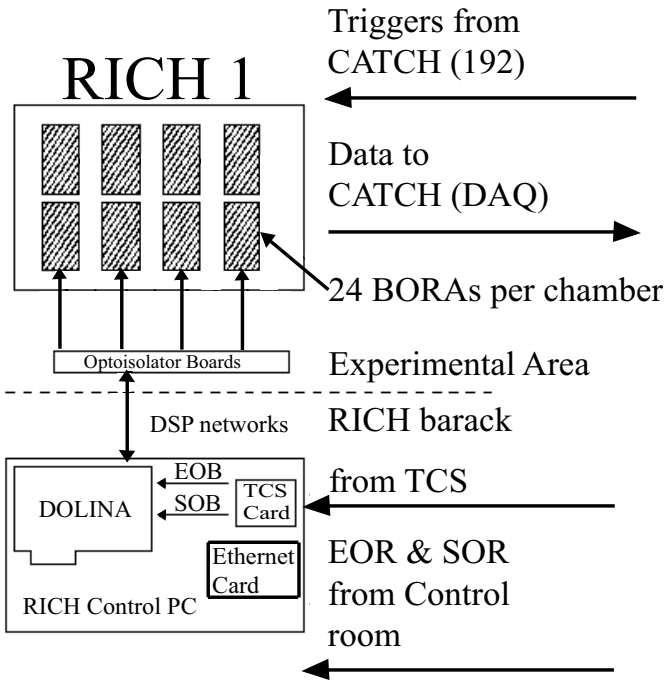

Figure 8.11: Schematical design: RICH-1 readout architecture.

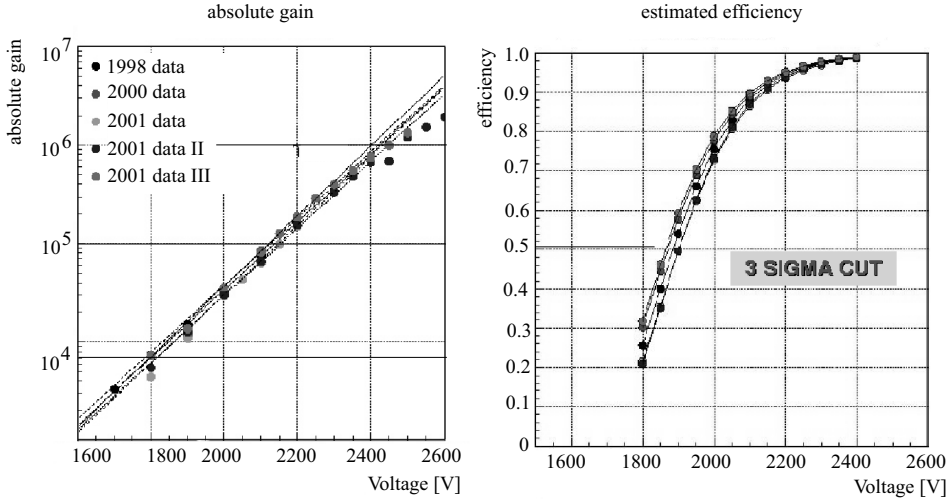

Figure 8.12: Calculation of the absolute gain and photon detector efficiencies. Left side: the absolute gain is linear up to 2300 V. Standard operational voltages are around 2000 V, which corresponds to a gain of 3×10^4. A Ru-source was used. Right side: applying a 3 σ cut the photon detector efficiency was measured to be around 75% for an operational voltage of 2000 V.

Figure 8.13 shows the on line event display for two representative running conditions with varying beam-, photon detector- and radiator gas conditions. The rings are distributed over several photon detectors. For the low intensity run on the left side of Figure 8.13 the background is less visible compared to a run with nominal beam intensity as shown on the right side of Figure 8.13. The substantial difference in the amount of C_4F_{10} has to be noticed. Figure 8.14 shows a zoomed view of one ring being distributed over two photon detectors.

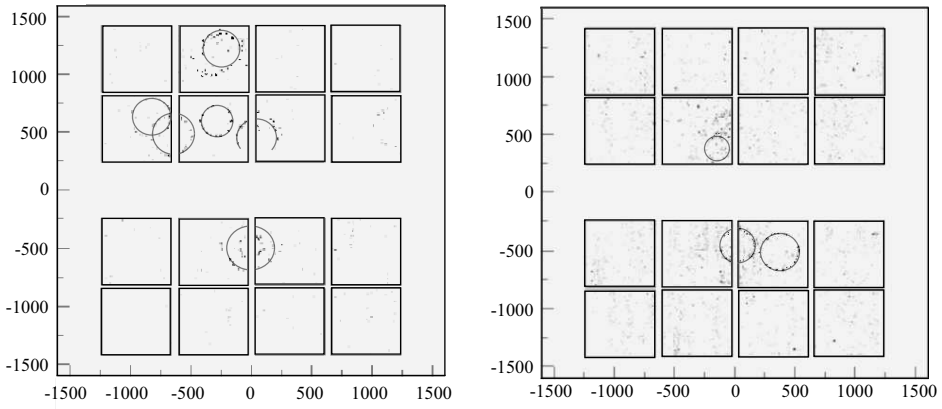

Figure 8.13: Left side : On line Event Display: 2002-run, Run 20319, Event Nr. 142, photon detector voltage: 2050 V, readout threshold: 3 sigma above background, low beam intensity, fraction of C_4F_{10} in the vessel: 93%. Right side : On line Event Display: 2002-run, Run 22312, Event Nr. 389, photon detector voltages: 1950 V, readout threshold: 2 sigma above background, nominal beam intensity, fraction of C_4F_{10} in the vessel: 68%. Some rings are enhanced for a better view.

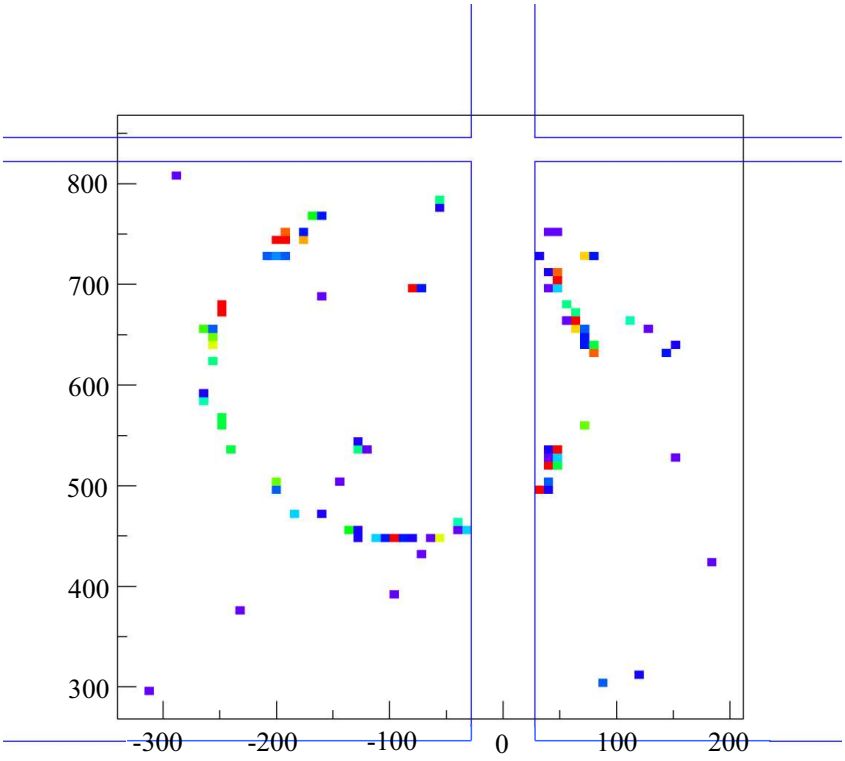

Figure 8.14: On line Event Display: 2002-run, zoomed view of one ring.

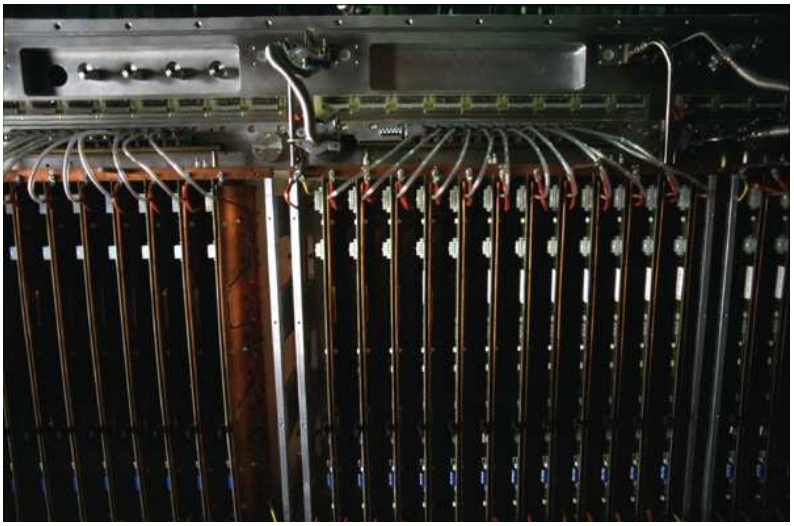

Figure 8.15: Photograph of a photon detector with the BORA front end boards connected via optical fibers. The copper cooling plates are connected to the cooling water supply.

8.3 The RICH-1 Radiator Gas System

The COMPASS RICH-1 gas system corresponds largely to the design of the RICH detector at HERA-B experiment at DESY and is made of similar components [70]. The main purpose of the gas system is to ensure the purity of the radiator gas by the use of a recirculation cycle and to transfer the gas out of and back into the storage-tank before and after a run. Because of the large, thin windows of the vessel the maximum overpressure allowed in the system is 5 mbar. For this reason there is a fully mechanical protection mechanism: A safety bubbler, assuring depressurization in a case of emergency when control mechanisms of the gas system may not work due to possible power-cuts. In case of overpressure gas is vented to atmosphere, in case of under pressure air is sucked into the vessel, resulting in a contamination of the radiator gas but protecting the delicate quartz windows of the photon detectors. The three main components are:

- The compressor rack, equipped with two oil-free compressors (Haug SOGX) together with a pneumatic valve, regulating the flow according to the measured pressure values.
- The purification rack, containing two pairs of two filter cartridges to keep the radiator gas clean, as water or oxygen traces are only tolerable in the ppm-range without influencing the radiator gas transparency.
- The third rack implies the gas-liquid separation unit, allowing to separate nitrogen and C_4F_{10} during filling or emptying of the vessel using their clearly different boiling points.

A 1000-liter stainless steel tank is used to store C_4F_{10} in liquid phase. The fill level is measured with an capacitive level indicator (Vega capacitive liquid level indicator) . The electrode, the medium and the cylinder around the electrode form an electrical capacitor. The capacitance is mainly influenced by three factors: The distance of the electrode plates, the size of the electrode plates and the kind of dielectric between the electrodes. Electrode and tube wall are the capacitor plates. The medium is the dielectric. Due to the higher dielectric constant (DK-value) of the medium against gas, the capacitance of the capacitor increases with raising covering of the electrode. The capacitance change is processed by the oscillator and converted into a level proportional value, which is provided analogue as standardized, floating 4 ... 20 mA-current signal. In addition a purely mechanical external liquid level indicator is attached to the storage tank. Figure 8.16 shows the single components.
The system is controlled and operated from a dedicated area outside the experimental area. With the help of a Schneider-PLC (Programmable Logic Control) one can choose between different operation modi, with the additional

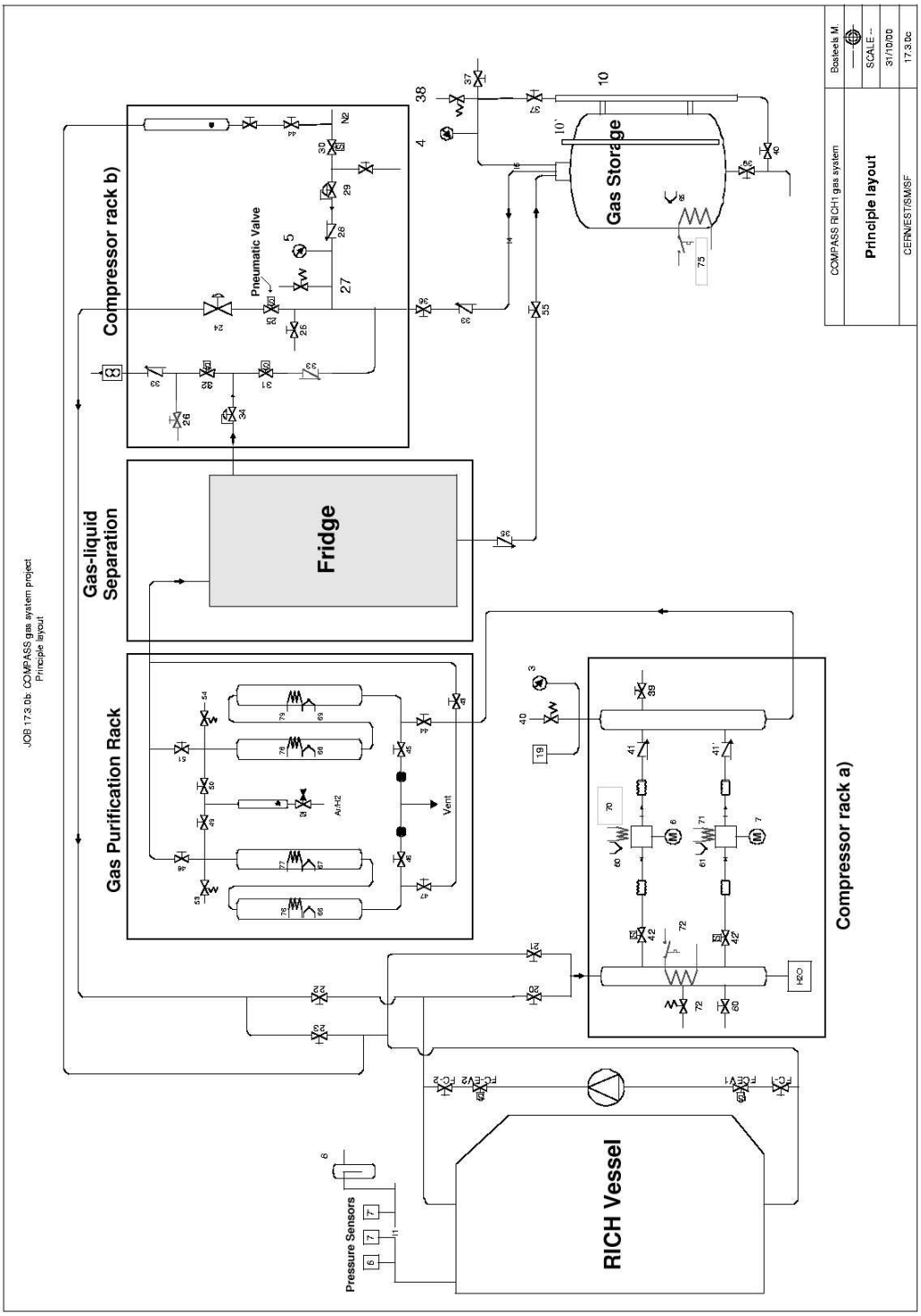

Figure 8.16: Schematic layout of the RICH-1 radiator gas system. The system consists of the compressor rack part a), part b) with the pneumatic valve for the pressure control, the purification rack and the gas-liquid separation unit.

possibility to readout several parameters via a PC connected to the system. Below all individual operation modes are described: Purge, Filling, Run and Recovery.

Purge-Mode:

In Purge Mode nitrogen from the CERN-supply system is flushed through the vessel while the purification system is bypassed. In this way it is guaranteed that the system is kept dry and clean.

Filling-Mode:

Starting with the vessel completely supplied with nitrogen, the volume is continuously filled with C_4F_{10} circulating the gas mixture through the gas-liquid separation unit, where C_4F_{10} and N_2 are separated due to their different boiling points. The nitrogen extracted from the vessel is vented to atmosphere. The fraction of C_4F_{10} is slowly increasing with the amount of radiator gas coming from the storage-tank. The filling is controlled with the help of two liquid-level indicator systems (installed at the storage-tank) and a gas-counter, summing up the vented amount of N_2. In addition, the gas coming from the RICH-vessel can be analyzed for the amount of C_4F_{10} using the sonar system (This system is described in detail in chapter 8.4.4). The operating temperature of the refrigerator is around -36° C at an absolute pressure of 6 bar. Looking at the PT-diagram (Figure 8.18) one finds a partial pressure for C_4F_{10} of 200 mbar. As the extracted amount of nitrogen during the gas-liquid separation process is vented to atmosphere, this fraction of C_4F_{10} still included is lost. Assuming a large reservoir and the continuation of the filling for a very long time, the filling could be completed at close to 100%. *In practice* a complete filling for a ration of 95:5 takes roughly 36 hours.

Run-Mode:

The radiator gas is circulated permanently through the purification-unit and the vessel. Pressure sensors on top of the vessel regulate the flow by means of variable opening and closing of a pneumatic valve in the compressor-rack. The allowed over pressure in the system is kept constant within small limits ($\pm$ 5 mbar). In order to conceive a homogeneous distribution inside the vessel the fast-circulation system is normally switched on during run mode.

Recovery-Mode:

With the gas-liquid separation unit turned on, the gas removed from the vessel is liquefied, C_4F_{10} goes back into the storage-tank, while an corresponding amount of nitrogen is introduced into the vessel in order to keep the system

pressure constant. The control of the procedure is similar to the one described for the Filling-Mode. Following the explanation as given for the Filling-Mode and considering the operating pressure, a loss of $\sim 3\%$ (200 mbar over 6 bar) of gas for each recovery is inevitable.

For permanent or intermittent control of the gas quality several analyzers are used and will be described in detail later: An Oxygen-analyzer (Alpha & Omega Trace Oxygen Analyzer 3000 and a Teledyne Trace Oxygen Analyzer), two moisture-meters (Shaw and Xentaur), a binary gas analyzer (Teledyne TC235) which allows to determine the fraction of C_4F_{10} in nitrogen, a setup for an integral absorption measurement of the radiator gas and since the year 2003 an on line monochromator system, which allows a wavelength-dependent determination of the transparency in the interesting region. Thereby it is ensured that the gas quality is controlled all the time and one is able to interact in case of present impurities. During "Filling" and "Recovery" mode a sonar device is used in addition, giving fast answer to the question of C_4F_{10} to N_2-ratio in the radiator gas using the fact the the sound velocity depends on the gas composition. Analyzing Cherenkov rings, the question if the expected number of Cherenkov-photons produced is the same everywhere inside the vessel, is essential. Besides assuming a constant efficiency of the photon-detectors all across the detection area, a homogeneous distribution of the radiator gas inside the vessel is presumed. The fast circulation system that was installed in 2002 ensures a uniform distribution of the gas by means of a temperature stabilized circulation at a maximum flow rate of 50 m^3/h.

The top and bottom in- and outlets of the vessel are comparably small, the pair of compressors allow a maximum flow of 10 m^3/h. The high density of the gas seems to suggest a 'top-bottom'-distribution. In addition Monte-Carlo-simulations show a strong temperature-dependence of the spatial distribution of the gas inside the vessel. As a result, one can claim, that both the foreseen external thermalization and the already operating fast circulation system lead to a sufficiently homogeneous distribution of the radiator gas inside the vessel.

The following sections outline the characteristics of the radiator gas, describe the purification procedures and the measuring setups for the determination of the transparency.

8.3.1 The Radiator Gas - C_4F_{10}

C_4F_{10}[3] , a heavy fluorocarbon, is used as radiator gas to produce Cherenkov-photons. Table 8.10 gives an overview of some important characteristics. Figures 8.17 and 8.18 show the dispersion and the pressure-temperature dependence of the material. The gas features low chromatic dispersion, it is non-flammable and non-toxic, which eases the handling. The total amount of C_4F_{10} used for the 2001-Run was delivered in 20 bottles, 65 kg of liquid each (=5.5 m^3 gas per bottle) beginning of the year 2000. For the following years the gas was delivered in large bottles of 550 kg content. For the determination of the purity of the gas and to set up the cleaning procedures to be applied, each bottle was checked using the reflectometer setup.

Formula	C_4F_{10} or CF_3-CF_2-CF_2-CF_3	
Indication	Perfluorobutane, also Decafluorobutane, non flammable, non toxic	
Molecular weight	238.028	g/mol
Boiling point (1 bar)	-2.0	° C
Freezing point	-128.0	° C
Density (15°C, 1,9 bar)	1534.0	kg/m^3 (liquid)
	20.16	kg/m^3 (Gas)
Refractive index n	1.00153	(7 eV)
DK-value	$\sim$ 1.75	
Thermo conductivity	52.6	mW/m K (25° C; liquid)
	12.1	mW/m K (25° C; Gas)
Threshold momentum	2.5	GeV/c (pions)
	8.9	GeV/c (kanons)
	17.0	GeV/c (protons)
Optical properties	low chromatic dispersion: dn/dE [eV^{-1}] = 53×10^{-6} (at 177 nm)	
	good intrinsic transparency in the UV up to 160 nm photon-wavelength	

Table 8.10: Physical properties of C_4F_{10}.

Figure 8.19 shows variations of the refractive index during 2003 data taking. To make a precise data analysis possible, a permanent monitoring of the refractive index is necessary. During the 2003 run the monochromator system was used on a regular basis to control the gas quality.

[3] 3M-Company

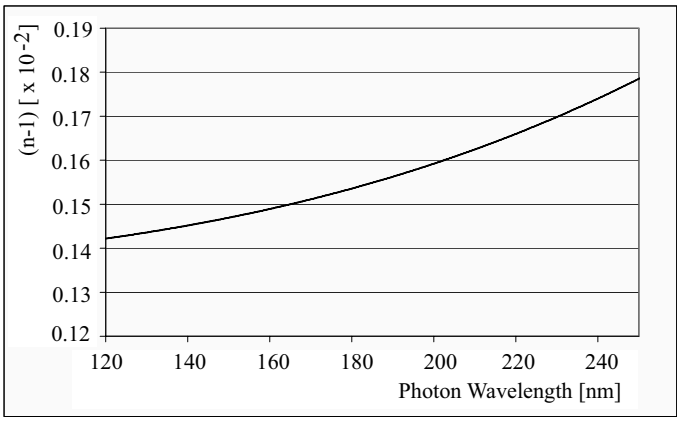

Figure 8.17: The dispersion of the radiator gas is shown. The refractive index (n-1) of the radiator gas is plotted as a function of the photon wavelength. The plot is extracted from [71].

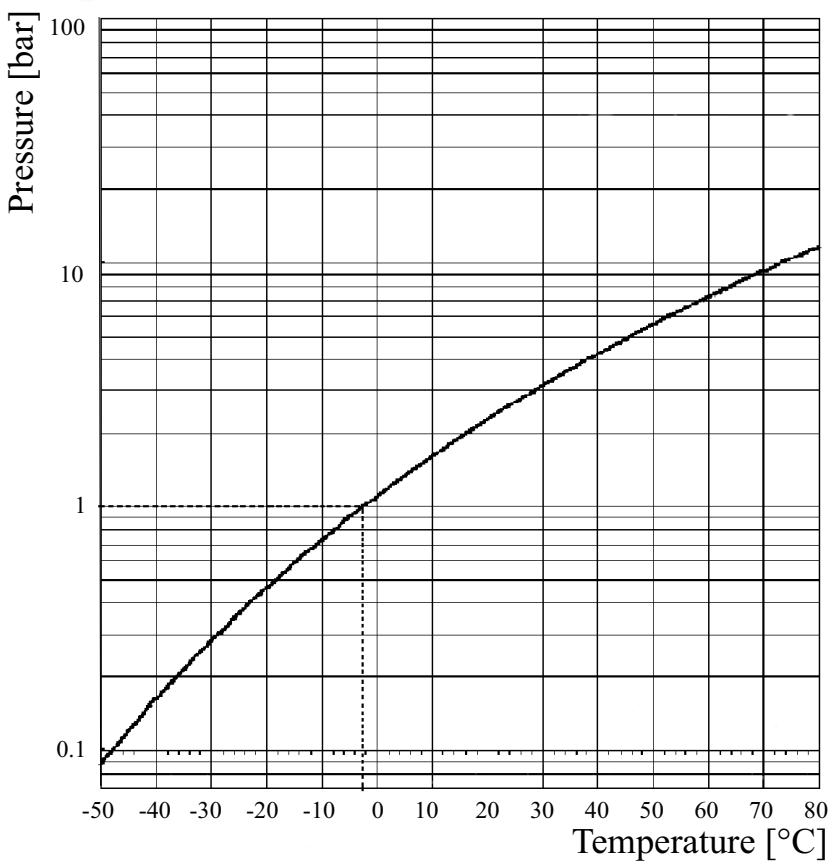

Figure 8.18: Pressure-Temperature diagram for C_4F_{10}. The boiling point is indicated at -2 ° for a pressure of 1 bar.

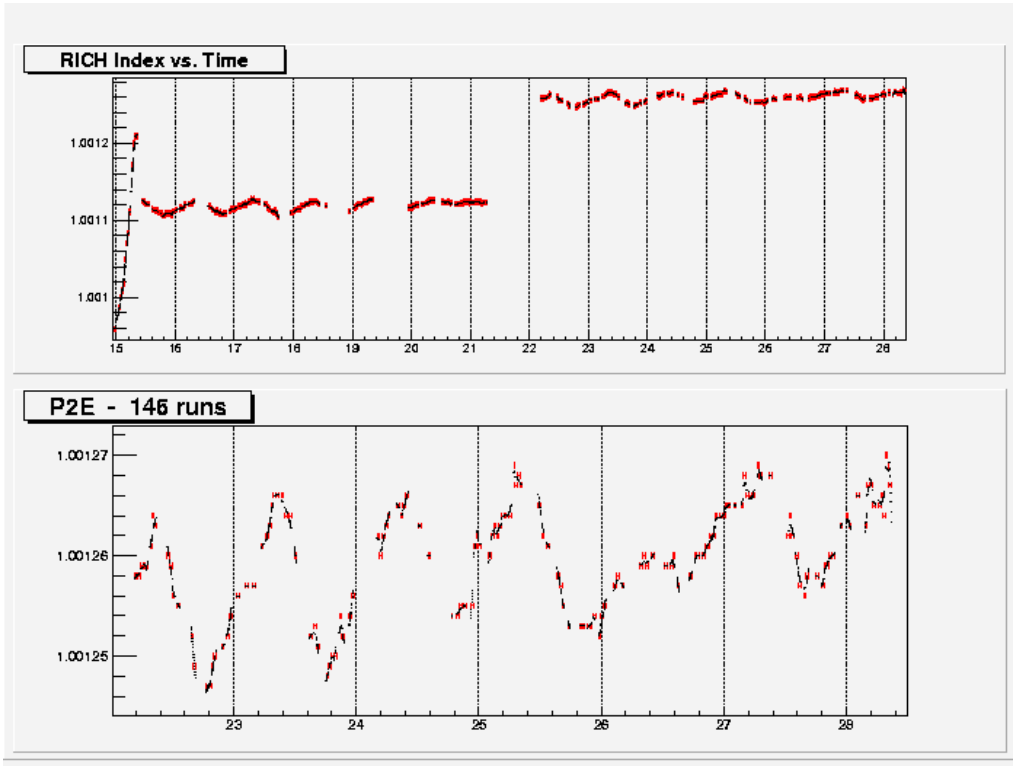

Figure 8.19: Variations of the refractive index of C_4F_{10} during the 2003 data taking. The upper plot shows a jump in the refractive index after an additional filling. The lower plot demonstrates day/night temperature fluctuations.

8.3.2 Gas Purification

The main contaminations, reducing the transparency of the radiator gas and therefore also the number of transmitted Cherenkov-photons are water and oxygen impurities. In the wavelength range from 160 nm to 180 nm UV-light is almost completely absorbed by oxygen and water impurities. In the following, the filter systems used are described together with the applied quality control mechanisms.

For first testing, silica gel, activated carbon, molecular sieve 13X and copper-filters were used. After several tests it was decided to use the copper-filter (BASF R3-11G) [72] . Here, the following reaction comes into operation for the oxygen-removal:

$$2\ \mathrm{Cu} \ + \ \mathrm{O_2} \rightarrow 2\ \mathrm{CuO} \qquad \Delta \mathrm{H} = \text{-}155.3\ \mathrm{kJ}$$

Optimization of the radiator gas purification was an evolving process, going through several development stages. For the first 110 m^3 it emerged from the reflectometer measurement that there were batches with two qualities in the delivery: nine bottles showed an initial transparency of 95% at 230 nm and could be cleaned up to 65% at 165 nm with a loss in material of $\sim 7\%$. Eleven bottles showed an initial transparency of $< 70\%$ at 230 nm where the pre-cleaning procedure, circulating the material through a set of filters in liquid phase, required several weeks with a loss of material close to 50%, giving finally 80% transparency at 200 nm wavelength. At that stage an additional cleaning step was tested - the Cryo-Cleaning. This procedure uses the fact, that C_4F_{10}, after cool down to -40°C with liquid nitrogen, is liquid at normal pressure while oxygen is still in gas phase at that temperature. This oxygen can be removed with a flushing gas like argon. using this procedure the oxygen content could be reduced by a factor of 10 to 40. Figures 8.20 and 8.21 show the transparency-plots for both batches where values for the raw-material and the final-state are plotted. Therein the increase in transparency after several weeks of filtering of these batches is shown.

The cleaning setup contains two sectors: the pre-cleaning , performed mostly in a dedicated laboratory with direct measuring potentiality (vacuum ultraviolet reflectometer; VUV) respectively cryo-cleaning and on line cleaning in the experimental area using the purification unit installed in the radiator gas system. The pre-cleaning setup that was used for the preparation of the gas for the 2001-run (see Figure 8.22 consists of a magnetic gear pump and a support for up to five filter cartridges in parallel. The bottle to be cleaned is mounted on a scale, making it easy to control the amount of material circulating.

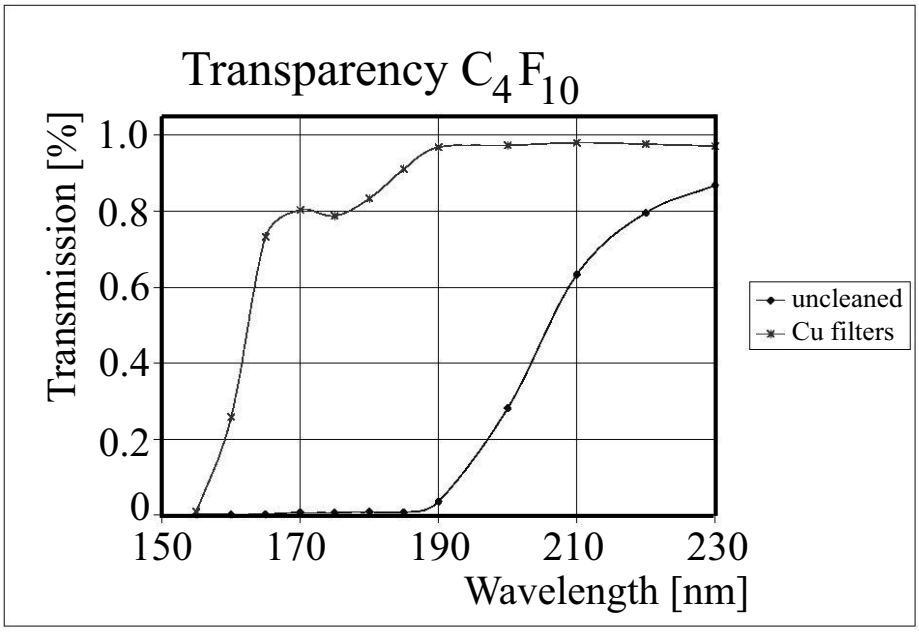

Figure 8.20: Sample of "good" radiator gas out of the 2000 delivery. The measurement is performed in liquid phase. Only the initial and final curves are shown.

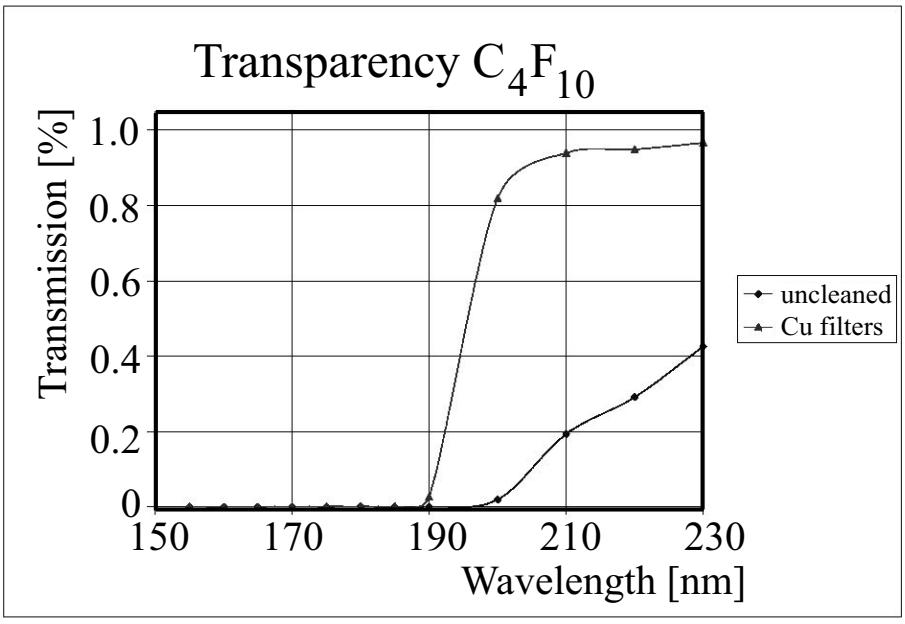

Figure 8.21: Sample of "bad" radiator gas out of the 2000 delivery. The measurement is performed in liquid phase. Only the initial and final curves are shown.

Figure 8.22: Pre-cleaning Setup 2001. The system consists of a special mount for a bottle and a rack with the filter cartridges, a magnetic gear pump (bottom) and a distribution panel with flow meters (top).

A VUV-reflectometer, located directly next to the pre-cleaning setup, allows the measurement of the transparency in gas- or liquid phase. Due to a comparable fast saturation of the copper-filled cartridges used, a change of the filter material on a two-day basis was necessary. During ongoing service two sets of five cartridges were used, making it possible to have always one set active while the second one was regenerated. The regeneration procedure consists of flushing with argon for 12 hours at 200°C followed by flushing with Noxal (Ar/H_2 mixture 97/3%) for 8 hours at 200°C and terminating flushing with argon for 12 hours at room temperature. This procedure turned out to be quite time consuming and manpower intensive, resulting in the search for a different approach.

For the 2002 and 2003 run, the additional radiator gas needed was pre-cleaned using the refurbished DELPHI pre-cleaning system, where the raw material is filtered in gas phase (see Figure 8.25). This system consists of a set of interchangeable filters of molecular sieves of 5 $\dot{A}$, 13X molecular sieves and activated carbon, a pump for circulation and a cooling unit for gas-liquid separation. The gas is circulated in a closed-loop or transferred from the initial bottle with the uncleaned gas into a second bottle for storage of clean gas. The process is controlled via a PLC-unit, including water and oxygen analyzers. At this stage the regeneration of the cartridges was still done manually. The overall losses were still in the order of 20%, while to amount of time needed was significantly less. Figure 8.23 and 8.24 demonstrate the increase in transparency during the cleaning-procedure.

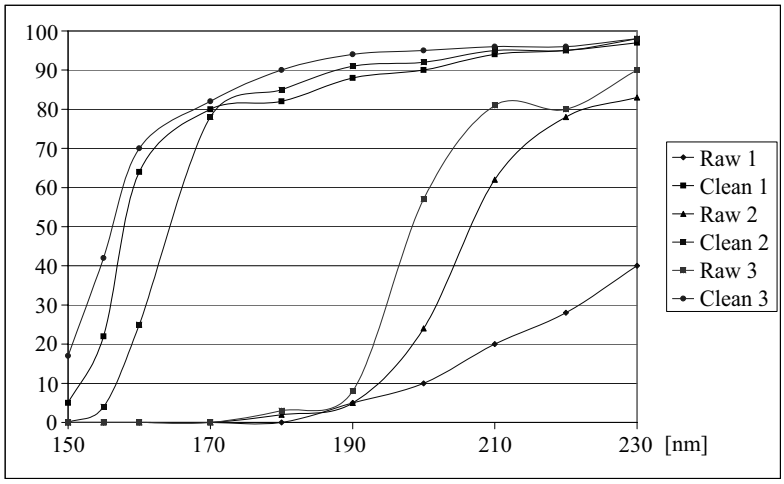

Figure 8.23: Pre-cleaning of C_4F_{10} for the 2002 run. Three different qualities of raw material are shown together with the final transparency after pre-cleaning. In all cases the design value of 80% at 165 nm wavelength was reached.

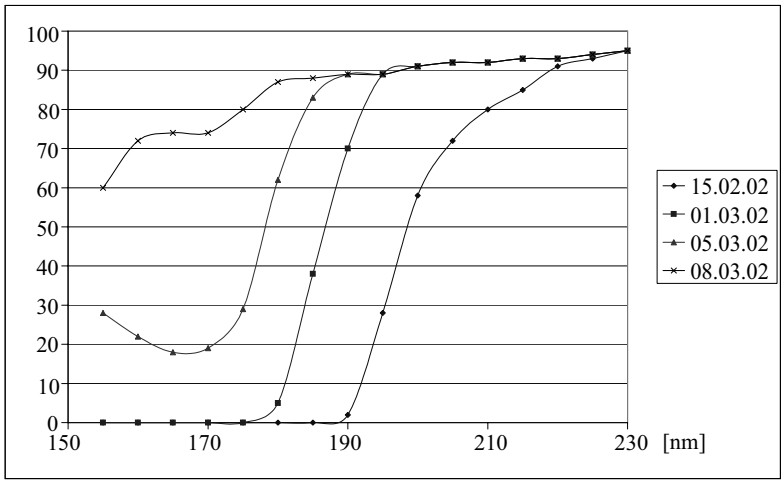

Figure 8.24: Pre-cleaning of the additional C_4F_{10} for the 2002 run. Starting with the raw material showing no transparency below 190 nm, a final value of 75% at 165 nm wavelength was reached for the total amount of material after 3.5 weeks of pre-cleaning.

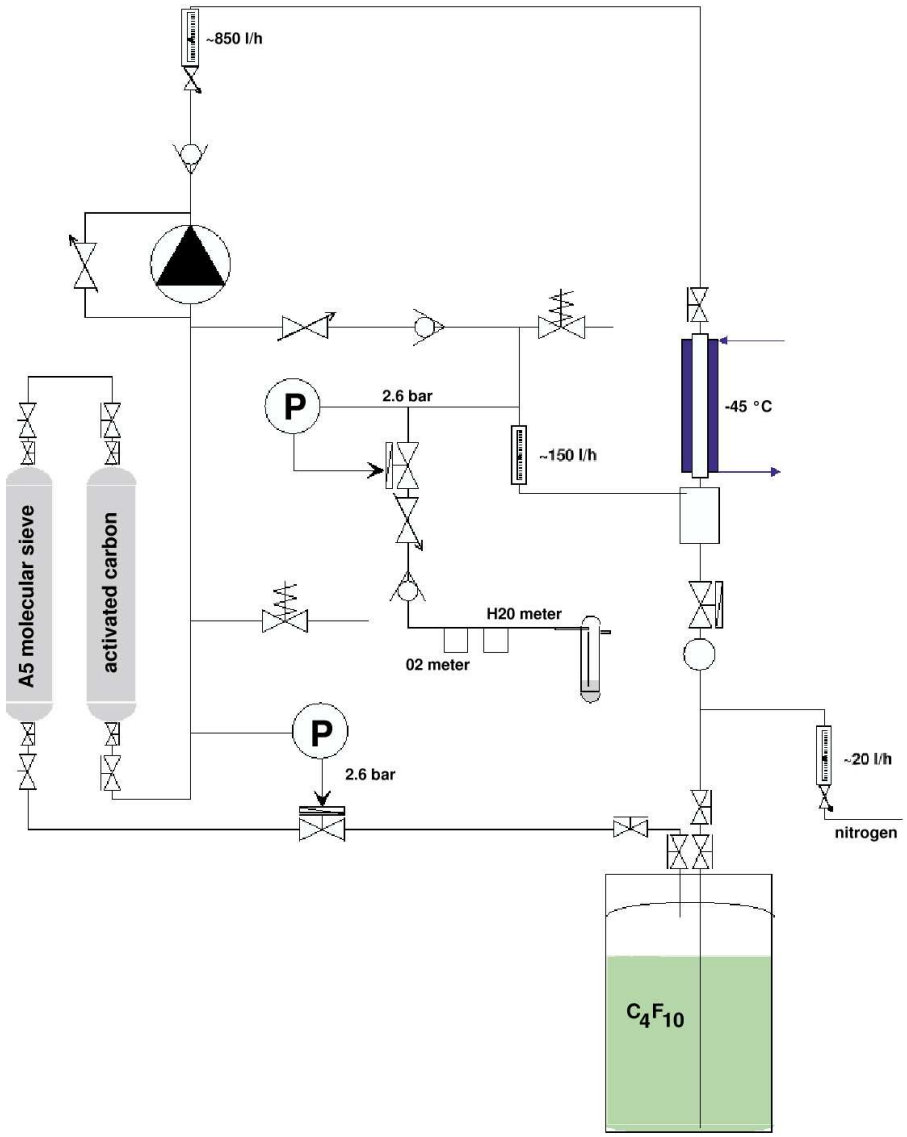

Figure 8.25: Schematic drawing of the pre-cleaning system, used for the 2002 and 2003 run.

For both runs the design transparency of 80% at 165 nm was achieved and kept rather stable during a long period of data taking. During the 2002-run leakages, that turned out to be not curable during the run caused non negligible losses together with a small drop in transparency, as Figure 8.26 shows. More precisely one had to note down a loss of C_4F_{10} of 1.3% per day.

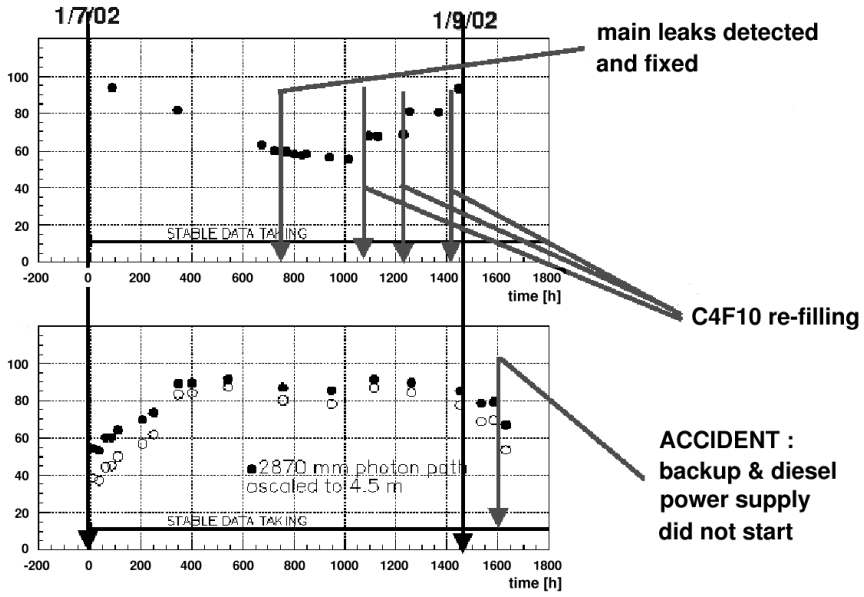

Figure 8.26: C_4F_{10}-fraction and -transparency during 2002 run. The upper plot shows the fraction of C_4F_{10} inside the vessel. The lower plot shows the transmission of the radiator gas. The open circles show the values obtained with the integral transmission measurement system (chapter 8.3.5), the full circles show the values scaled to 4.5 m photon path length.

For finding of the leaks a detailed investigation started after the run, including a leak test of the huge windows closing the vessel. A rather large leak was found in the upper part of the huge flange connecting the downstream window and the vessel. Minor leakages also could be fixed in the radiator gas system itself, resulting in a significantly lower leak rate after the first weeks of running in the 2003-run. Monitoring the level of liquid C_4F_{10} inside the storage-tank one can calculate the actual loss rate. Compared to the 2002 run the loss rate went down to $\approx$ 90 l per day, which is a factor of 5 lower. A plot showing the measured leak rate (Figure 8.7) can be found in chapter 8.2.1. Detailed information about VUV absorbing vapors in per fluorocarbons can be found in [73].

The prepared cleaning system for the 2004 run is similar to the previous setup but has a double set of cartridges (two times four cartridges) that can be regenerated *on line*, to have a close to automated system, as the manpower to operate a system like that is one of the most important expense and availability factors.

8.3.3 The modified Reflectometer

For transparency measurements of the radiator gas in the beginning of the pre-cleaning phase the modified CERN-EP VUV reflectometer was used. The setup is shown in Figure 8.27.

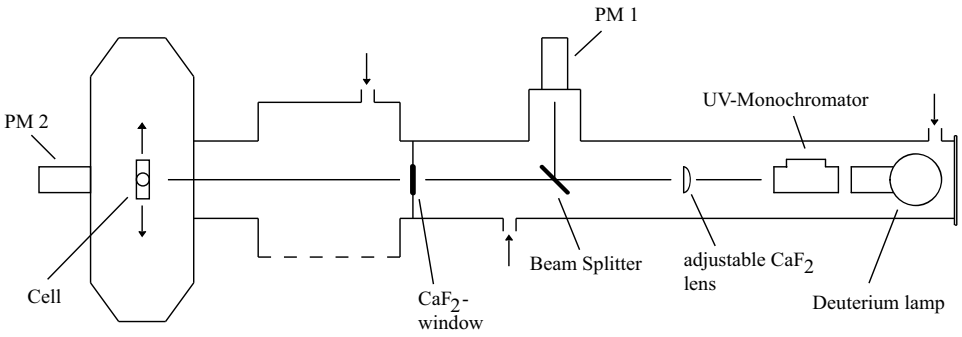

Figure 8.27: Schematic view of the CERN-EP VUV Reflectometer (modified).

With the help of an UV-monochromator the wavelength of the light emitted by the deuterium lamp is selected. All measurements are performed in the wavelength region between 160 and 230 nm. Uniform focusing of the beam is achieved with an adjustable calcium-florid lens. A beam splitter allows to perform reference measurements, by redirecting part of the beam to a photomultiplier (PM1) installed perpendicular to to the beam-direction. The measuring cell is mounted on a gear rod in the part separated from the vacuum-chamber by a calcium-florid window. The photomultiplier PM2 - measuring the intensity of light crossing the measuring cell is attached there. The movable measuring cell allows for three different measurements: The background is quantified by directing the beam toward a metallic plate, the reference measurement is performed with pass in vacuum and the actual measurement, where the beam is guided through the measuring cell, filled with C_4F_{10} or with nitrogen for calibration purposes. The signal is registered with PM2. The reflectivity R is given by the following expression:

$$R = I_{trans}/I_{in}\,; \quad \begin{aligned} I_{trans} &= \text{Intensity of light transmitted} \\ I_{in} &= \text{Intensity of incoming light} \end{aligned}$$

The measuring cell is connected to the pre-cleaning setup (see chapter 8.3.2) via stainless steel pipes, allowing fast and efficient measurements during the cleaning process. Especially in the initial phase of the pre-cleaning this was extremely time saving, when different filter materials were tested.

8.3.4 The On-line Monochromator

Using a direct connection to the fast circulation system (see chapter 8.3) a small quantity of gas can be extracted from the circuit to be analyzed in a monochromator setup . Figure 8.28 sketches the setup. Monochromatic light (Figure 8.29 shows the inner part of the monochromator) enters a horizontal tube where a beam splitter sends part of the light to a photomultiplier PM2 and part through a vertical tube, filled with the sample gas, to photomultiplier PM1. Using these signals, the fraction of absorbed light is determined, giving the transparency of the sample gas in dependence of wavelength in the range from 150 nm to 230 nm.

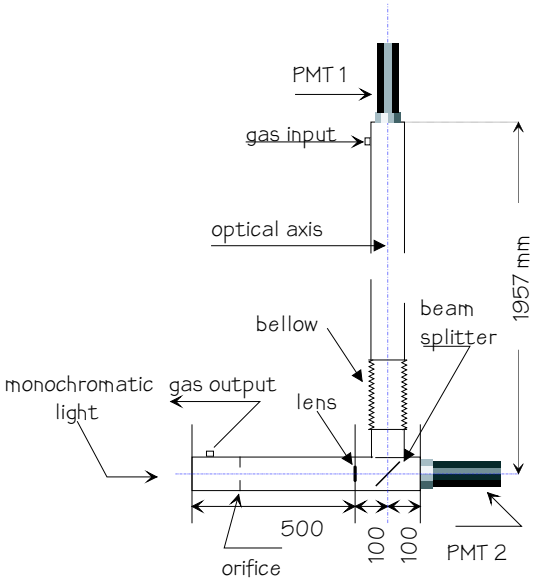

Figure 8.28: Monochromator setup for on line transparency measurements. Dimensions are given in mm.

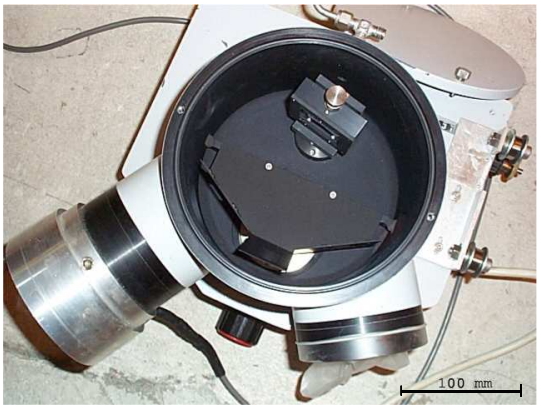

Figure 8.29: Top view photograph into the monochromator.

8.3.5 The Integral Transmission Measurement System

For 'on location' measurements of the radiator gas transparency a custom made setup for integral VUV-absorption measurements was installed directly connected to the RICH-1 gas system. Figure 8.30 shows the setup.

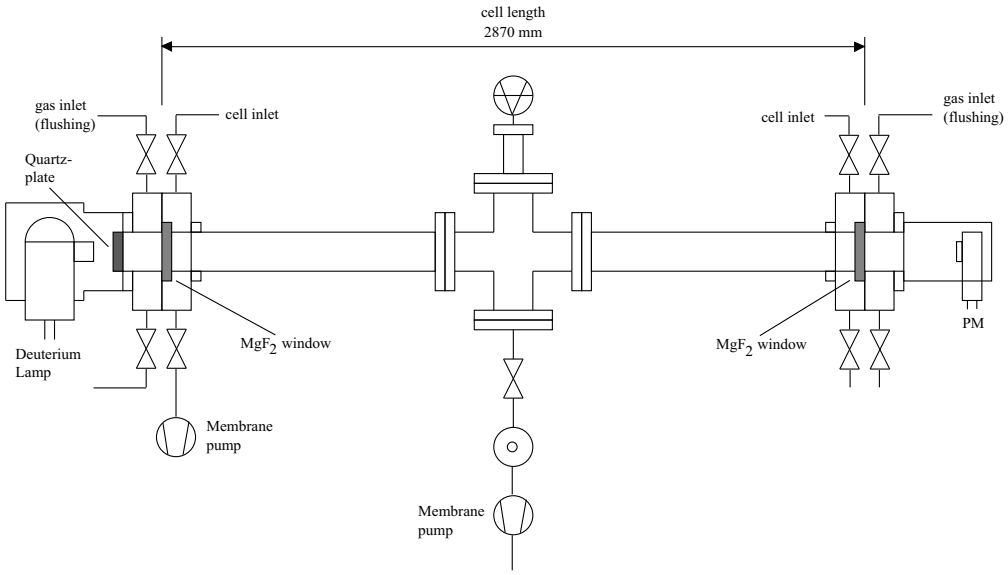

Figure 8.30: Schematical Drawing, integral transmission measurement system.

The measuring chamber is located between the deuterium lamp and the photomultiplier - separated by magnesium fluoride windows. A Hamamatsu series L2-2000 device is used as lamp (specifications see Table 8.12) with a spectral response between 160 nm and 400 nm. Inside the connecting flange between deuterium lamp and measuring tube a quartz plate (thickness: 5 mm; characteristics as given in Figure 8.32 UV-cutoff energy: 7.7 eV; $\lambda \simeq 161$ nm) is implemented, to perform the measurements similar to the ones inside the RICH-1 vessel. The measuring tube is machined of stainless steel, showing a total length of 2870 mm and can be evacuated down to $< 10^{-5}$ mbar with a two-stage pump system (a membrane fore pump and a turbo-molecular pump). As photomultiplier a Hamamatsu model R7639 (see Table 8.13), sensitive in the wavelength region between 115 nm up to 230 nm with a quantum efficiency of 40% at 155 nm is used. Both the lamp and the photomultiplier are housed in chambers which are flushed with clean nitrogen to keep them transparent. Table 8.11 illustrates a typical measurement. After calibration with evacuated tube and control with pure nitrogen as reference gas, the transparency of the radiator gas can be easily determined out of the fraction of absorbed light using the relation

$$I_{abs} = \frac{I_{vac} - I_{gas}}{I_{vac}}$$

PM signal [mV]	cell pressure [mbar]	absorption [%]	transmission [%]
−18.2	$< 10^{-4}$		
−17.5	1000 (N_2)	3.8 %	96.2 %
−18.0	$< 10^{-4}$		
−11.3	1000 (C_4F_{10})	37.0 %	63.0 %
−17.6	$< 10^{-4}$		
−17.1	1000 (N_2)	2.8 %	97.2 %

Table 8.11: Example of an integral absorption measurement. For control purposes before and after the radiator gas measurement clean nitrogen is measured. The total measuring error is below 2%.

Type	L2D2-2000, Type L7296
Window material	synthetic silica
Spectral response	160 to 400 nm
Aperture	0.5 mm
Starting voltage	400 V
Anode current	300 mA
Signal stability	$\pm$0.3 %
Guaranteed lifetime	2000 hours

Table 8.12: Excerpt of data sheet of the Hamamatsu L2D2-Deuterium Lamp.

During the construction phase of the system a dedicated test setup was used to measure the spectral response of the system (see Figure 8.32). A McPherson model 218 monochromator was used together with a deuterium lamp and a photomultiplier (both Hamamatsu) to perform the measurement in the wavelength interval from 150 to 220 nm with a resolution of 0.5 nm. The expected influence of the quartz window in the setup was taken into account.

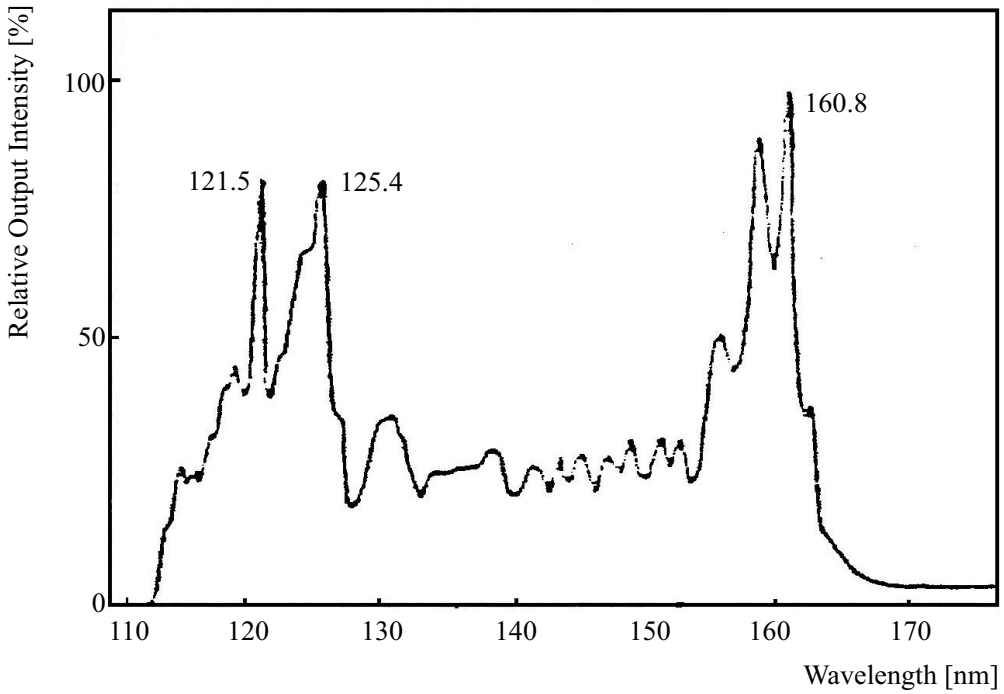

Figure 8.31: Spectral Emission of the Deuterium lamp with an MgF_2 window.

Type	R 7639
Spectral response	115 to 230 *nm*
Maximum signal wavelength	155 nm
Photo cathode material	diamond
Photo cathode surface	3×12 *mm*
Window material	MgF_2
Dynode	Sb-Cs
Number of Dynode stages	9
Quantum efficiency	40% at 155 nm
Amplification	3.0×10^6
Dark current	max. 5 nA
Anode current stability	0.1 %

Table 8.13: Excerpt of data sheet of the Hamamatsu R 7639 Photomultiplier.

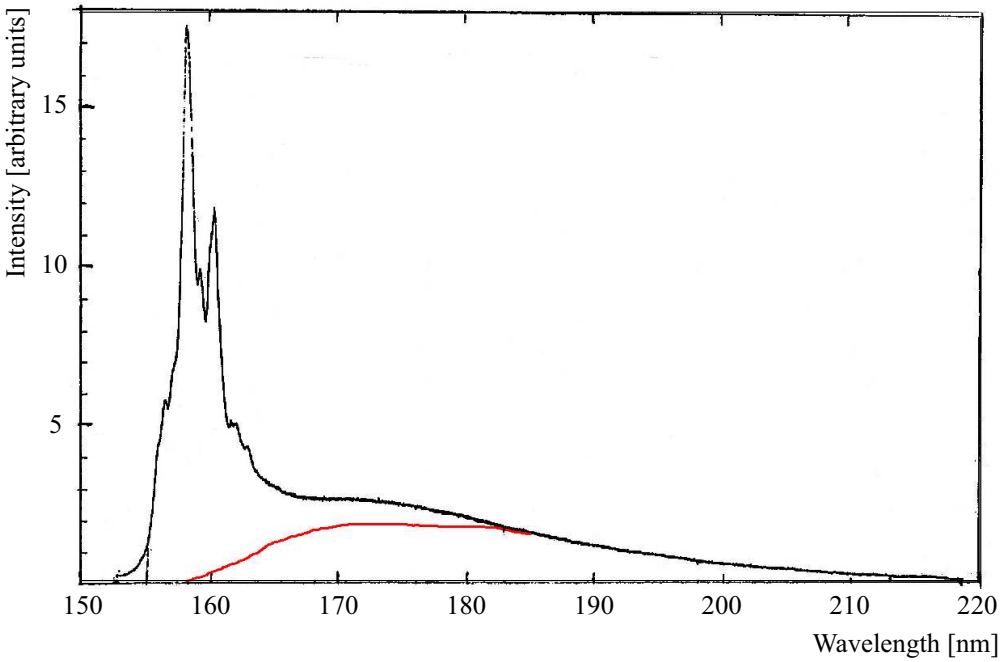

Figure 8.32: Measured relative spectral response of the VUV Transmission System. The expected spectrum with the quartz plate in place is indicated in red (flat curve in bottom part of the plot).

8.4 Monitoring Issues

For a permanent control of the radiator gas quality a variety of monitoring devices is used. The oxygen and water contamination, together with the composition of the gas are observed using the following devices.

8.4.1 Alpha & Omega^{TM} Oxygen Analyzer

The series 3000 oxygen analyzer is a trace oxygen sensor , being composed of a lead-oxygen battery, which is equipped with a lead anode, a gold-coated cathode and potassium-hydroxyd electrolyte. The common feature for all electrolytic transducers is the fact that they are built of three components: cathode, anode and an electrolyte. In the present case of the Alpha & Omega sensor the cathode forms the transducer - the place of chemical reduction of oxygen. Below one finds the chemical reactions in detail:

$$\text{cathodic reaction} \quad 4e^- + O_2 + 2H_2O \rightarrow 4OH^-$$

Four electrons combine with an oxygen molecule to end up with four hydroxyd ions. In parallel the following anodic reaction occurs:

$$\text{anodic reaction} \quad 2Pb + 2OH^- \rightarrow PbO + H_2O + 2e^-$$

the anode (lead) is oxidized to lead-oxide, releasing two electrons per lead-atom. Together one gets the complete reaction:

$$O_2 + 2Pb \rightarrow 2PbO$$

Thus, the sensor reacts very sensitive to oxygen, assuming that there are no other components in the gas-flow being able to oxide lead. Possible candidates could be halogens (iod, bromine, chlorine and fluorine). In the cathodic part of the reaction four electrons are transferred per each reacting oxygen molecule. Therefore, the oxygen molecule must diffuse through the sensor membrane as well as through the thin electrolyte film which is located between sensor membrane and up side of the cathode. The rate of oxygen molecules reaching the surface is proportional to the oxygen concentration in the gas mixture, determining the electrical signal.

8.4.2 Humidity Sensors

One model used is a Shaw^{TM} SHA which offers the possibility to measure the dew point temperature and features analog or digital display in ppm. The sensor is made of an ultra pure aluminum wire, coated with a hygroscopic and porous gold-layer. The gold-film and the aluminum-core build a capacitance. The capacity and its variation are read out at a bias frequency of 50 or 60 Hz. Some of the water molecules inside the volume around the sensor enter the dielectric gold-layer, where the molecular movement of the molecules is lowered and the molecules condensate to liquid water. Because of the high dielectric constant of water in the order of 80, the dielectric value varies quite a lot and is measured by the analyzer. In-between the water vapor outside the sensor and the condensed water inside the pores a dynamic stable equilibrium is adjusted. Molecules being larger than water-vapor can not enter the pores, so the sensor is resistant against many impurities independent from the carrier gas. Using the same operating principle the second sensor is a Xentaur loop powered dew point sensor. It uses a high capacitance aluminum oxide thin film which ensures high precision measurements in the range from -100°C up to +20°C dew point temperature. The amount of humidity in the gas stream can be measured in units of ppm. The resolution is around 0.1 °C.

8.4.3 Teledyne Binary Gas Analyzer

The Model 235 Thermal Conductivity Analyzer is being used. This device measures the concentration of one component in a binary stream of gas or the purity of a sample stream containing a composite mixture of impurities by comparing the difference in thermal conductivity of the sample stream with that of a reference gas of fixed composition. The difference in thermal conductivity between the fixed reference gas and the sample is measured by hot wire elements. The elements are mounted in a cell assembly so that one set is in the reference and the other in the sample stream. Each set of elements is a component in an electrical bridge circuit.

During calibration a constant supply of gas of a fixed composition is needed as reference to which the sample gas will be compared. The reference gas is selected to represent the main background of the analysis. To zero-standardize the analyzer a gas containing little or none of the components of interest is required. After the zero setting has been finished, the sensitivity of the analyzer has to be adjusted by sending the span gas through the analyzer and setting the correct value of the known impurity in the span.

Points along the range of interest will produce a DC electrical signal representative of the analysis. This signal is feed to an amplifier and span potentiometer, which produces a standard 0-1 V output signal. The temperature of the measuring cell is regulated within 0.1 °C by a dedicated control circuit. A thermisor is used to measure the temperature and a zero-crossing switch regulates the power in a cartridge type heater.

8.4.4 Sonar

In series with the gas flow through the monochromator described in the previous section there is a sonar to measure the composition of the radiator gas. Looking at a binary gas mixture the sound velocity depends on the according speed of the single components and their relative concentration. The experimental setup is simple: An evacuated stainless steel tube with sender and receiver of sound waves fixed at opposite sides and simple readout electronics. Below, the measuring principle and the setup used (Figure 8.33) are described: the theory for the speed of sound in an ideal gas for small amplitudes results in a pressure independent equation [74]:

$$v = \left(\frac{\gamma RT}{M}\right)^{1/2}, \tag{8.15}$$

with $\gamma = C_P/C_V$ and molecular mass M. Temperature differences may influence the precision of the measurements, as to be seen in Eq. 8.16.

$$v_1^2/v_2^2 = T_1^2/T_2^2, \tag{8.16}$$

with v_1 and v_2 as the velocities at the temperatures T_1 and T_2. At a temperate T_1 (K) a change in temperature $\Delta T = (T_2\text{-}T_1)$ results in a change of speed of sound $\Delta\ v = (v_2\text{-}v_1)$ according to

$$\Delta T = T_1(1 - v_1^2/v_2^2)(v_1^2/v_2^2)^{-1}. \tag{8.17}$$

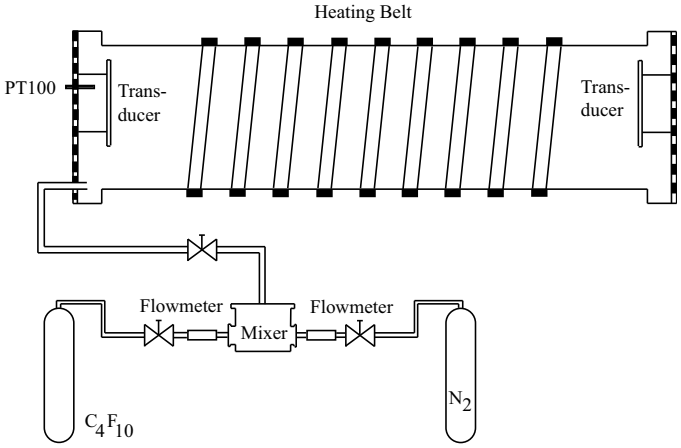

Figure 8.33: Schematic design of the sonar system.

Possible temperature changes have to be taken into account during series of measurements. A stainless steel tube of 1297 mm length is used as measuring section. The heart of the system is a Polaroid 6500 Transducer [75], originally used in auto focus systems of cameras. In the setup described here it fulfills two duties: It acts

as an electrostatic loudspeaker. After a start-signal the driver module generates a series of 16 pulses with a frequency of 49 kHz and an amplitude of 400 V. Followed by a dead time of 2.3 ms the transducer switches to reception mode and operates like a microphone (typical bias voltage 200 V). During this phase the amplification value increases in twelve steps in order to compensate the attenuation of the signal in the gas mixture. The stop signal is generated when the preset threshold voltage is reached. A 16-bit counter is counting the number of pulses of the internal clock (4.77 MHz respectively 210 ns) between start and stop. The sound velocity of the probed gas is given as:

$$v_{meas} = \frac{2L}{t_{meas} - t_{offset}} \tag{8.18}$$

with L as path length, t_{meas} as measured time of flight and an offset t_{offset} which is caused by a short delay between the start-signal and the emission of the first pulse. It can be easily measured with the help of gases with well known velocity of sound. In the setup used, one finds $t_{offset} = 0.056$ ms. Figure 8.34 shows calibration curves for measured speed of sound for different fractions of C_4F_{10} in $C_4F_{10} - N_2$-mixtures. For the 2004 run an additional sonar system will be installed at the top of the RICH vessel measuring directly inside the radiator volume.

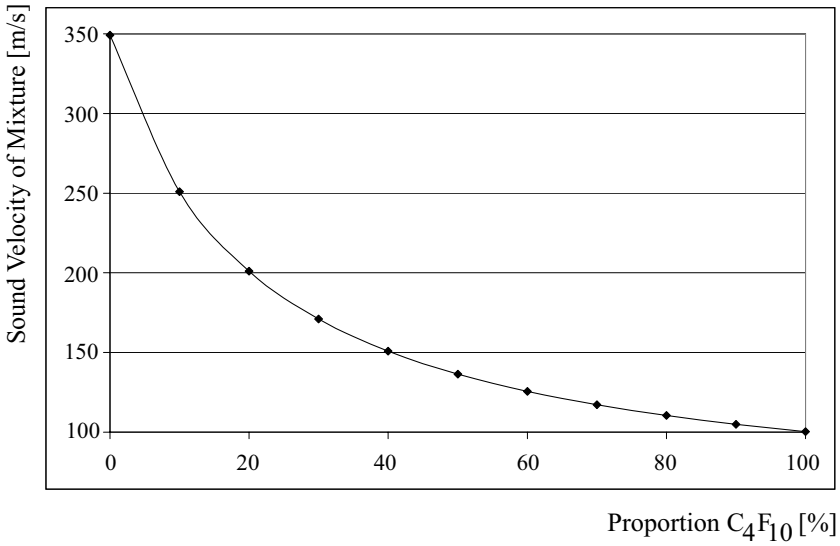

Figure 8.34: Calibration curve: measured speed of sound versus C_4F_{10}-fraction.

9 Data Taking with Muon Beam in 2001, 2002 and 2003

The beam times in 2001 and 2002 were the first tests under real conditions after the comissioning in the year 2000. The main focus will be put here on the RICH-1 performance. The RICH-1 detector showed a reasonable good performance, without concealing that there were several problems and backstrokes. During the 2003 data taking, the system has performed much more stable. In this chapter the different aspects of hardware (photon detectors, radiator gas and radiator gas system) and software (pattern recognition, data analysis) performance are discussed.

Figures 9.1, 9.2 and 9.3 show the setup of the spectrometer during 2001, 2002 and 2003 data taking.

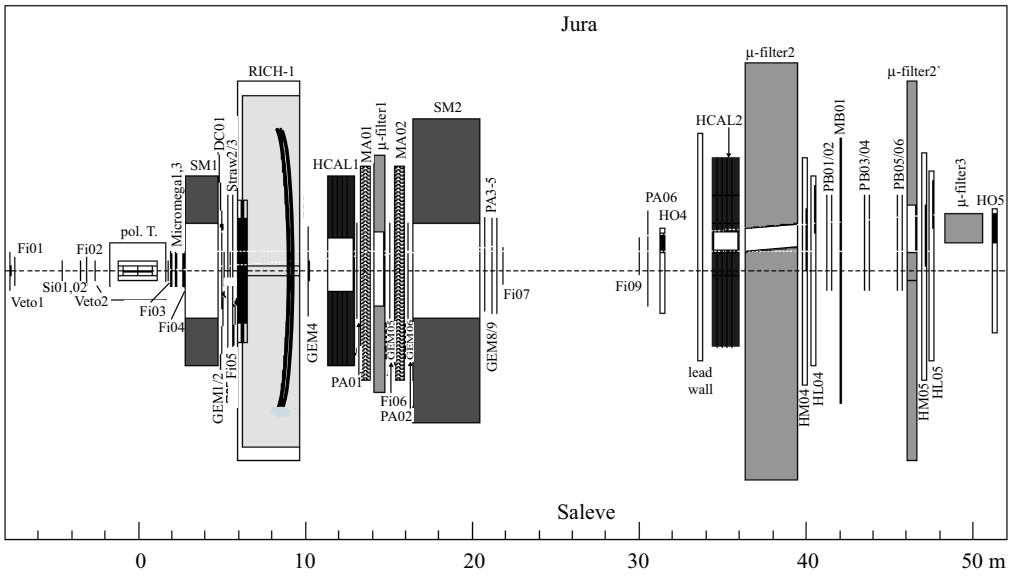

Figure 9.1: COMPASS spectrometer during the 2001-data taking.

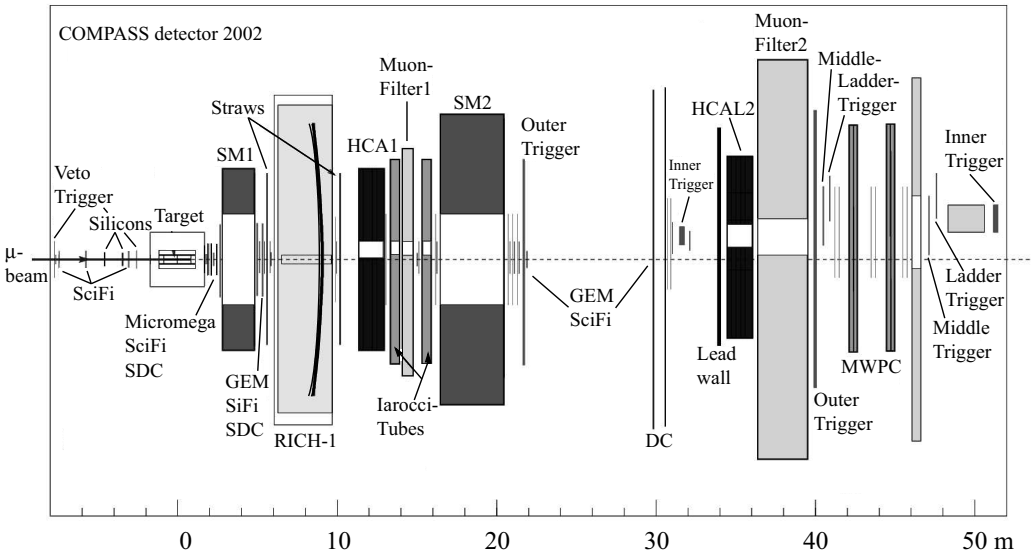

Figure 9.2: COMPASS spectrometer during the 2002-data taking. Downstream RICH-1 an additional straw detector was installed and two drift chambers upstream the second hadron calorimeter.

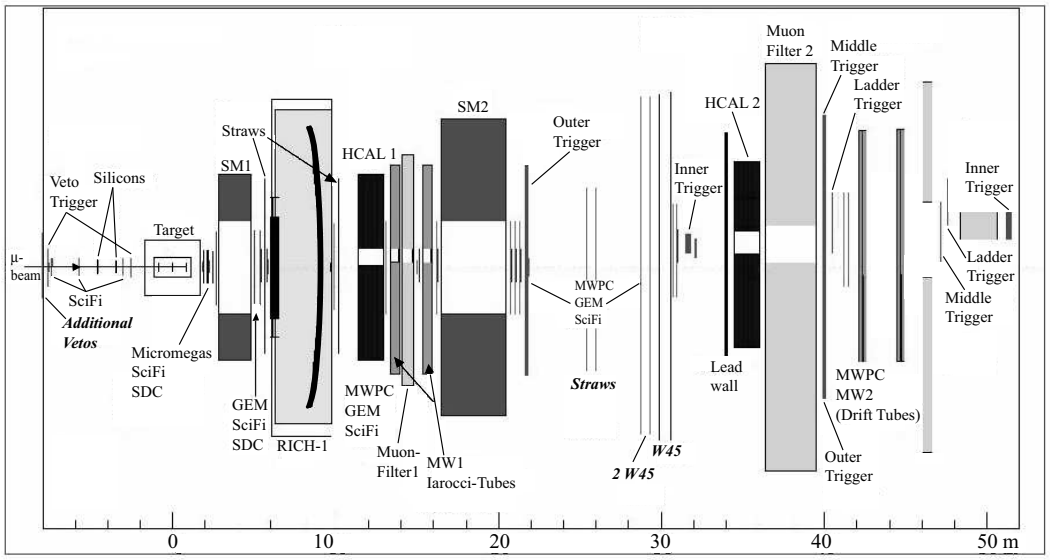

Figure 9.3: COMPASS spectrometer during the 2003-data taking. Note the additional veto system in front of the target, the additional straw layers and two additional W45 layer downstream SM2.

9.1 RICH-1 Photon Detector Performance

Tab. 9.1 shows operational voltages that could be sustained during the 2002 and 2003 data taking with the corresponding detector efficiencies.

	2002		2003	
photon detector	voltage $[V]$	efficiency [%]	voltage $[V]$	efficiency [%]
PD 0	1920	**60**	1950(*)	66
PD 1	1980	72	2000	76
PD 2	1980	72	1980	72
PD 3	2000	76	2000	76
PD 4	1890	**54**	2000	76
PD 5	2000	76	2030	82
PD 6	1850	**45**	2050	83
PD 7	1990	73	2000	76

Table 9.1: RICH-1 photon detector high voltages and efficiencies during the 2002- and 2003 run. (*) three groups out of nine for PD0 behaved unstable and were taken out of the readout.

During the operation, electrical instabilities were discovered at high beam rates, leading to a reduced operational voltage (100-150 V lower than the 2100 V nominal high voltage) for six chambers. Three chambers had to operate at significantly lower efficiencies. In order to cure this problem, a detailed investigation was started. Finally, local wire defects could be found, which made a refurbishment of four wire planes and the exchange of two wire planes necessary. During the winter shutdown in 2002 PD 6 was in the state of reconstruction and testing together with PD 0 and PD 4 in the CERN Gamma Irradiation Facility (GIF) [76], where the chambers can be operated under realistic conditions in terms of beam intensity and particle flux. For the 2003 run both the upper and lower photon-detector array could be equipped with fully operational chambers, where best-performing chambers were installed in the central region.

9.2 New Hardware for the 2002 run

A cooling system, using water circulation, for the front-end boards stabilized the temperature of the photon detector frames to T=22°± 1°. The total heating power of the 192 boards is in the order of ≈ 3.2 kW with no activity and ≈ 4.7 kW in data-taking conditions. Therefore they form a large source of local heating of the vessel structure causing temperature gradients inside.

Better grounding between the front-end boards and the photo-cathode frames resulted in a reduced noise-level of 1100 e^- compared to 2100 e^- in the year 2001 (see Figure 9.4).

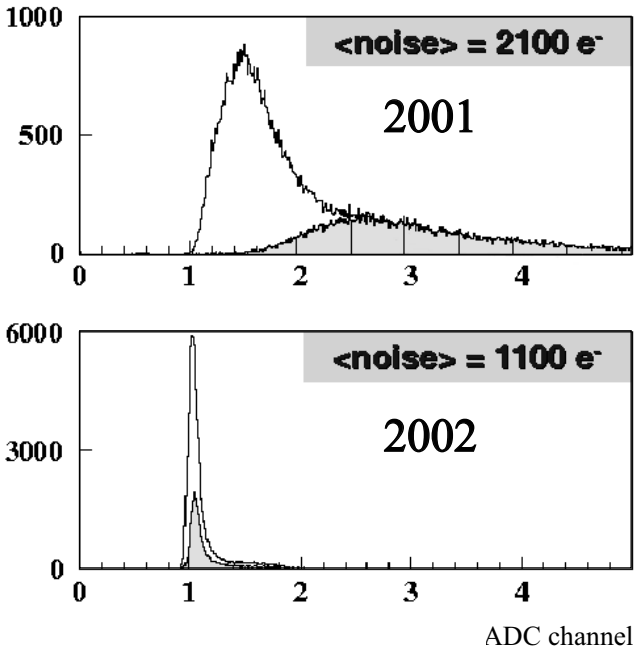

Figure 9.4: Electronic noise of the front-end boards. Comparison 2001 and 2002. The open curve shows a photon detector signal, the grey area represents the noise distribution, counted in electrons.

To attain the maximum homogeneity of the radiator gas inside the vessel a 'fast circulation system' was installed before the 2002 run, thermalizing the gas (Δ T < 0.2°C) and circulating it through the system at a flow rate of $\sim$ 50 m^3/h. The effect of temperature difference is quite severe, if one considers the contribution to Δn

$$\Delta T = 1.0°C \quad \rightarrow \quad \frac{\Delta n}{n-1} = \pm 0.2\%. \tag{9.1}$$

9.3 New hardware for the 2003 run

For a fast and convenient gas quality check a monochromator system (see section 8.3.4) together with a sonar device (see section 8.4.4) were installed directly at the gas system in the experimental area. A pair of additional small diameter transfer lines with pickup points at the fast circulation in- and outlet connections allow a small permanent gas flow for analysis due to the pressure difference between the two lines. Tab. 9.2 gives some important parameters using gas viscosities in the range of 30 - 40 mPa s.

turbo speed	flow [l/h]	p_{low} [mbar]	p_{high} [mbar]	ΔP [mbar]
50 %	18	-3.30	+2.25	5.55
55 %	28	-4.60	+2.70	7.30

Table 9.2: Flow rates and pressures for the online gas analysis. The pressure difference Δ P between the pickup point at the vessel and the input at the monochromator system has to be adjusted to guarantee stable measuring conditions.

Using these two monitoring devices a regular check of transparency and composition of the radiator gas is possible, guaranteeing fastest possible interaction in case of saturation of the filters.
For further pre-cleaning of additional raw material a new system was constructed. It uses - as in the past - two sets of copper-filters and molecular sieves which can be regenerated online without any manual intervention. The fridge circuit is operated with liquid nitrogen, as described in detail in section 8.3.2.

9.4 Pressure, Temperature and the Refractive Index

Starting with the Clausius-Mossotti relation [77]

$$\gamma_{mol} = \frac{3}{4\pi N}\frac{\epsilon - 1}{\epsilon + 2}, \tag{9.2}$$

with N as the number of gas molecules per unit volume, ϵ as the dielectric constant and γ_{mol} being the molecular polarizability the refractive index $n = \sqrt{\epsilon}$ can be related to the gas density

$$n - 1 \propto N\gamma_{mol}. \tag{9.3}$$

Taking pressure and temperature the Cherenkov angle can be evaluated

$$\Theta^2 \approx 4\pi\frac{P}{kT}\gamma_{mol}. \tag{9.4}$$

Using pressure and temperature data from the RICH vessel the following correction can be applied:

$$\Theta_{corr} = \Theta_{meas}\sqrt{\frac{P_{meas}}{1013mbar}\frac{T_0}{T_{meas}}}. \tag{9.5}$$

Besides several sensors all over the experimental area, a network of temperature sensors (PT 100 elements) inside the vessel measures at different representative positions: two times eight sensors cover the upstream window region and the whole surface of the downstream window. Figure 9.5 shows the positions of the various sensors inside the vessel.
The pressure inside the vessel is measured by two independent pressure sensors responsible for the regulation of the gas flow through the system. In addition temperature-, pressure- and humidity sensors outside the experimental area record changing weather conditions. As the refractive index of the radiator gas depends on external pressure variations, the pressure values are archived for later corrections. One sees changes in the order of about 10 Torr (see Figure 9.6) within a few days. Looking at the temperature trends in Figure 9.7 and 9.8 one sees how the temperature inside the vessel follows the outside temperature. Fast changes in temperature are well damped. Maxima are shifted by roughly six hours, with the same frequency of 24 hours. This behavior can be explained by the slow heat transfer from the outside environment into the vessel. Temperature fluctuations are less visible during periods when the fast circulation system is running. For the selected period the average temperature differences between top and bottom sensors are in the order of about 0,8 °C (see Figure 9.7) with the fast circulation running while temperature differences for the selected period with the fast circulation system being switched

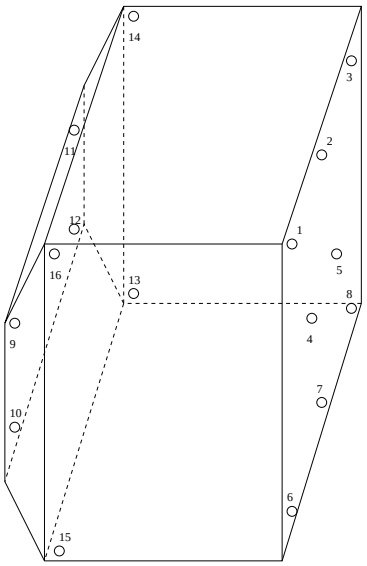

Figure 9.5: Positions of the 16 temperature sensors inside the RICH vessel.

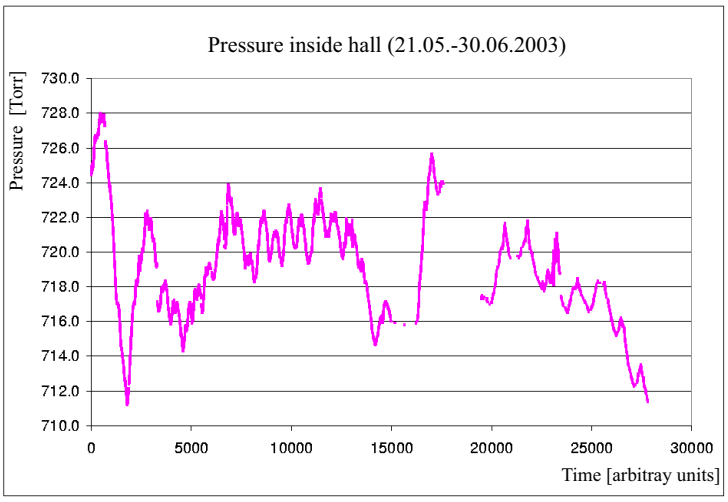

Figure 9.6: Atmospheric pressure inside the experimental area during the period 21.05.03 - 30.06.03

off is in the order of about 1,5 °C (Figure 9.8). Assuming a higher circulation speed of gas inside the vessel for the first case, a more uniform temperature distribution is expected.

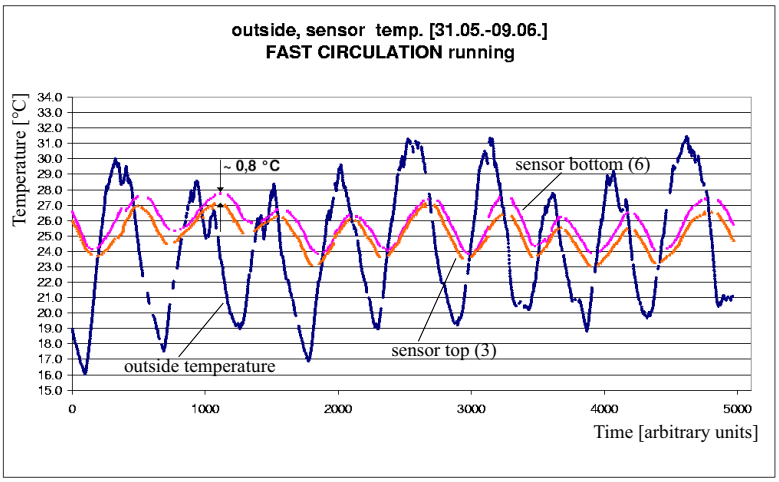

Figure 9.7: Outside temperature and temperatures inside the vessel for the period of 31.05.03 till 09.06.03 with the fast circulation system running at *nominal* speed. Respectively one sensor located at the top and bottom of the downstream window are taken as an example.

This presumption seems to be proven by looking at a period where the Fast Circulation system was running at reduced speed (see Figure 9.11). One finds a temperature difference of about 1,0 °C. Looking at Eq. 9.1 this variation causes changes in (n-1) in the order of 0.2%.
Figure 9.9 and 9.10 show the temperature distribution inside the vessel when the fast circulation system was running at nominal speed. There is no clear difference visible between the upstream and downstream set of sensors. Figure 9.11 and 9.12 illustrate the temperature distribution inside the vessel when the Fast Circulation system was running at a reduced speed. As expected the temperature trends indicate a slightly higher temperature inhomogeneity compared to periods with the Fast Circulation system running at nominal speed. Differences between the upstream- and downstream window temperature can be explained on the basis of the heat supply caused by the photon detectors and are in the order of two degrees.

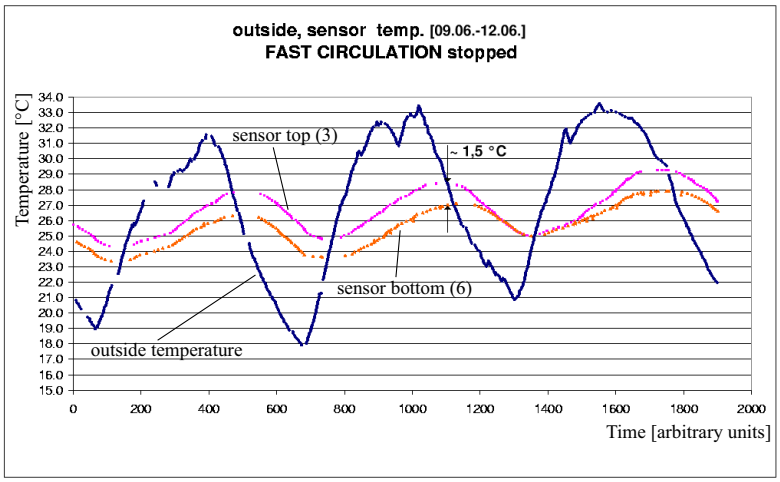

Figure 9.8: Outside temperature and temperatures inside the vessel for the period of 09.06.03 till 12.06.03 with the fast circulation system being *stopped*. Compared to Figure 9.7 a factor twice as high in the 'top-bottom temperature distribution' is visible.

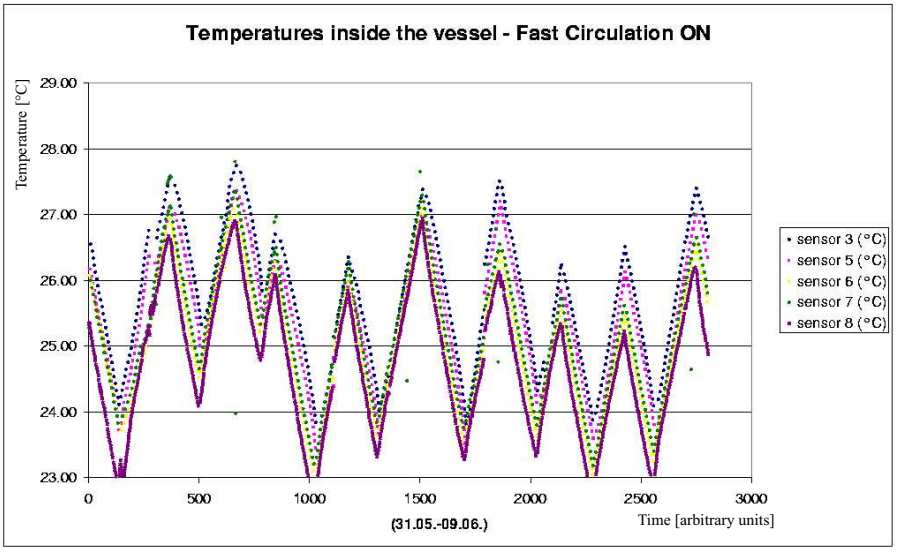

Figure 9.9: Temperature distribution of sensors located at the downstream window for a period of ten days. The Fast Circulation system was running at *nominal* speed.

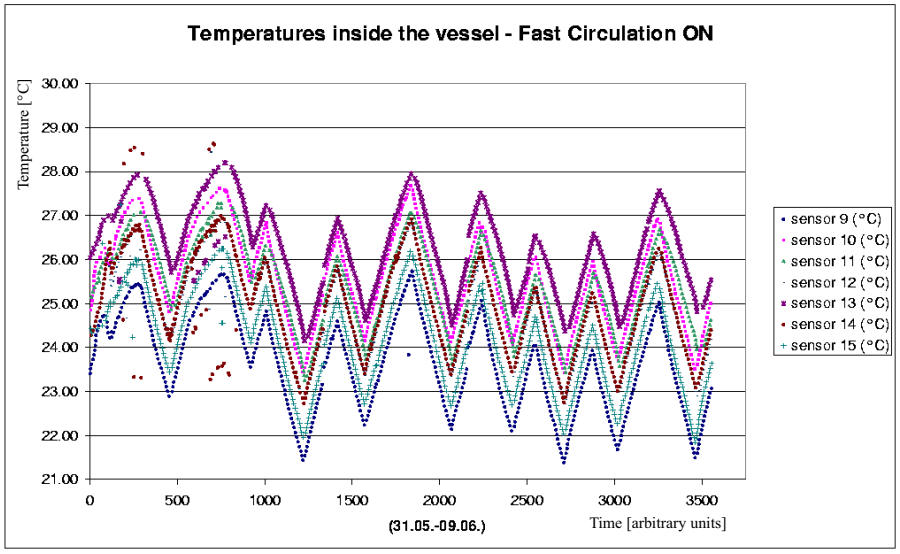

Figure 9.10: Temperature distribution of sensors located at the upstream window for a period of ten days. The Fast Circulation system was running at *nominal* speed.

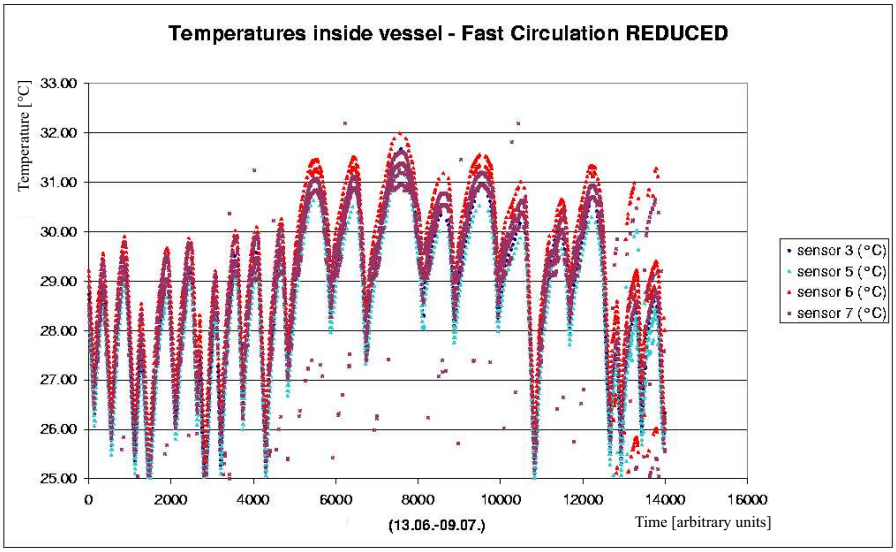

Figure 9.11: Temperature distribution of sensors located at the downstream window for a period of 26 days. The Fast Circulation system was running at a *reduced* speed.

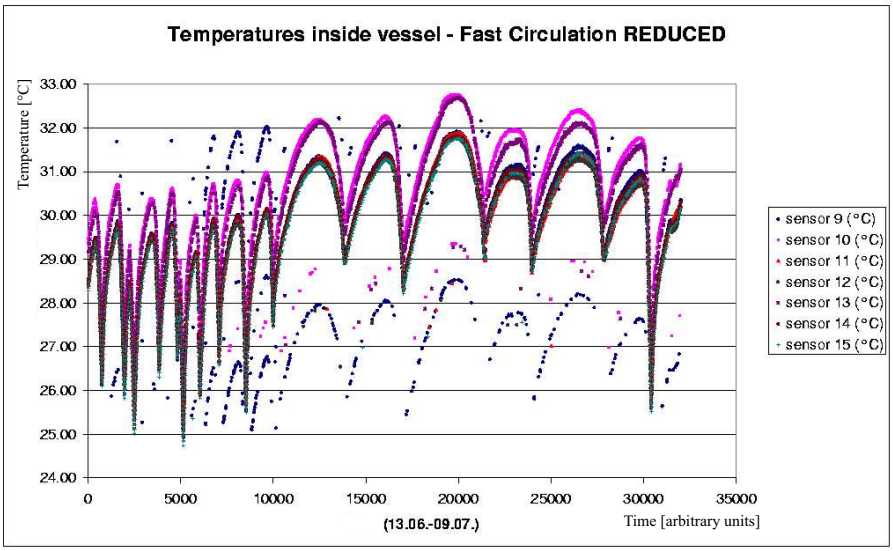

Figure 9.12: Temperature distribution of sensors located at the upstream window for a period of 26 days. The Fast Circulation system was running at a *reduced* speed.

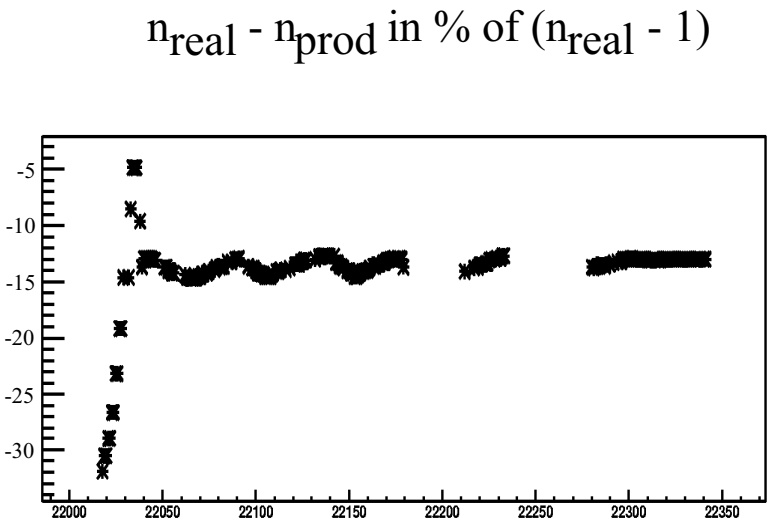

Figure 9.13: The average error on the refractive index (n-1) during the P2D production period is around 13 %.

Figure 9.13 shows the difference of the real refractive index minus the refractive index used for production in percent of $(n_{real} - 1)$, where real means that a corrected value after *post*production was used. Here, values were corrected on a run-by-run basis using the calculated number coming from the RICH-analysis. For the P2D period the deviation is in the order of 13 ± 1 %.

Concluding one can say that a thermalization of the RICH - using a tent-like encasing structure - together with a permanent control of the refractive index is absolutely needed in order to achieve the needed stability for the refractive index during a full beam time.

10 Data Analysis

In the following chapter some insight into the data analysis with special interest of the involvement of the RICH-1 is provided. Ring recognition and clustering as well as basic principles of Likelihood analysis and particle identification based on χ^2 analysis are explained. The search for D mesons and their main decay products, kaons and pions, provides access to $\Delta G/G$, first results on this are presented in section 10.4.

The pattern recognition and particle identification code RICHONE [78] is used for the RICH-1 data analysis. The Cherenkov reconstruction mechanism is described in [59]. The method assumes that the particle trajectory, specially the particle momentum, is known upstream of the RICH detector. First data reduction is done by clustering, to be followed by pattern recognition and particle identification, based on *Likelihood selection* or χ^2*-calculations*.

10.1 Ring Recognition and Clustering

The following reference systems are used in the reconstruction procedure:

- Main Reference System (MRS). The origin is in the nominal center of the interaction target. Looking downstream the z-axis is parallel to the beam, the y-axis vertical upwards and the x-axis horizontal to the left.
- Detector Reference Systems (DRS). They are defined for the upper and lower detector surfaces, with the origin at the center of each detector and the x-axis parallel to the x-axis of the MRS. Each detector surface is tilted by an angle of 150 mrad with respect to the MRS xy-plane.

The input to the pattern recognition procedure comes from the RICH photon chambers, from tracking detectors, and from Monte Carlo data generation. In this order, the pulse hight from the ADC of each detector pad with its signal and its address, for each reconstructed particle its position at the RICH entrance window, x_p, y_p, z_p, the direction tg_{xp}, tg_{yp} and the measured momentum p_p and Monte Carlo generated 'true' values for particle masses, photon impact points on the detector are used. The active pads around the photon impact points are distributed on the detector surface. Before this data can enter the reconstruction

procedure, the pads may be arranged together in groups - in clusters, which should better correspond to the real photon impact point. The basic principle is to take an average of the individual pad positions, weighted with the pad pulse height. The actual code works along the following line: the pad with maximum pulse height is taken and adjacent (along x or y only) active pads are inserted into the cluster up to the level, where their pulse hight is less than 0.3 along x or 0.6 along y of the maximum value. The cluster summation is stopped when no more adjacent pads are found and it is restarted for a further cluster looking for the next pulse height maximum.

For the reconstruction each cluster is assumed to correspond to a photon impact point on the detector plane (DRS). For each reconstructed particle it is presumed that all photons have been emitted from the middle point of its trajectory inside the radiator gas volume, which is computed from the measured particle parameters. For each cluster, the polar angles $\theta_{cluster}$ and $\phi_{cluster}$ around the particle trajectory are then evaluated. Looking at a $\phi_{cluster}$ vs $\theta_{cluster}$ plot, photons emitted by the selected particle string at constant $\theta_{cluster}$ and distribute uniformly in $\phi_{cluster}$, contrary to photons emitted by other particles, which spread along nonlinear paths. The *ring* pattern recognition is then equivalent to a search for a peak in the $\theta_{cluster}$ projection of the distribution described above. A $\theta_{cluster}$ bin size of 1 $mrad$ has been chosen, as a function of the expected counts in the signal peak. To determine the exact peak position, the counts are integrated within a window of 5 sampling channels (bins) and a scan is made over a range in $\theta_{cluster}$ from 0 to 70 mrad. The peak position is taken as the maximum in the scan.

The Figure of Merit is then computed as the ratio between integrated counts in the peak window and the background inside the peak, where the background is computed from the count average outside the peak. A first approximation of the value for θ_{ring} is computed as the average of the values for $\theta_{cluster}$ inside the peak. In this averaging, each value for $\theta_{cluster}$ is taken with equal weight. Because of the presence of the quartz entrance window (thickness 5 mm, refractive index 1.458) to the detector, incoming photons are distorted for incidence angles different from 90°. The knowledge of the approximate reflected photon trajectory after the first reconstruction step, allows the determination of the photon incidence angle and as a next step, the computation of the correction to the photon impact point on the cathode plane. Finally a second value for θ_{ring} is computed. The standard deviation σ_{θ}^{photon} of the $\theta_{cluster}$ - θ_{ring} distribution is taken as the inverse *single photon* resolution which is $\simeq$ 800 μrad. One standard method for categorical data analysis is the Likelihood analysis which is described in more detail in the following section.

10.2 Likelihood Analysis

Maximum Likelihood, also called the maximum Likelihood method, is the procedure of finding the value of one or more parameters for a given statistic which makes the known Likelihood distribution a maximum.

In the case of the COMPASS RICH 1 reconstruction a Likelihood function of the photons in the ring is built. Both the signal and the background have to be described correctly which is difficult in the case of COMPASS as the theoretical description is not straightforward, and the distributions can be taken from experimental or Monte Carlo data. The signal can be described in the $(\theta^{photon}, \Phi^{photon})$-plane [79] for fixed Φ^{photon} by a Gaussian distribution $\mathrm{G}(\theta^{photon}, \Phi^{photon})$ around θ^{ring} with a standard deviation $\sigma_{\theta}^{photon}(\Phi^{photon}, \beta)$. The background due to the electronics noise of the photon detectors can be described by a function $\mathrm{B}(\theta^{photon}, \Phi^{photon})$. Under the assumption of this background being almost uniformly distributed over the detector surface one can try to determine it from real data. For each particle mass hypothesis the probability density can be written as:

$$L_N = \prod_{k=1}^{N^{photon}} \Big[(1-\epsilon)\, G\,(\theta^{photon}, \Phi^{photon}) + \epsilon\, B(\theta^{photon}) \Big], \tag{10.1}$$

with

$$\begin{aligned} G(\theta^{photon}, \Phi^{photon}) &= \frac{1}{\sigma_{\theta}^{photon}\sqrt{2\pi}}\, \frac{\theta^{photon}}{\Theta^{mass}}\, exp\Big[-\frac{1}{2} \frac{(\theta^{photon} - \Theta^{mass})^2}{(\sigma_{\Theta}^{photon})^2} \Big] \\ B(\theta^{photon}) &= \frac{2}{(\Theta_M)^2}\, \theta^{photon} \\ \epsilon &= \frac{N_B}{N_S + N_B}. \end{aligned} \tag{10.2}$$

N_S is the number of photons in the ring and N_B is the number of photons in the background in the θ_{rec}^{photon} range from 0 to θ_{max} [80]. Both G and B are normalized to unity, ϵ is the background fraction, and Θ_M is the upper limit of the θ^{ring} range (70 mrad). The Likelihood is then normalized to the number of photons N. One uses $\mathrm{L} = \sqrt[N]{L_N}$, to be able to compare Likelihood values of different particles.

For each particle with a reconstructed ring, the Likelihood L is evaluated for three mass hypotheses, namely pions, kaons and protons. The mass hypothesis with the largest value of L is taken as the one to be used. In this approach for the

evaluation of L, all 'photons' with the reconstructed angle each emitted photon spans with the particle trajectory direction θ_{rec}^{photon} smaller than 70 mrad are taken into account. With C_4F_{10} as radiator material and $\beta = 1$ particles the Cherenkov angle θ_C is 55.8 mrad. Table 10.1 shows the results of particle mass correlations. Summing up the number of particles in each column gives the number of particles of the indicated type, generated in the Monte Carlo simulation and accepted for identification. Each entry in a column is the number of particles identified by the Likelihood according to the label of the row. One gets identification efficiencies (number of correctly identified particles over number of particles *accepted* for identification) of 96.5% for p, 98.6% for K and 99.8% for π.

ID efficiency		number of particles			contamination
$96,5$ %	ident. as p	11	2	551	$2,4$ %
$98,6$ %	ident. as K	30	1884	10	$2,1$ %
$99,8$ %	ident. as π	29409	25	10	$0,1$ %
		gen. π	gen. K	gen. p	
		$\sum 29450$	$\sum 1911$	$\sum 571$	

Table 10.1: Likelihood particle mass assignments for π, K, and p. The first and last column show the identification efficiencies and the sample contamination which is defined as the number of incorrect identifications over the number of particles identified for the given mass.

The Likelihood used here [81] is the 'RING Likelihood' in which only photons belonging to a reconstructed ring are taken into account, to be compared to the 'ALL Likelihood' where all the photons related to a particle trajectory are used. Taking the mass hypothesis for π, K or p Likelihood values are computed together with a background hypothesis for reference. For that purpose the particle momentum and the refractive index of the radiator gas are needed. The following analysis has been made using sample runs out of the production period P2E of the 2002 run, where the RICH special output files (they are called gfiles) have been processed with best known values for the refractive index. Three quantities are used:

- the particle momentum, which is known from the tracking. The momentum range from 8 - 38 GeV/c, split into five bands of 6 GeV/c each, is taken into account,
- the three Likelihood ratios L_π, L_K, L_p to the background Likelihood L_B. A particle is considered to be identified, when $R_{particle} = L_{particle} / L_B$ is maximum,
- the three ratios of the maximum Likelihood to the second largest Likelihood L_{Max2}, $r_{particle} = L_{particle} / L_{Max2}$.

There is a clear correlation between $R_{particle}$ and $r_{particle}$ just like one expects between $R_{particle}$ and $\Delta\Theta_{particle} = \Theta_{Ring} - \Theta_{Mass}$ for the mass of the corresponding particle. It becomes clear that cuts in those quantities are not independent. Figure 10.1 shows the mass distribution as calculated from the particle momentum and the reconstructed ring angle Θ_{RING}. The solid peak (in color) indicates particles identified as $K^{'S}$. No cuts have been applied.

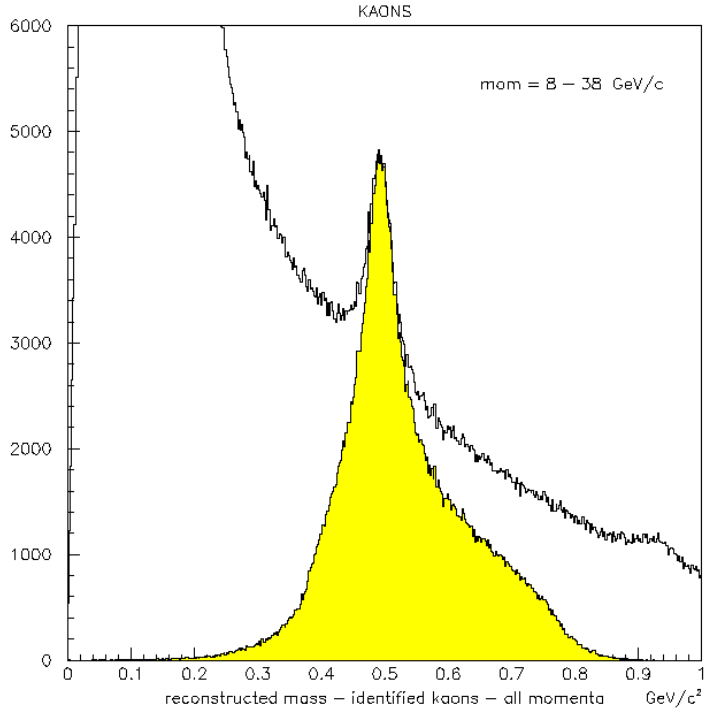

Figure 10.1: Reconstructed mass spectrum for all particles and for identified kaons (color) within the momentum range from 8 - 38 GeV/c.

The width of the peak is rather large because of a decreasing mass resolution with momentum and mostly because of the background under and to the right hand side of the peak. Plotting L_K/L_B versus reconstructed mass a value close to 1 stands for a Likelihood value being not significantly different from the one of the background, indicating a poorly identified particle. A cut is applied at L_K / L_B = 1.4 (Cut1). Figure 10.2 points out the effect of this cut. Similar to the first cut, plotting L_K/L_{Max2} versus reconstructed mass a cut L_K/L_{Max2} = 1.4 (Cut2) is applied as can be seen in Figure 10.3). Note that this cut includes Cut1. A next step in optimizing the distributions can be achieved introducing a cut in the number of photons per reconstructed ring ($N \geqslant 7$) and a cut in the ring reduced $\chi^2/\nu \leqslant 3$. As a result, the mass peak in Figure 10.4 shows a slightly reduced height that means that less well measured signal events are removed.

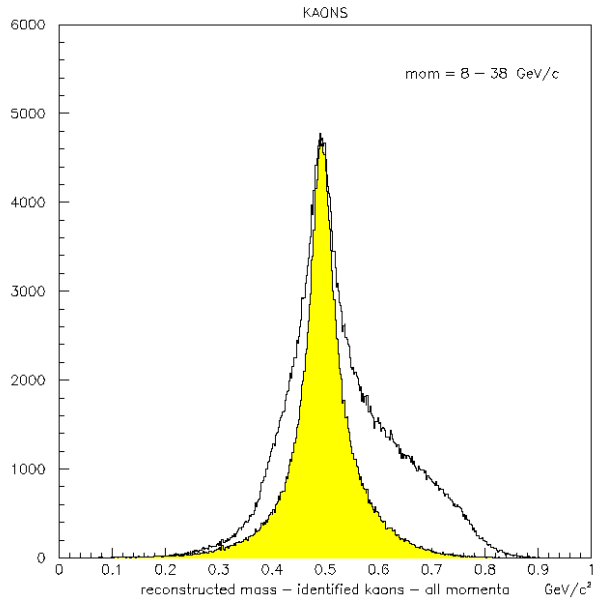

Figure 10.2: Reconstructed mass spectrum of identified kaons (color), after the cut L_K/L_B, as described in the text, superimposed on the uncut K mass distribution as shown in Figure 10.1.

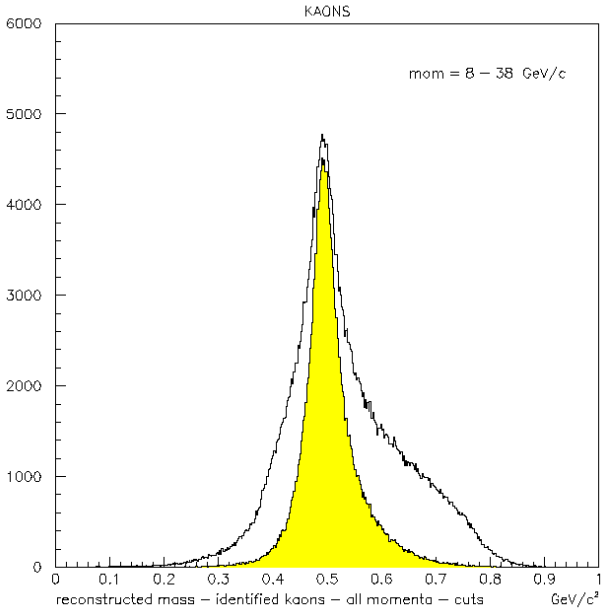

Figure 10.3: Reconstructed mass spectrum of identified kaons (color), after the cut L_K / L_{Max2} (Cut1 and Cut2), together with the uncut distribution of Figure 10.1.

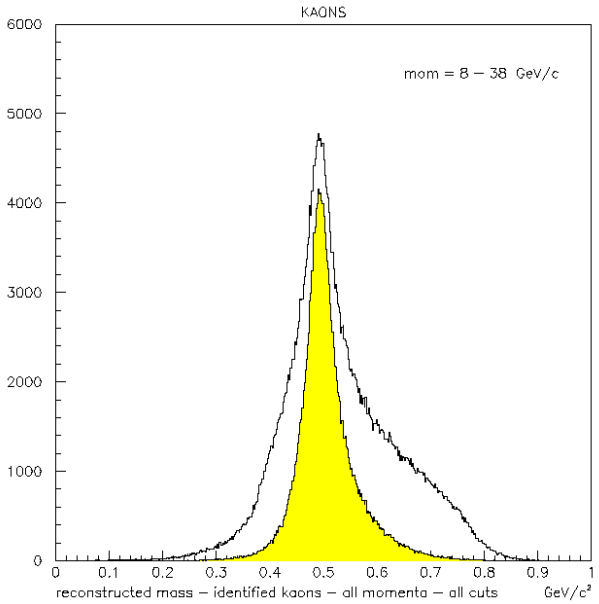

Figure 10.4: Reconstructed mass spectrum of identified kaons (color), after the cuts L_K/L_B, L_K/L_{Max2} and cuts in $N_{photons}$ and ring χ^2, together with the uncut distribution as shown in Figure 10.1.

10.2.1 Comparison with Monte Carlo Data

PYTHIA and JETSET are programs for the generation of high-energy physics events, i.e. for the description of collisions at high energies between elementary particles such as e^+, e^-, p and $\overline{p}$ in various combinations. Together they contain theory and models for a number of physics aspects, including hard and soft interactions, parton distributions, initial and final state parton showers, multiple interactions, fragmentation and decay. They are largely based on original measurements, but also use many theoretical predictions. Using these generators and 2002 apparatus geometry files the following plots were generated.

Comparing Figure 10.1 and 10.5, both showing the mass spectrum for all particles and for identified kaons (color) in the momentum range from 8 - 38 GeV/C, the factor of two in the K mass width (FWHM of $\approx$ 25 MeV/c to be compared to $\approx$ 50 MeV/c for real data) is in good accordance with the difference in Cherenkov angle resolution of 250 μrad for Monte Carlo data and 400 μrad for real data. The number of photons per ring being a factor of two lower with respect to the expected number is the clear reason for this. (Note that the resolution goes with $\sqrt{N}$). Applying all cuts (Cut1, Cut2 and the cuts in $N_{photons}$ and ring χ^2) to the Monte Carlo data one obtains Figure 10.6.

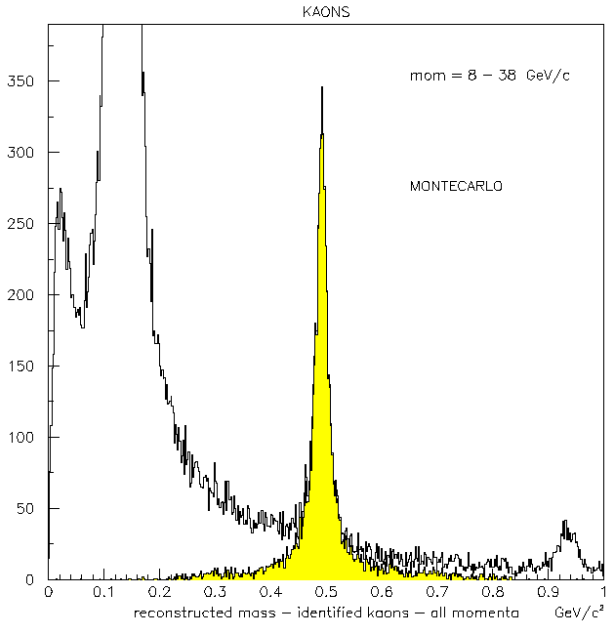

Figure 10.5: Mass spectrum for Monte Carlo generated particles and for identified kaons (color) in the momentum range from 8 - 38 GeV/c. This plot has to be compared to Figure 10.1.

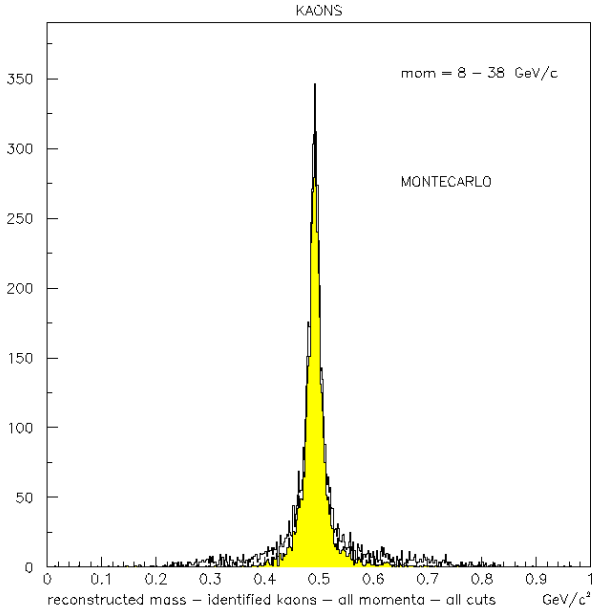

Figure 10.6: Mass spectrum for Monte Carlo generated particles and for identified kaons (color), where all cuts have been applied. This plot has to be compared to Figure 10.4.

As the Likelihood values for the masses of π, K, and p contain the derivatives of the Likelihood with respect to the refractive index (dL/dn), they have to be used to do corrections of these Likelihood values for differences of the value of the refractive index used in the production compared to the correct value. Figure 10.7 and 10.8 show the reconstructed mass distribution of identified kaons when incorrect values for the refractive index are used [Δ(n-1) $\simeq$ 13% and 6%, respectively]. In the second case the correction is much more effective. In this context incorrect means there is a non negligible discrepancy between the real value for the refractive index and the value used in the analysis for the corresponding period. Figures 10.7b) and 10.8b) demonstrate the effectiveness of the correction: with a decreasing error on the refractive index Δ (n-1) as input the match of the curves for the correct and the corrected refractive index is increasingly better. Looking at real data (Figure 8.19) one sees changes in the refractive index because of day/night fluctuations and the fact that during the operation of the radiator gas system some liquid was filled up.

In conclusion one can claim that the use of Cut1 is a useful approach to improve the K mass peak and to reduce the background at the same time, without cutting in the mass range. In comparison the effects of Cut2 are less obvious. As cuts in the number of photons per *ring* and *ring* χ^2 cut off part of the real signal, they have to be well tuned.

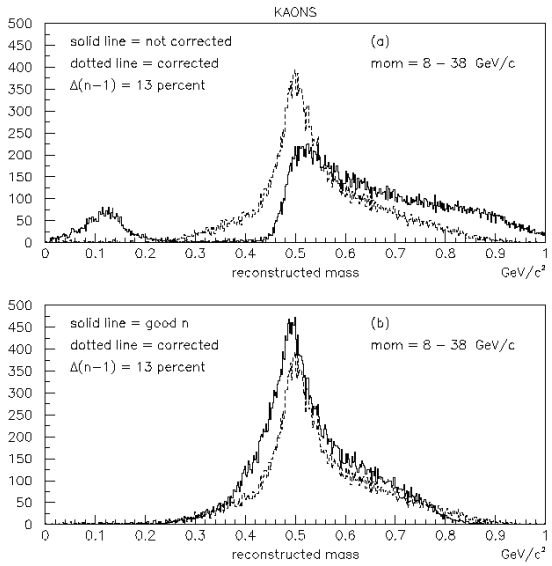

Figure 10.7: Figure (a) shows the reconstructed mass distribution of identified kaons as solid line, when an incorrect refractive index, Δ (n-1) $\simeq$ 13%, is used in processing. As dotted line the same distribution is plotted, after the use of the Likelihoods' derivatives with respect to the refractive index for correction. Figure (b) shows the mass distribution of identified kaons as solid line, using the correct value for the refractive index. The dotted line corresponds to the same correction as explained in (a).

Figure 10.9 compares 2002 data with Monte Carlo in the momentum range from 2 to 50 GeV/c. There is already a good agreement, nevertheless it has to be mentioned that the Monte Carlo simulation was substantially improved for 2003 data and detector geometry, which will further improve data quality together with a much higher statistics.

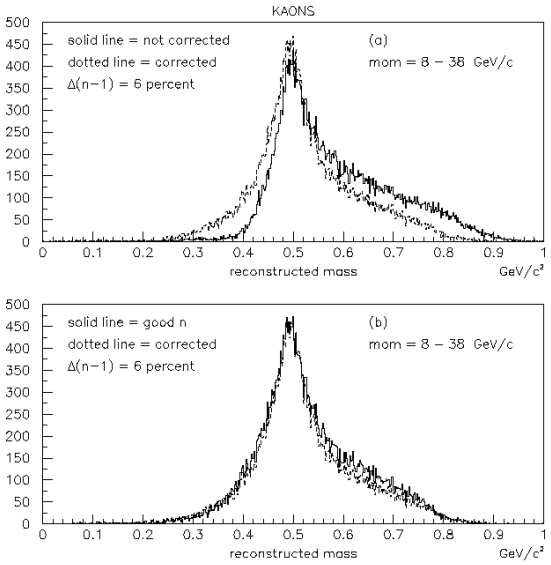

Figure 10.8: Figures (a) and (b) show the same as in Figure 10.7 but in the case of an incorrect refractive index, Δ(n-1) $\simeq$ 6%.

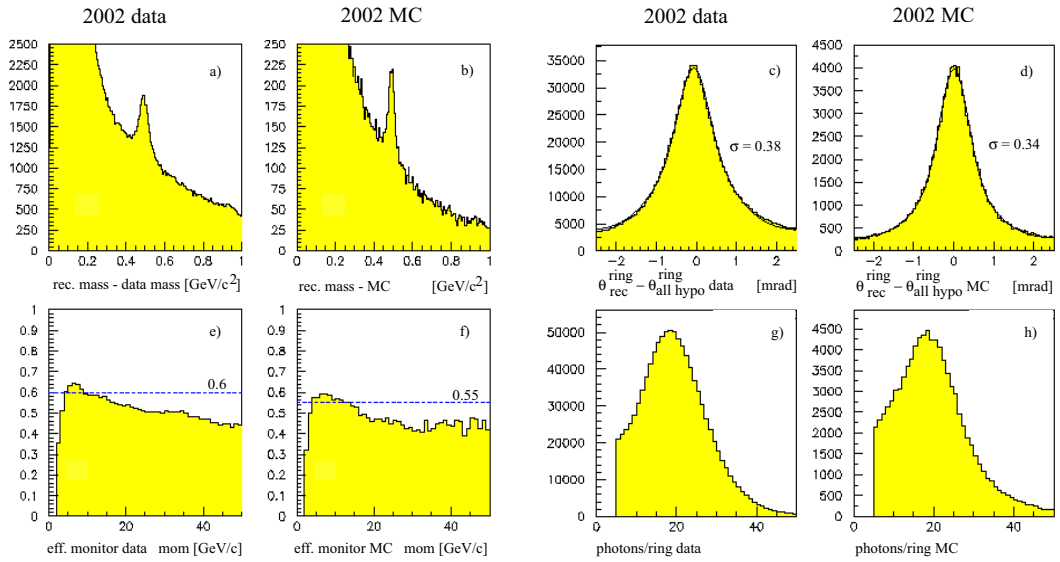

Figure 10.9: The plots show a comparison of 2002 data vs. Monte Carlo in the momentum range from 2 to 50 GeV/c. Figures (a) and (b) show a reconstructed mass spectrum. Figures (c) and (d) show the reconstructed emission angle subtracted from the emission angle taking all possible mass hypotheses into account: $\theta_{reconstr.}$ - $\theta_{allHypoth.}$. Figures (e) and (f) show the efficiency monitor and Figures (g) and (h) show the number of photons per ring.

10.3 Particle Identification on χ^2 Basis

For a given mass hypothesis and from the measured particle momentum the particle velocity β is determined. In case of β being above the Cherenkov threshold θ_{mass}^{ring} is calculated as

$$cos\ \theta_{mass}^{ring} = \frac{1}{\beta n}, \tag{10.3}$$

with n as the refractive index of the radiator gas. The χ^2 is then computed summing over N^{photon}, all the photons in the reconstructed ring

$$\chi^2 = \sum_{k=1}^{N^{photon}} \frac{\left(\theta_{rec,k}^{photon} - \theta_{mass}^{ring}\right)^2}{\left(\sigma_\theta^{photon}\right)^2}. \tag{10.4}$$

With the help of χ^2 one can choose among the different mass hypotheses. The σ_θ^{photon} is the standard deviation of the distribution of θ_{rec}^{photon}, the angle between each photon reconstructed in the ring and the particle trajectory.

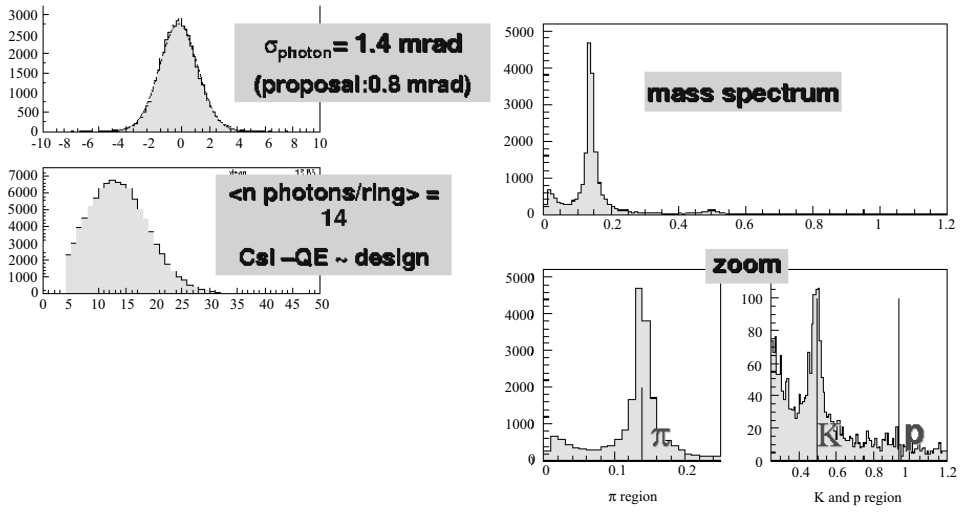

Figure 10.10: 2002-run, Low intensity - Calibration-Run. On the left side the photon Cherenkov angle accuracy σ_{photon} for photons belonging to reconstructed rings, the number of photons per reconstructed ring after clusterization. The right side shows a mass spectrum in the range from 0 to 1.2 GeV, computed from the measured Cherenkov angle and the particle momentum. The pion, kaon, and proton mass regions are magnified.

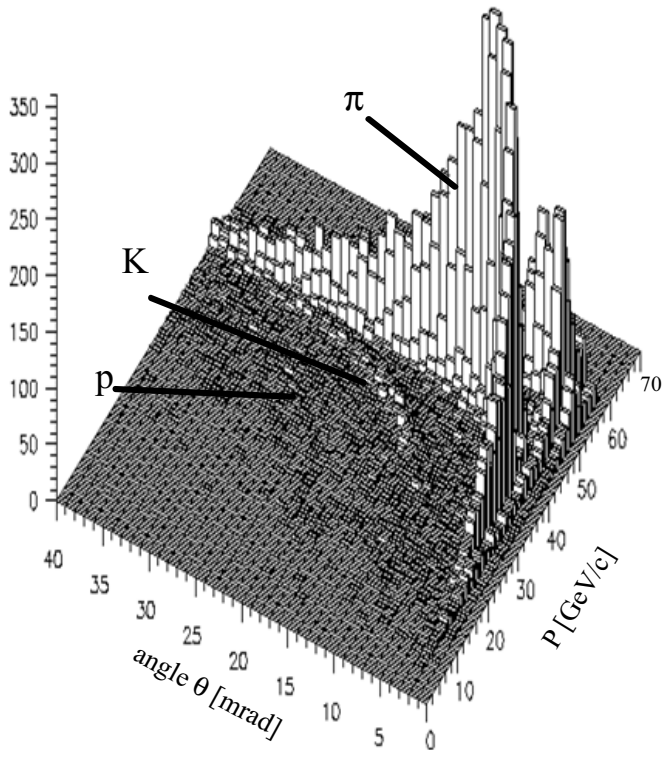

Figure 10.11: 2002-run, Low intensity. A three dimensional $\Theta_{cherenkov}$ vs. momentum plot is shown. The pion mass is 140 MeV, the kaon mass is 494 MeV and the proton mass is 940 MeV.

On the left side, Figure 10.10 shows the distribution of $\Theta_{Photon} - \Theta_{Ring}$ in mrad after a best-fit to a circle, with a standard deviation of $\sigma = 1.4$ mrad, to be compared to the expected value of 0.8 mrad. This difference can be explained by the fact that the RICH-1 geometry was not yet calibrated. The mean value of the number of photons per reconstructed ring can be seen to be 14 which is in reasonable agreement with the expected value taking into account that the vessel was only filled to $\sim 80\%$ with C_4F_{10} during that measurement. The right side shows the mass spectrum computed from the particle momentum and the measured cherenkov angle. Pion and kaon masses are clearly reconstructed while the proton peak is barley visible due to low statistics.

Figure 10.11 shows a three dimensional $\Theta_{cherenkov}$ vs. momentum plot in the momentum range from 0 to 70 GeV/c. There is a strong signature of pions visible while kaons are comparably weak and protons are practically invisible.

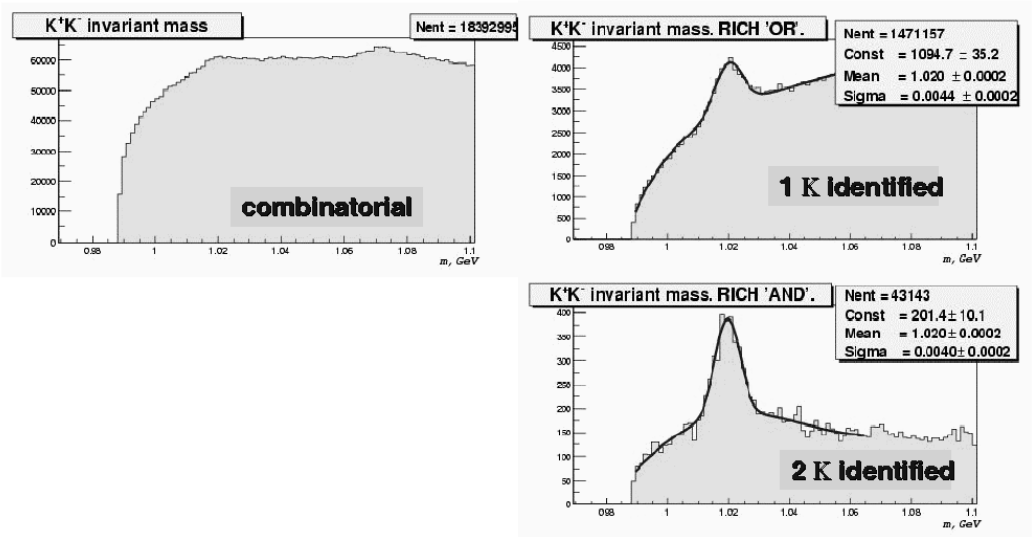

Figure 10.12: K^+K^--separation. The invariant mass is plotted, showing combinatorial events, events with *one* identified K and *two* identified K.

The left side of Figure 10.12 shows an invariant mass plot in the mass range from 0 to 1.1 GeV, where all combinatorial events are plotted (number of entries 18.4 millions). The upper right plot shows the K^+K^- invariant mass spectrum where one kaon is identified, the lower right side shows the mass spectrum for two identified kaons.

10.4 First Results on D^0 and D^* Analysis

The identification of D^0 and D^* is part of the COMPASS muon programme (See chapter 4). Figure 10.13 and 10.14 compare the D^0 mass spectrum with and without PID from RICH-1, respectively. In the first case the χ^2 method is used for the data analysis. In both cases the signal to background ratio is only fair: 0.07 (entries divided by number of Ds) in the first and 0.007 in the second case. Higher statistics, better understanding of the background, and improved overall efficiency for the RICH-detector will significantly enhance these numbers. Nevertheless an increase in the Figure of Merit by a factor of two is visible.

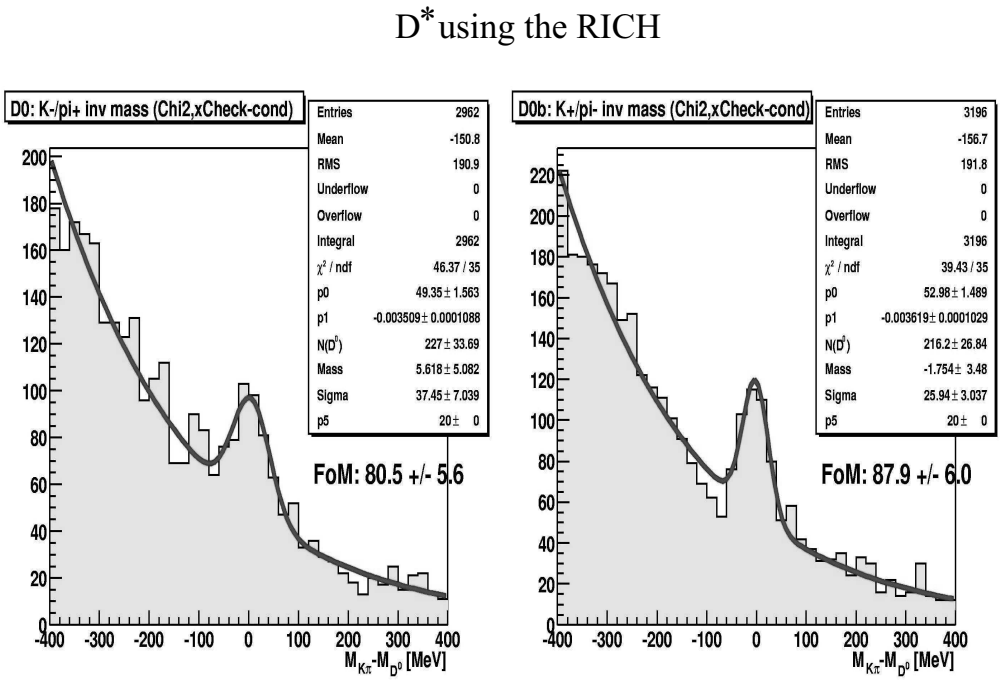

Figure 10.13: K^-/π^+ (left side) and K^+/π^- invariant mass spectrum using particle identification with RICH-1.

Table 10.2 compares the *Figure of Merit* ($\mathcal{F}o\mathcal{M}$) for D^* and D^0 particles, with and without PID from the RICH-1 detector. In case of the D^* one finds a factor of three for the $\mathcal{F}o\mathcal{M}$, while for D^0 the $\mathcal{F}o\mathcal{M}$ lies in between the two values for the D^*. The *Figure of Merit* is defined as

$$\mathcal{F}o\mathcal{M} = \frac{S}{1 + \frac{B}{S}}$$

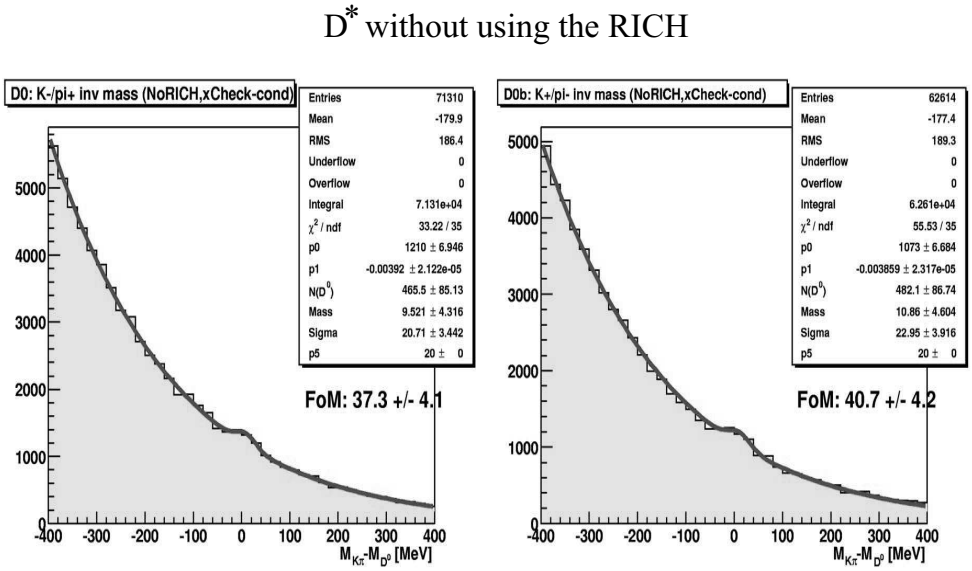

Figure 10.14: K^-/π^+ (left side) and K^+/π^- invariant mass spectrum *without* using particle identification with RICH-1.

	[S]	[S/B]	$[\mathcal{F}o\mathcal{M}]$	ϵ_S
D^* + RICH	159.9 ± 20.7	0.68 ± 0.09	64.7 ± 12.8	0.077
D^* no RICH	218.7 ± 49.4	0.11 ± 0.03	22.2 ± 8.9	0.108
D^0 + RICH	1127.8 ± 177.5	0.043 ± 0.007	46.0 ± 13.3	0.071

Table 10.2: Global efficiency for the D^0 and D^* signal.

10.5 RICH Efficiency and Purity

The following determination of the efficiency ϵ and purity P is based on a simple Cherenkov angle selection with no a priori knowledge of the refractive index as a function of time and a kinematical selection of kaons and pions.

$$P = \frac{number\ of\ genuine\ K}{total\ number\ of\ identified\ particles}. \tag{10.5}$$

For a perfect particle identification one would expect a background over signal ratio as determined from the heavy flavor event generator AROMA [82], of

$$\frac{B}{S_0} = \frac{Pythia\ generated\ K\pi}{Aroma} \approx 6. \tag{10.6}$$

Taking a realistic particle identification one gets

$$\frac{B}{S} = \frac{B}{S_0} \times \frac{K+\pi}{K} = \frac{B}{S_0} \times \frac{1}{P}, \tag{10.7}$$

arriving at the *Figure of Merit* :

$$\mathcal{F}o\mathcal{M} = \epsilon P \times \frac{B/S_0 + 1}{B/S_0 + P}. \tag{10.8}$$

For B $\gg$ S the *Figure of Merit* can be written as

$$\mathcal{F}o\mathcal{M} \approx \epsilon P \tag{10.9}$$

The RICH efficiency ϵ_{RICH} is defined as $\epsilon_{RICH} = \frac{S_{RICH}}{S}$

	$\mathcal{F}o\mathcal{M}$	ϵ_{RICH}	P
Perfect PID	1	1	1
no PID	0.10	1	0.10
RICH-1 PID	0.20	0.60	0.31

Table 10.3: *Figure of Merit* with and without PID

For the determination of the $\mathcal{F}o\mathcal{M}$ for $D^0 \rightarrow K\ \pi$ the following efficiencies are taken into account:

Ideal K ID : $\epsilon = 71\%$ (with realistic Monte Carlo)
Ideal RICH : $\epsilon = 62\%$ (K within the acceptance and purity range)
Real RICH : $\epsilon = 22\%$

For the following considerations N_1 and N_2 are taken as parameters defining the σ cuts for the Cherenkov angle θ. Table 10.4 points out the *Figures of Merit* for several assumptions for $\delta\theta$: $\delta\theta_K < N_1 \times \sigma$, $\delta\theta_\pi < N_2 \times \sigma$. The values for the $\mathcal{FOM}$ vary by 15%.

N_1	N_2	ϵ	P	$\mathcal{FOM}$
2	3	0.31	0.53	0.166
3	2	0.40	0.49	0.195
5	2	0.45	0.39	0.178

Table 10.4: Determination of the *Figure of Merit.*

As described above there are two different approaches, namely the Likelihood-method and the method of particle identification on χ^2 basis. Table 10.5 and 10.6 compare different values for the $\mathcal{FOM}$ using different boundary conditions (weight of the background Likelihood and the two particle mass hypothesis for π and p): taking a variation of about 10% for $\mathcal{FOM}$ into account, there is no clear advantage of one over the other method.

N_1	N_2	ϵ	P	$\mathcal{FOM}$
1	1	0.50	0.33	0.165
1.1	1.2	0.45	0.41	0.182
1.4	1.2	0.41	0.45	0.187

Table 10.5: *Figure of Merit* using Likelihood analysis. $\mathcal{L}_K > N_1 \times \mathcal{L}_{Background}, \mathcal{L}_K > N_2 \times \mathcal{L}_{\pi,p}$.

N_1	N_2	ϵ	P	$\mathcal{FOM}$
∞	1	0.51	0.26	0.135
4	1.2	0.36	0.50	0.184

Table 10.6: *Figure of Merit* using χ^2 analysis. $\chi^2/ndf < N_1, \chi^2/ndf < N_2 \times \chi^2/ndf_{\pi,p}$.

First analysis [83] gave some indication that, depending on the error of the refractive index used during data production (n_p = n + Δn), the Likelihood analysis is preferable in case of Δn < 6 % (n-1), while the χ^2 analysis is advantageous in case of Δn > 10 % (n-1). In both cases the dependence on the refractive index n are taken into account using $d\mathcal{L}/dn$ and $\chi^2(n)$. A more detailed introduction into the RICH 1- χ^2 analysis can be found in [84].

11 Summary and Outlook

One of the main physics questions tackled by the COMPASS collaboration is the measurement of the gluon spin contribution to the nucleon spin from open charm leptoproduction. Therefore the polarized gluon distribution ΔG is measured via deep inelastic scattering of polarized muons off polarized proton and deuterium targets. The apparatus consists of two successive spectrometers comprising several tracking stations, electromagnetic and hadronic calorimetry, muon identification and Ring Imaging Cherenkov Counters for particle identification.

The major requirements for the RICH detector of the first spectrometer, RICH-1, are the capability to separate pions, kaons and protons with momenta up to 55 GeV/c, the full acceptance of the large-angle spectrometer together with the demand to minimize the total amount of material used, as RICH-1 is followed by electromagnetic and hadronic calorimeters and the small-angle spectrometer. The detector is a gas detector with 83 m^3 of C_4F_{10} as radiator at atmospheric pressure. The Cherenkov photons are reflected by a mirror surface with more than 20 m^2 on a set of two photon detectors placed below and above the acceptance region. As UV photon absorbing impurities have to be strictly avoided, water vapor and oxygen traces are only tolerable below 5 ppm.

The author contributed to the build up and commissioning of the radiator gas system, the preparation and pre-cleaning of the gas and the quality control by means of transparency measurements. The RICH-1 gas system is a recirculation system with on line purification units, a gas liquid separation unit to allow the filling and the recovery of the radiator gas before and after a run and a pneumatically controlled regulation valve to sustain the operating pressure within small limits. As the initial quality of the radiator gas was not satisfactory a pre-cleaning procedure was developed, using a series of filters to reach the anticipated transparency. Molecular sieves, copper and activated carbon filters showed the best performance. In order to guarantee the most stable operating conditions regular transparency checks were carried out, using several measuring devices: a reflectometer was used in the initial cleaning phase, while a monochromator system and an integral transmission measurement system allowed for well controlled and stable conditions during the runs of the year 2002 and 2003.

A further improvement would be an automated transparency and refractive index measurement system that could directly provide gas quality data, to be used in the data analysis. This would substantially increase the data quality for the RICH analysis, as these parameters are directly involved in the ring reconstruction.

First results on the D^0 and D^* analysis are presented where two different analysis attempts are compared: the Likelihood analysis and the χ^2 analysis. 2002 data and Monte Carlo simulations are in good agreement. A complete analysis of 2003 data with a further improved simulation package and much higher statistics will enhance the physics outcome.

List of Tables

List of Figures

Bibliography

[1] J. Ashman et al. *An investigation of the spin structure of the proton in deep inelastic scattering of polarised muons on polarised protons,*. Nucl. Phys., **B 328**, 1 (1989).

[2] The NMC Collaboration. *Detailed Measurements of Structure Functions from Nucleons and Nuclei*. Proposal to the SPSC, CERN/SPSC 85-18 SPSC/P210, 27. Feb. 1985, pages 1–64.

[3] V.W. Hughes et al., The Spin Muon Collaboration. *Measurement of the Spin-dependent Structure Functions of the Neutron and Proton*. CERN/SPSC 88-47 (SPSC/P242) (1988).

[4] E. Nappi et al. *The Hadron Muon Collaboration Letter of Intent*. CERN/SPSLC 95-27, SPSLC/I204, March 1995 (1995).

[5] S. Paul et al. *CHEOPS, Letter of Intent*. CERN/SPSLC 95-22, SPSLC/I202 March (1995).

[6] B. Adeva et al. *Combined analysis of world data on nucleon spin structure functions*. Phys. Lett., **B 320**, 400 (1994).

[7] P.L. Anthony et al. *Determination of the neutron spin structure function*. Phys. Rev. Lett., **71**, 959 (1993).

[8] J. Ellis and R. Jaffe. *Sum rule for deep-inelastic electroproduction from polarized protons*. Phys. Rev., **D 9**, 1444 (1974).

[9] F. Close. *The Nucleon Spin Crisis Bible*. Rutherford Appleton Lab. UK, **hep-ph/9306288** (1993).

[10] S. Aoki. *Lattice Calculations and Hadron Physics*. International Journal of Modern Physics A, **Vol. 15, No. supp01B**, 657 (2000).

[11] C.R. Allton et al. *Lattice Calculation of $D-$ and $B-Meson$ Semileptonic Decays*. CERN-TH 7484/94.

[12] N. Isgur, R. Kokoski, and J. Paton. *Gluonic excitations of mesons: Why they are missing and where to find them.* Phys. Rev. Lett., **54**, 869 (1995).

[13] T. Barnes, F. E. Close, and E. S. Swanson. *Hybrid and conventional mesons in the flux tube model: Numerical studies and their phenomenological implications.* Phys. Rev., **D 52**, 5242 (1995).

[14] F. E. Close and P. R. Page. *The production and decay of hybrid mesons by flux-tube breaking.* Nucl. Phys., **B 443**, 233 (1995).

[15] F. Hussain and G. Thompson. *An Introduction to the Heavy Quark Effecitve Theory.* IC/95/15 hep-ph/9502241.

[16] B. Adeva et al., The Spin Muon Collaboration. *Measurement of the Polarization of a High Energy Muon Beam.* Nucl. Instr. Meth., **A 343**, 363 (1994).

[17] B. Adeva et al., The Spin Muon Collaboration. *Measurement of the Spin-dependent Structure Function $g_1(x)$ of the Deuterium.* Phys. Lett., **B 302**, 533 (1993).

[18] P.L. Anthony et al. *Deep inelastic scattering of polarized electrons by ^3He and the study of the neutron spin structure.* Phys. Rev. Lett., **D 54**, 6620 (1996).

[19] E. Leader. *Spin dependent structure functions and the parton model spin crisis.* in: 24th International Conference on High-energy Physics. 24th Rochester Conference , Munich, Germany, pages 1017–1023 (1988).

[20] G. Altarelli and G. Ross. *Low x behaviour of the Isovector Nucleon Polarized Structure Function and the Bjorken Sum Rule.* Phys. Lett., **B 212**, 391 (1988).

[21] R. D. Carlitz et al. *The role of the axial anomaly in measuring spin-dependent parton distributions.* Phys. Lett., **B 214**, 229 (1988).

[22] S.J. Brodsky and J. Ellis et al. *Chiral symmetry and the spin of the proton.* Phys. Lett., **B 206**, 309 (1988).

[23] J. Collins et al. *Fragmentation of transversely polarized quarks probed in transverse momentum distributions.* Nucl. Phys., **B 396**, 161 (1993).

[24] K. Ackerstaff et al. *The HERMES Spectrometer.* Nucl. Instr. Meth., **A 417**, 230 (1998).

[25] M. Amarian et al., The HERMES Collaboration. *The HERMES Charm Upgrade Program: A measurement of the Double Spin Asymmetry in Charm Leptoproduction.* DESY-PRC 97-03 (1997).

[26] A. Airapetian et al. *Measurement of single-spin azimuthal asymmetries in semi- inclusive electroproduction of pions and kaons on a longitudinally polarised deuterium target.* Phys. Lett., **B 562**, 182 (2003).

[27] H. E. Jackson. *HERMES and the spin of the proton.* Int. J. Mod. Phys., **A 17**, 3551 (2002).

[28] S.E. Vigdor et al., Joint RSC STAR PHENIX Collaboration. *Proposal on spin physics using the RHIC polarized collider.* approved October 1993 as Brookhaven experiment R5 (unpublished).

[29] V. Ghazikhanian et al. *Proposal to Measure The Gluon Spin Distribution Using Polarized Open Charm Photoproduction.* SLAC-Proposal E161, **Sep. 8** (2000).

[30] M. Glueck, E. Reya, and W. Vogelsang. *Determination of Spin Dependent Parton Distributions in Polarized Leptoproduction of Jets and Heavy Quarks.* Nucl. Phys., **B 351**, 579 (1991).

[31] A. Watson. *Spin-spin asymmetries in inclusive muon proton charm production.* Z. Phys., **C 12**, 123 (1982).

[32] W. Vogelsang. *Proceedings: Physics at HERA.* pages 29–30 (1991).

[33] Physical Review D, Particles and Fields. *Meson Particle Listings.* The American Physical Society, **66**, 607 (2002).

[34] Physical Review D, Particles and Fields. *Meson Particle Listings.* The American Physical Society, **66**, 593 (2002).

[35] R. Jaffe and X. Ji. *Chiral-odd parton distributions and polarized Drell-Yan process.* Phys. Rev. Lett., **67**, 552 (1991).

[36] R. Jaffe and X. Ji. *Chiral-odd parton distributions and Drell-Yan processes.* Nucl. Phys., **B 375**, 527 (1992).

[37] D. Babusci et al. *Chiral symmetry and pion polarizabilities.* Phys. Lett., **B 277**, 158 (1992).

[38] J. Kyynäräinen and The Spin Muon Collaboration. *The SMC polarized target.* Nucl. Instr. Meth., **A 356**, 47 (1995).

[39] D.Adams et al. *The polarized double cell target of the SMC.* Nucl. Instr. Meth., **A 437**, 23 (1999).

[40] K. Kondo et al. *Polarization measurement in COMPASS polarized target.* to be published in Nucl. Instr. Meth. (2003).

[41] O. Lounasmaa. *Experimental Principles and Methods below 1 K* (Academic Press, 1974).

[42] F. Pobell. *Matter and Methods at Low Temperatures* (Springer, 1996).

[43] J. Ball et al. *First results of the large COMPASS ^6LiD polarized target.* Nucl. Instr. Meth., **A 498**, 101 (2003).

[44] D. Thers et al. *Micromegas as large microstrip detector for the COMPASS experiment.* Nucl. Instr. Meth., **A 469**, 133 (2001).

[45] H. Angerer and R. de Masi et al. *Present Status of Silicon Detectors in COMPASS.* Nucl. Instr. Meth., **A 512**, 229 (2003).

[46] E. Iarocci et al. *Plastic streamer tubes and their applications in high energy physics.* Nucl. Instr. Meth., **A 217**, 30 (1983).

[47] J.P. Peigneux et al. *The WA102 Proposal: A search for centrally produced non-qqbar mesons in proton proton interactions at 450 GeV/c using the CERN Omega Spectrometer and GAMS-4000.* CERN/SPSLC 94-22 (P281).

[48] M. Leberig. Ph.D. thesis, University of Mainz, Germany (2002).

[49] M. S. Curie. *Radioactivité II.* Hermann, page 345 (1935).

[50] P. Cherenkov. *Visible Radiation Produced by Electrons Moving in a Medium with Velocities Exceeding that of Light.* Phys. Rev., **52**, 387 (1937).

[51] I.M. Frank and I.J. Tamm. Dokl. Academie des Sciences de l'URSS, **14**, 107 (1937).

[52] V.L. Ginzburg. Zh. Eksp. Teor. Fiz. SSSR, **10**, 589 (1940).

[53] J. Seguinot and T. Ypsilantis. *A historical survey of ring imaging Cherenkov counters.* Nucl. Instr. Meth., **A 343**, 1 (1994).

[54] E. Nappi. *RICH detectors.* CERN-EP/99-149.

[55] The Proceedings of the 1st RICH Workshop. Nucl. Instr. Meth., **A 343** (1994).

[56] The Proceedings of the 2st RICH Workshop. Nucl. Instr. Meth., **A 371** (1996).

[57] The Proceedings of the 3st RICH Workshop. Nucl. Instr. Meth., **A 433** (1999).

[58] O. Zimmer. *Introduction to Nuclear and Particle Physics. 4. Passage of radiations through matter.* Lectures at the TU munich (2003).

[59] T. Ypsilantis and J. Seguinot. *Theory of ring imaging Cherenkov counters.* Nucl. Instr. Meth., **A 343**, 30 (1994).

[60] *Particle Physics Booklet.* Particle Data Group, page 206 (2002).

[61] J. Seguinot and T. Ypsilantis. *Evolution of the RICH technique.* Nucl. Instr. Meth., **A 433**, 1 (1999).

[62] J. Seguinot and T. Ypsilantis. *Photo-ionization and Cherenkov ring imaging.* Nucl. Instr. Meth., **142**, 377 (1977).

[63] The RD26 Collaboration. *RD26 status reports: CERN DRDC 93-96.* CERN DRDC 94-49, CERN DRDC 96-20.

[64] E. Albrecht et al. *The mirror system of COMPASS RICH-1.* Nucl. Instr. Meth., **A 502**, 236 (2003).

[65] P. Baillon et al. *Production of 300 paraboloidal mirrors with high reflectivity for use in the Barrel RICH counter in DELPHI at LEP.* Nucl. Instr. Meth., **A 277**, 338 (1988).

[66] W. Beusch et al. Internal Note 4, CERN/ECP/MIP (1993).

[67] G. Baum et al. *BORA, a front end board with local intelligence for the COMPASS collaboration.* Nucl. Instr. Meth., **A 433**, 466 (1999).

[68] XILINX. *Virtex VCX100 FPGA.* Programmable Logic Control.

[69] *Analog Devices, DSP Microcomputer, ADSP-21065L.*

[70] D. Broemmelsiek. *HERA-B RICH: Radiator Gas System Report.* private communication (1997).

[71] S. Amato et al., The LHCb collaboration. *LHCb - RICH Technical Design Report.* CERN LHCC 2000-037, LHCb TDR 3, page 18 (6 Sep. 2000).

[72] *BASF-Catalyst R3-11G, Technical Leaflet, 12.98.*

[73] E. Albrecht et al. *VUV absorbing vapours in n-perfluorocarbons.* Nucl. Instr. Meth., **A 510**, 262 (2003).

[74] D.E. Gray. *American Institute of Physics Handbook* (Mc Graw-Hill, 3rd ed., New York, USA).

[75] Polaroid (Polaroid Sonar ranging Module, 6500 series, PID 615077; Electrostatic transducer, 7000 series, PID 612366).

[76] CERN, EP/ESS GIF. *Gamma Irradiation Facility.* http://ess.web.cern.ch/ESS/GIFProject/index.html.

[77] Graham Woan. *The Cambridge Handbook of Physics Formulas* (Cambridge University Press, 2000).

[78] G. Baum et al. *RICHONE. A software package for the analysis of COMPASS RICH-1 data.* Nucl. Instr. Meth., **A 502**, 315 (2003).

[79] P. Schiavon. *Particle Identification in COMPASS RICH-1, Progress Report, May 2000.* COMPASS Web Page (2000).

[80] P. Schiavon. *Particle Identification in COMPASS RICH-1, Progress Report, September 2001.* COMPASS Web Page (2001).

[81] P. Schiavon. *Hints for PID in RICH-1, Progress Report, May 2003.* COMPASS Web Page (2003).

[82] G. Ingelman et al. *AROMA.* Comput. Phys. Commun., **101**, 135 (1997).

[83] Y. Bedfer. *RICH reconstruction.* Talk presented during the Compass Collaboration Meeting (2003).

[84] P. Schiavon. *Trieste reconstruction software for COMPASS RICH 1, Progress Report, December 1999.* COMPASS Web Page (1999).

Acknowledgment

In particular, I would like to thank Prof. Günter Baum for his continual support, for giving me the opportunity to work at CERN and to participate in the COMPASS-collaboration.

In addition I would like to thank many colleagues and collaborators that endorsed my work - Silvia dalla Torre, Fulvio Tessarotto and Andrea Bresan from the RICH team and Kenneth Gustafsson, Eric Weise, Stephane Platchkov, Jörg Pretz and Nicolas Dedek. The colleagues from the polarized target group, Fabrice Gautheron, Norihiro Doshita, Kaori Kondo, Juri Kisselv and Jaakko Koivuniemi. Furthermore many other colleagues as Olav Ullaland, Andre Braem and Michel Bosteels at CERN. My colleagues at the University of Bielefeld, Natasa Pavlovic, Bernhard Roth and Stefan Förster. Continuous supporters like Thomas Maxisch for permanent online help for all kind of computer or software questions.

Finally, I would like to thank my parents for their constant encouragement.

Index